

## ABSTRACT

CHILAMKURTI, YESASWI NARENDRA. Towards understanding the Heat Transfer Behavior of Dense Granular Media. (Under the direction of Dr. Richard Gould).

Over the past few decades, granular media is gaining attention as a viable option for heat transfer fluids (HTFs). From applications in chemical/material processing industries to state-of-the-art Concentrated Solar Power technologies, many research efforts are studying the use of ceramic particles to maximize the heat transfer efficiency of their systems. In addition, these particle-based HTFs can also serve as thermal storage media and pose limited safety concerns. Hence it is important to understand the particle-scale physics of granular media. With this motivation, the current work focusses on analyzing the different flow and heat transfer mechanisms in densely packed granular media.

In the early stages of the work, experimental techniques were employed to understand gravity-driven flow behavior of granular media in vertical circular tubes. Using these results as bench-mark data, computational studies were then implemented to gain deeper insights into the flow. The motion of particles was resolved with a Lagrangian approach using the high-fidelity Discrete Element Method (DEM). These preliminary studies helped in gaining an understanding of the velocity, packing fraction and pressure profiles in gravity-driven dense flows. Literature suggests that the heat transfer behavior of granular media is primarily restricted by the discrete nature of these flows. While previous works acknowledged a relatively high thermal resistance near the wall compared to the bulk of the flow, there was not an in-depth analysis of this phenomenon. Thus, DEM computational studies were conducted to incorporate the micro-structure of particles in modelling the wall-adjacent thermal resistance for vertical dense granular flows.

To study the heat transfer behavior of granular media, unlike the flow simulations, a two-way coupled computational strategy is mandatory. Hence, the DEM approach is coupled with a Finite-Volume (FV) approach to solve for the heat transfer of both particles and the interstitial air, respectively. The Open-Source library *CFDEM Coupling*<sup>®</sup> was used in the current study to join the Finite Volume PISO solver of *OpenFOAM*<sup>®</sup> and the DEM solver of *LIGGGHTS*<sup>®</sup>. Theoretical analyses in the literature suggest the existence of several modes of heat transfer in flowing granular media. Since it is beyond the scope of the current work to analyze all of them, the CFD-DEM heat transfer studies conducted here are restricted to static bed configurations. It was observed that the available heat transfer closure models severely underestimate the thermal behavior. Hence other multi-scale modelling approaches were explored to address these issues.

Particle-Resolved Direct Numerical Simulations (PR-DNS) were conducted to obtain high fidelity observations of different particle-scale heat transfer mechanisms. In addition to the conduction and convection heat transfer, an entirely different mechanism of heat transfer was observed in these simulations. This phenomenon – streaming heat transfer – was found to play a significant role in the overall thermal behavior of packed beds. Characteristics of this mechanism were carefully observed, and a theoretical model was developed to capture its behavior. The PR-DNS results were used to fine-tune the developed model to make it applicable over a wide range of thermal properties, particle sizes and bed packing fractions. Finally, this model was implemented in the CFD-DEM framework as another closure model. Studies were then conducted to analyze the relative contribution of each heat transfer mode for different thermal properties and void fractions. Further observations were also made to analyze the variation of the effective thermal conductivity of static beds with different thermal and geometrical properties. Thus, the proposed CFD-DEM framework was found to serve as a first step in estimating the particle-scale

heat transfer mechanisms with less computational expenditure, which can be implemented for most future granular systems.

© Copyright 2019 by Yesaswi Narendra Chilamkurti

All Rights Reserved

Towards understanding the Heat Transfer Behavior of Dense Granular Media

by  
Yesaswi Narendra Chilamkurti

A thesis submitted to the Graduate Faculty of  
North Carolina State University  
in partial fulfillment of the  
requirements for the degree of  
Doctor of Philosophy

Mechanical Engineering

Raleigh, North Carolina  
2019

APPROVED BY:

---

Richard Gould  
Committee Chair

---

Alexei Saveliev

---

Jack Edwards

---

Tarek Echehki

## **DEDICATION**

*To my parents,  
for their love and affection;*

*To my grandparents,  
for their memories and inspiration;*

*To my best friend Sneha,  
for her support through sheer joy and optimism;*

*And to the sweetest pup named Leia,  
for being the happiness I found during the darkest of times.*

## **BIOGRAPHY**

Yesaswi Narendra Chilamkurti was born on the 18th of May 1992 in Gudlavelleru, in the state of Andhra Pradesh, India. He received his bachelor's degree in Mechanical Engineering from Indian Institute of Technology Patna (IIT Patna) in May 2013. The author went on to study Mechanical Engineering in North Carolina State University (NCSU), Raleigh, North Carolina in fall 2013. Here, he began working in the Heat Transfer Laboratory from January 2014 under his academic and research advisor Dr. Richard Gould.

## ACKNOWLEDGMENTS

I would first like to thank my advisor, Dr. Richard Gould, for his great support and help with my research work. His perspective towards solving several research roadblocks I faced in that past 5 years is inspirational and something I would always look up to. I would also like to thank my committee members Dr. Alexei V. Saveliev, Dr. Jack Edwards, and Dr. Tarek Echeikki for their valuable time and input into my research.

It would be an understatement to say that my lab mate, Megan Watkins, just helped me with my research. She created an environment, where I could freely discuss the most elementary scientific issues, for hours, without worrying about being called stupid. Her strong will and patience have always inspired me to face any research issue without fearing failure. I cannot thank her enough for making me realize the importance of organizing and documentation in research, which is something I would carry throughout my entire professional career. I would also like to thank my other lab mate Alex Szersen for his valuable input and feedback to my research. I should also thank him for creating a loud-music-friendly environment and made working late-hours in lab cool again!

I would also like to express my gratitude to ARPA-E (Advanced Research Projects Agency-Energy) for the financial support they provided throughout my tenure. Furthermore, I would also like to thank the folks at RTI International for their valuable suggestions and inputs that guided my research direction.

Last but certainly not the least, I'd like to thank all my close friends Bharadwaj, Vishnu, Praveen, Sandeep, Swetha-Aditya, Sairaj, Sahith, Satish, Sushmitha, Swetha-Vikas, Nadish, Aravind, Pranav, Hari and Karthik, for making me realize I'm not alone in this journey.

## TABLE OF CONTENTS

<b>LIST OF TABLES .....</b>	<b>vii</b>
<b>LIST OF FIGURES .....</b>	<b>viii</b>
<b>Chapter 1 Introduction.....</b>	<b>1</b>
<b>Chapter 2 DEM Study of Dense Granular Media .....</b>	<b>11</b>
2.1 Governing Equations .....	13
2.2 Simulation Setup .....	19
2.3 Particle-Wall Contact Behavior .....	22
2.4 Residence Times and Fluctuations .....	25
2.5 Wall-adjacent Particle Mechanics .....	29
<b>Chapter 3 CFD-DEM Coupling.....</b>	<b>39</b>
3.1 Governing Equations .....	42
3.2 Heat Transfer Models .....	43
3.3 Coupling Paradigm.....	46
3.3.1 Void Fraction Model .....	48
3.3.2 Smoothing Exchange Scalars .....	49
3.4 Preliminary Heat Transfer Studies .....	50
<b>Chapter 4 Particle-Resolved DNS .....</b>	<b>57</b>
4.1 Simulation Methodology.....	58
4.2 Heat Transfer Studies of a Randomly Arranged Particle Bed .....	63
4.3 Heat Transfer Studies on a Single Stack of Particles .....	67
4.3.1 Verification of Lumped Capacitance Assumption and Conduction Model .....	68
4.3.2 Verification of Convection Model.....	72
4.3.3 Characteristics of Streaming Heat Transfer .....	74
<b>Chapter 5 Streaming Heat Transfer Model .....</b>	<b>77</b>
5.1 Model Development .....	77
5.2 Core Radius Empiricalization .....	85
5.3 Model Validation.....	87
5.3.1 Comparison with PR-DNS Predictions .....	87
5.3.2 Comparison with Models Available in Literature .....	89
5.3.3 Model Behaviour for Different Particle Bed Void Fractions .....	91
5.4 Heat Transfer Insights from CFD-DEM .....	94
5.4.1 Preliminary Observations .....	94

5.4.2 Relative Contribution of Different Heat Transfer Phenomena in a Packed Bed.....	96
5.4.3 Influence of Particle Bed Void Fraction on the Heat Transfer Physics .....	100
<b>Chapter 6 Conclusions.....</b>	<b>103</b>
<b>REFERENCES.....</b>	<b>106</b>

## LIST OF TABLES

<b>Table 1:</b>	Particle Properties for the Simulation Studies .....	21
-----------------	--	----

## LIST OF FIGURES

<b>Figure 1:</b>	Flow regimes present in granular flows.....	3
<b>Figure 2:</b>	(a) Experimental schematic used to conduct preliminary flow tests; (b) Mean velocity profiles of particles for different flow rates (x-axis is radial location inside the tube scaler with particle diameter); (c) Mean packing fraction profiles for different flow rates (x-axis is radial location inside the tube scaler with particle diameter) .....	5
<b>Figure 3:</b>	Multi-scale approach for dense fluid–particle flows comprising (1) discrete bubble model; (2) the two-fluid model based on the kinetic theory of granular flow; (3) the discrete particle model; (4) the immersed boundary model; (5) lattice Boltzmann model. (The last two models come under the DNS method) [31].....	7
<b>Figure 4:</b>	Particle contact force formulation on the contact plane.....	14
<b>Figure 5:</b>	Simulation geometry without and with particles (left to right).....	20
<b>Figure 6:</b>	Particle-wall contact behavior with different particle diameters in 0.007747m inner diameter tube .....	23
<b>Figure 7:</b>	Particle-wall contact behavior with different flow rates in 0.007747m inner diameter tube.....	24
<b>Figure 8:</b>	Variation of average particle-wall contact residence time with flowrate .....	26
<b>Figure 9:</b>	Radial profiles of Standard Deviation values of the particulate axial velocities for different flow rates. ....	28
<b>Figure 10:</b>	Variation of Normalized Near Wall Turbulence Intensity with different flowrates.....	29
<b>Figure 11:</b>	Particle arrangements in the wall-adjacent layer for mean axial flow velocities of (a) 0.023m/s and (b) 0.25m/s (using 7.75mm tube and 300 $\mu$ m particles).....	31
<b>Figure 12:</b>	Depiction of thermal resistances used to model wall-adjacent layer heat transfer [46]. Red denotes resistance considered for contact particles, blue denotes resistance for particles not in contact, and yellow denotes resistance for void spaces. ....	32
<b>Figure 13:</b>	Variation in the normalized number of particle contacts per unit wall area with average flow velocity and particle diameter in the 7.75mm tube.....	34
<b>Figure 14:</b>	Fraction of particles in wall-adjacent layer that are not in contact with the wall as a function of mean flow velocity and particle diameter. Results for 7.75mm tube.....	35

<b>Figure 15:</b>	Variation of the wall-adjacent layer packing fraction.....	36
<b>Figure 16:</b>	Variation of the saturation pressure with average flow velocity for different particle diameters in the 7.75mm diameter tube.....	38
<b>Figure 17:</b>	Variation in the average distance of NC particles with average flow velocity and particle diameter in the 7.75mm tube.....	38
<b>Figure 18:</b>	Example of a typical LIGGGHTS simulation input script .....	41
<b>Figure 19:</b>	Steps involved in CFD-DEM coupling.....	47
<b>Figure 20:</b>	CFD-DEM simulation setup with 1000K temperature on the bottom wall and 300 K on the top wall.....	51
<b>Figure 21:</b>	Temperature profiles of CFD-DEM solution after achieving steady state .....	52
<b>Figure 22:</b>	Temperature profiles of 1D Transient conduction equation in MATLAB after achieving steady state .....	53
<b>Figure 23:</b>	Variation of Effective Thermal Conductivity as seen in experiments [46] .....	54
<b>Figure 24:</b>	Variation of Effective Thermal Conductivity ( $k_{Eff}$ ) with Pressure as observed from CFD-DEM framework with ACF tuning .....	55
<b>Figure 25:</b>	Simulation Domain (Gravity in negative Z-direction).....	59
<b>Figure 26:</b>	Generation of a Three-Dimensional particle cloud using a Visual Basic Macro in Solidworks. (a) 3D sketch with points at the particle centroid locations; (b) Sketch-driven pattern of solid particles at the particle centroid locations .....	60
<b>Figure 27:</b>	Three-dimensional mesh used for DNS (Blue mesh cells represent particles while grey mesh cells represent the interstitial air) .....	61
<b>Figure 28:</b>	PR-DNS Implementation .....	63
<b>Figure 29:</b>	PR-DNS solution of a packed bed. Temperature distribution inside (a) Interstitial Fluid (Air) and (b) Particle.....	64
<b>Figure 30:</b>	Axial temperature profile inside the packed bed and the air column .....	65
<b>Figure 31:</b>	Heat flux distribution on the surface of a particle (Only one hemisphere depicted in the image).....	66
<b>Figure 32:</b>	PR-DNS Simulation configuration to evaluate the assumptions made in CFD-DEM (Gravity in negative z-direction).....	67
<b>Figure 33:</b>	Comparison of CFD-DEM and PR-DNS solutions for single stacked particle. a) Temperature Profile; b) Temperature Jump at contact interface .....	69

<b>Figure 34:</b>	Behavior of CFD-DEM and PR-DNS solutions for single-stacked particles with increasing particle thermal conductivity .....	70
<b>Figure 35:</b>	Intra-particulate temperature profile for single-stacked particles .....	71
<b>Figure 36:</b>	Comparison of temperature profiles with vacuum and interstitial air .....	73
<b>Figure 37:</b>	Variation of the CFD-DEM behavior for different Nusselt numbers .....	74
<b>Figure 38:</b>	Heat flux vectors highlighting the presence of streaming heat transfer.....	75
<b>Figure 39:</b>	Distribution of heat on a particle surface .....	76
<b>Figure 40:</b>	Streaming heat transfer model; (a) Particles not in contact (b) Particles in contact .....	78
<b>Figure 41:</b>	Example of Voronoi Tessellation (a) Tessellation of a packed bed [53]; (b) Voronoi Cells encapsulating two neighboring particles [54] .....	82
<b>Figure 42:</b>	Variation of neighbor radius with local void fraction. On y-axis, the neighbor radius is scaled with particle diameter. ....	84
<b>Figure 43:</b>	Variation of $R_{vc}$ with local packing fraction. On y-axis, the values are scaled with particle radius.....	85
<b>Figure 44:</b>	Variation of core radius with different simulation parameters .....	86
<b>Figure 45:</b>	Comparison of CFD-DEM with streaming heat and PR-DNS results for $k_{Part} = 2.534 \text{ W/m-K}$ and $k_{Air} = 0.02534 \text{ W/m-K}$ . (a) Axial Temperature Profile (b) Thermal gradient in z-direction .....	88
<b>Figure 46:</b>	Comparison of Effective thermal conductivity estimates from CFD-DEM results with PR-DNS.....	89
<b>Figure 47:</b>	Comparison of Streaming Heat Transfer Model in Equations 61 with models proposed by Cheng et al.....	90
<b>Figure 48:</b>	Generation of a dilute packing configuration. Image progression from left to right indicating particle insertion, particle settling and particle size reduction in sequence .....	92
<b>Figure 49:</b>	Comparison of CFD-DEM and PR-DNS results for a void fraction of 75%. (a) Axial Temperature Profile (b) Thermal gradient in z-direction.....	93
<b>Figure 50:</b>	Variation of effective thermal conductivity of a packed with void fraction as observed in CFD-DEM and PR-DNS implementations .....	94
<b>Figure 51:</b>	Variation of $k_{Eff}$ with number of particles inside the packed bed .....	95

<b>Figure 52:</b>	Variation of $k_{EFF}$ with number of particles inside the packed bed .....	96
<b>Figure 53:</b>	Net heat for every particle in the simulation domain.....	97
<b>Figure 54:</b>	(a) Total Convection heat transfer on a particle (b) Total Conduction and streaming heat on a particle .....	98
<b>Figure 55:</b>	Probability distribution of each heat transfer mechanisms for (a) $k_{Particle}/k_{Air} = 2.5$ , (b) $k_{Particle}/k_{Air} = 25$ , and (c) $k_{Particle}/k_{Air} = 250$ .....	99
<b>Figure 56:</b>	Percentage shares of different heat transfer behaviors to the overall heat for void fraction of 42% .....	100
<b>Figure 57:</b>	Probability distribution of Non-Contact streaming for different void fractions .....	101
<b>Figure 58:</b>	Variation of $k_{Eff}$ with $k_{Particle}/k_{Air}$ for different void fractions.....	102

# Chapter 1

## Introduction

Granular flows can become a viable alternative as high temperature heat transfer fluids in applications that rely on direct/indirect absorption of heat energy [1]–[3]. From applications in chemical/material processing industries to energy sectors, increasing the working temperature range remains as a primary path for achieving better thermodynamic cycles and operational efficiencies. In this context, use of flowing ceramic particles as opposed to conventional heat transfer fluids like steam, molten nitrate salts and/or liquid metals is gaining attention in the engineering and research community. Applications like concentrated solar power (CSP) are aggressively exploring the use of dry particles for heat transfer and thermal storage [4] to make their technologies viable and efficient. Thus, a careful study of the flow physics and heat transfer behavior of granular media is required before implementing them on an industrial scale.

Direct absorption systems, though easy to operate have large convective losses and flow instabilities[5]. Thus, industrial applications are primarily oriented towards indirect heat absorption systems with particles flowing through closed sections[6]. This is the motivation for limiting the current research to gravity-driven granular media, flowing in cylindrical tubes. From the study of static granular beds to the modelling of particulate collisions, our understanding of granular physics has increased steadily [7]–[15]. With the help of high-speed imagery and other

non-intrusive techniques like PIV, X-ray, MRI, and ECT, several intrinsic features were observed by the research community. In addition, computational methodologies like Molecular Dynamics and Discrete Element Analyses enabled the investigation of these flows in an explicit manner. However, the flow characteristics vary from configuration to configuration. In fact, every geometrical configuration may have different flow regimes, each of which have different governing physics. As a result, the most common approach in understanding the flow rheology of granular media is by studying individual configurations and extracting their intrinsic features.

Based on the particulate velocities, granular flows are broadly divided into three types – quasi-static flows, dense intermediate flows and dilute inertial flows. In the quasi-static regime, the inertia of individual particles becomes negligible and the granular media behaves like a solid. This tightly packed regime, which is governed by particle properties like friction, elasticity, shape etc., can be modelled using plasticity models of soil mechanics [10]. The dilute inertial regime, on the other hand, is mainly governed by the collisions of the particles. This gas-like regime can be modelled using analogies of the kinetic theory of gases [16] as the particles are strongly agitated and the momentum transfer is mainly through collisions. Between these two, lies the dense intermediate flow regime which has a fluid-like rheology with non-negligible particulate inertia. Despite the relatively high velocities, the particles maintain a continuous contact network [13], [17] propagating the stresses layer by layer. All these regimes have different flow physics and as a result, no universal framework has been developed to describe the whole range from solid-like quasi-static to gas-like collisional regimes. In general, with increasing flow rate, the granular flow transitions from quasi-static to the dilute regime. This classification is depicted in Figure 1.

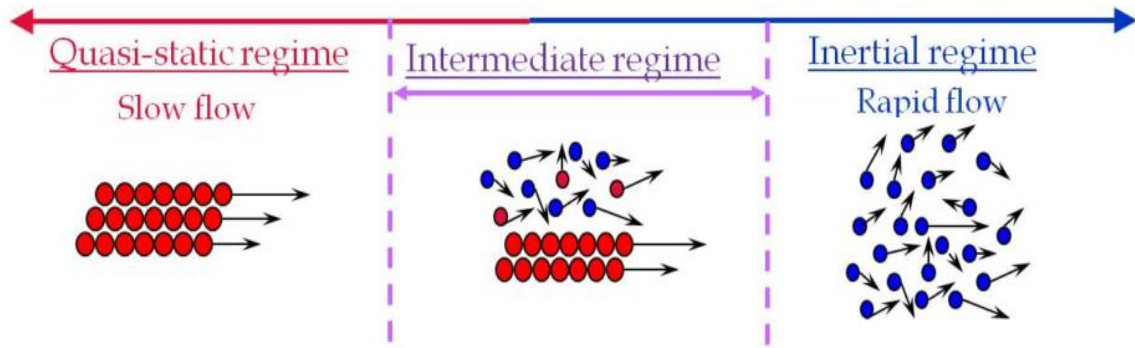
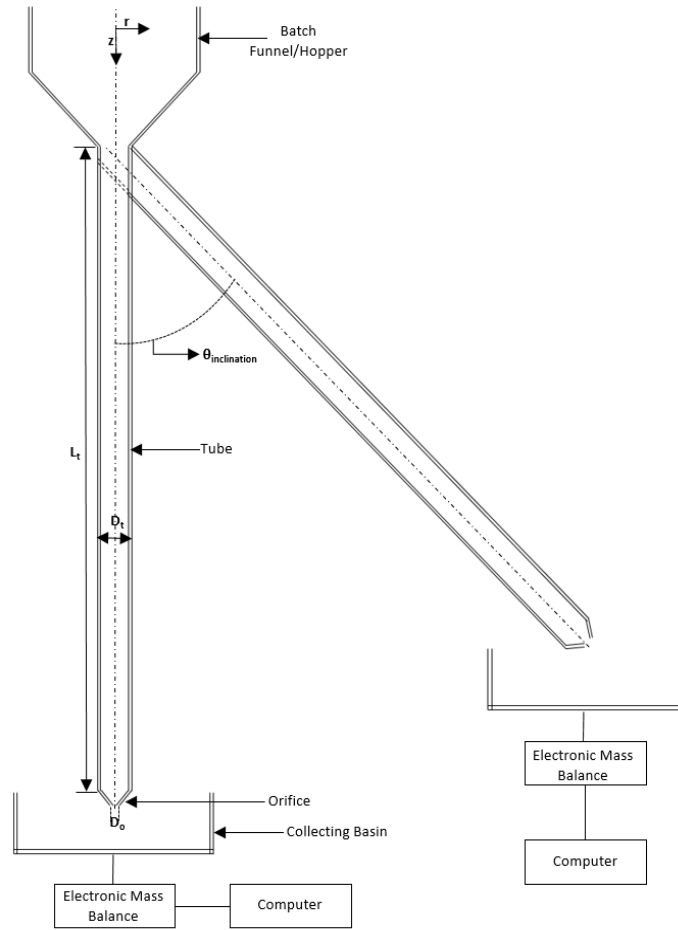


**Figure 1:** Flow regimes present in granular flows

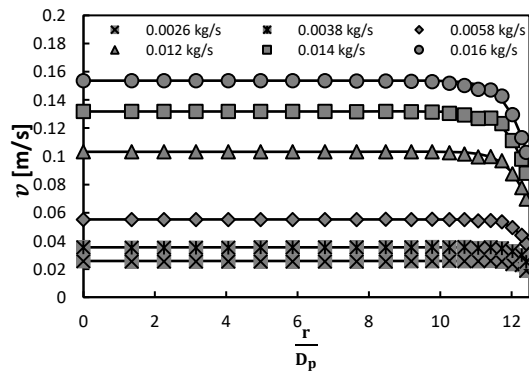
Several research works show that the heat transfer coefficients of granular heat transfer fluids (HTFs) increase with increasing flow rates [18], [19]. Thus, a natural tendency is to select the dilute collisional flow as the operational regime. But on the other hand, a similar observation was made with increasing packing fractions, within certain limits of temperatures. Thus, an ideal operation regime could be obtained from the intermediate dense flows where a continuous particulate contact network is maintained. In this regime, there exists a fluid-like rheology with stresses propagated layer by layer and a dense particulate packing. Hence, the dense flow regime with high packing fractions is the primary focus of the current research. Since these flows cannot be pneumatically conveyed, gravity driven flows are considered. Gravity driven flows have been studied over the years both experimentally and computationally [15], [20]. But a majority of these studies focused on quasi-static or dilute inertial regimes. Though several researchers worked in the intermediate dense regime, the complexity associated with this regime has made its complete understanding a challenge [21]. Constitutive relations were developed to describe the stress-strain relations of this regime, but these are specifically tuned to their own flow/geometrical configurations.

In our previous work [22], [23], with the help of a bench-scale experimental setup, studies were conducted to identify the influence of different geometrical parameters on granular flows.

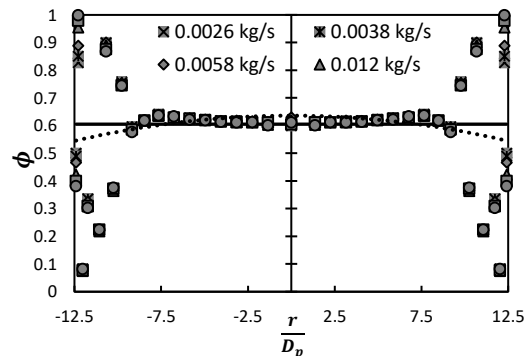
The setup was designed to let ceramic particles (Si-Zr) flow in a vertical tube under the action of gravity. The inlet of the tube was connected to a funnel on the top that serves as the particle reservoir while the exit of the tube is fixed with an orifice. The orifice constricts the flow and maintains a dense particle packing inside the tube. Experiments were also conducted with an inclined tube. A schematic of the experimental setup is provided in Figure 2 (a). The flow rate through the tube was controlled by orifices with different exit diameters. This behavior was characterized for different tube diameters and particle types. These results matched very well with those cited in the literature [8] and also enabled the observation of several flow phenomena. Unlike chute flows, the three-dimensional nature of tube flows makes it difficult to analyze the internal profile using flow visualization techniques. Though high-speed visualization could be attempted using a transparent tube, it would still be insufficient in predicting the internal flow structure. In addition, non-intrusive techniques prove ineffective owing to the high packing fractions of the flow [24]. Hence, computational studies were conducted to observe the intrinsic features of the flow. The particles were modeled with a Lagrangian approach by considering Discrete Element Methods (DEM) [9]. Validated with experimental results, the simulation studies helped in providing further insight into the internal flow rheology. Mean velocity profiles, flow fluctuations, packing fraction profiles and flow pressures are some of the several properties tracked with the help of DEM simulations. Some of these results are presented in Figure 2 (c) for reference. Since the interstitial air had no observable influence on the particle flow, the continuum air was not modelled in these studies. Though these studies provided valuable insights into dense granular regimes in vertical tubes, they were directed towards the rheological modelling of the flow. Hence, the previous flow simulations were further extended in this current work to understand the thermal transport in granular media.



(a)



(b)



(c)

**Figure 2:** (a) Experimental schematic used to conduct preliminary flow tests; (b) Mean velocity profiles of particles for different flow rates (x-axis is radial location inside the tube scaler with particle diameter); (c) Mean packing fraction profiles for different flow rates (x-axis is radial location inside the tube scaler with particle diameter)

The heat transfer behavior of dense granular flows has been studied sporadically [19], [25]–[28] in the past. It was observed that granular flows, when modelled with their bulk properties, overestimate the thermal behavior. This is because the particles in the wall-adjacent layer are arranged in a structured fashion leading to relatively dilute packing compared to the bulk of the flow. As a result, thermal resistance in the wall-adjacent layer increases, reducing the thermal performance. Researchers have tried to model this behavior empirically but could not develop a universally spanning relation. This is because most of these works didn't incorporate the microstructure of particles in the near-wall region. Thus, DEM studies were conducted in the current work to gain a better understanding of the different near-wall flow phenomena that are limiting the heat transfer to the flow. Studies were conducted to examine how these mechanisms vary with particle diameter, tube diameter, and flow rate. These observations were used to develop a correlation to predict the resistance to heat transfer in the wall-adjacent layer, in the form of an effective thermal conductivity. Since this was a collaborative work, the current manuscript only describes with the flow phenomena identified for the modelling, while the development and validation of the model are discussed in another paper [29]. These DEM flow studies are presented in chapter 2 of this manuscript.

In addition to the flow studies of granular media, the current work also places a major emphasis on understanding different particle-scale heat transfer phenomena. With the advent of better computational infrastructure, researchers began to adopt multi-scale modelling approaches to derive better heat transfer predictions [30]. Several techniques have been developed which can be classified into 4 groups, namely[31], 1. Discrete Bubble Models, 2. Two-Fluid Models, 3. Discrete Particle Models (DPM), and 4. Direct Numerical Simulations (DNS) methods. An example of their implementation is depicted in Figure 3.

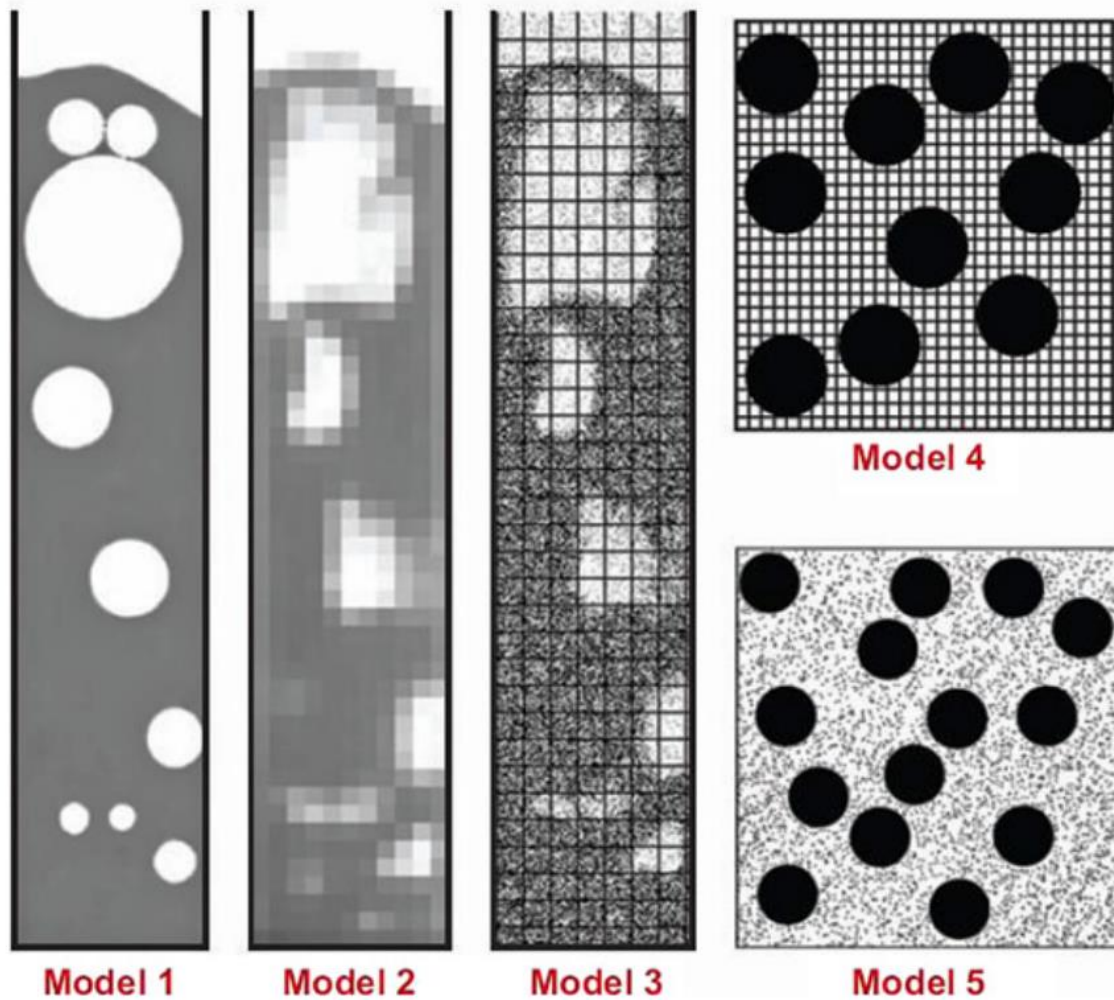


**Figure 3:** Multi-scale approach for dense fluid–particle flows comprising (1) discrete bubble model; (2) the two-fluid model based on the kinetic theory of granular flow; (3) the discrete particle model; (4) the immersed boundary model; (5) lattice Boltzmann model. (The last two models come under the DNS method) [31]

The discrete bubble model and two-fluid model are computationally simple, but do not provide particle-scale fidelity which is essential for better accuracy in heat transfer simulations. DNS methods on the other hand, provide the most accurate solutions and offer the possibility to directly compute the fluid-particle interactions. But they are computationally intensive and may

not be the best option for simulations with huge number of particles. Hence, Discrete Particle Models (DPM) stand as the one method that can produce good accuracy with less computational expenditure. This is because DPM captures the actual particle packing arrangements while avoiding the need to resolve the intra-particulate phenomenon. Building upon this approach, researchers are now starting to use the Discrete Element Method (DEM), a popular DPM approach, to derive better thermal predictions. Unlike in the flow rheology studies, the implementation of DEM for heat transfer simulations also requires the modelling of the interstitial air too. As a result, the discrete modelling of particles needs to be coupled with a continuum modelling of interstitial air. In the current study, the Finite Volume PISO solver is coupled with the DEM solver to perform CFD-DEM coupled heat transfer simulations.

In general, the accuracy of CFD-DEM coupled simulations relies on the applicability of the closure models that capture the different particle-scale heat transfer modes that exist in granular media. Theoretical analyses in the literature suggest the existence of several modes of heat transfer in flowing granular media [32]. Since it is beyond the scope of our research to analyse all of them, the heat transfer studies in the current work are restricted to static bed configurations. Typically, two modes of heat transfer are considered when modelling the thermal behavior of particles – 1. Particle-Particle contact conduction, and 2. Particle-Air convection. Over the years, several models have been developed to capture the physics of these phenomena [32]–[34]. The conduction model can be applied in a standard DEM methodology for particles, while the convection model is applied in the finite volume CFD solver for the interstitial fluid. Chapter 3 presents a detailed description of this approach.

Preliminary CFD-DEM analyses of packed beds resulted in severe underestimation of thermal performance. The effective thermal conductivities (ETC) were found to be very low

compared to experiments. It was hypothesized that the closure models were inaccurate and required more work. To gain a better understanding of the particle-scale heat transfer phenomena, a modified DNS modelling approach called Particle-Resolved DNS (PR-DNS) was also implemented in the current study. It involves the use of DEM to get a realistic unstructured packing of particles. This data is further used to develop a 3-dimensional mesh with two separate elements – one for the particles and other for the interstitial air. Finally, the Finite Element Method (FEM) is used to solve the energy equation on this mesh. A detailed description of this methodology is presented in chapter 4. In addition to the conduction and convection heat transfer, PR-DNS analyses confirmed the existence of an entirely different heat transfer mode, which carries heat from one particle to another particle via interstitial air. The physics of this phenomenon – streaming heat – was studied and is described in chapter 4.

With the observations made from the PR-DNS simulations, a theoretical model was developed in chapter 5 to capture the streaming heat transfer between two neighboring particles. Cheng et al. [35] proposed two models to capture this phenomenon by making use of Voronoi Tessellation [36] of packed beds. Though these models increased the accuracy of the ETC predictions in packed beds, they do not explicitly capture the influence of intra-particulate thermal gradients on the heat transfer physics. As a result, the accuracy of these models might suffer for larger particle radii and high solid-fluid conductivity ratios. These issues are circumvented by fine tuning the proposed streaming model with a comprehensive dataset generated from PR-DNS results. All these results and discussions are presented in chapter 5.

Finally, the proposed streaming model was implemented in CFD-DEM simulations of packed beds and the results were compared with the benchmark data obtained from PR-DNS

studies. The model was found to have a wide range of applicability in terms of void fractions, thermal properties and particle size. This discussion is also presented in chapter 5.

## Chapter 2

# DEM Study of Dense Granular Media

The multiphase modelling of dry granular flows deals with the exchange of momentum between the continuum and dispersed phases – air and particles. This was resolved by implementing a Lagrangian method. In dense flow regimes, due to the high packing fractions of the dispersed phase (~60%), the inter-particulate interactions become frequent and accounting for their behavior is necessary to resolve the flow state. Though the continuum can be solved using the conventional Navier-Stokes equations, the collisional and contact interactions of the particles among themselves and with other boundaries need to be modelled for a precise simulation of the flow. This was achieved by considering the Discrete Element Method (DEM) which computes contact forces for every particle. The following sections describe how the simulation modelling was done in this research.

The Lagrangian Multiphase model solves the equations of motion for representative parcels of the dispersed phase as they pass through the solution domain. This method is primarily suited for systems that consist mainly of a single continuous phase carrying a small volume of discrete particles, droplets, or bubbles [37]. Using this approach is the best way to resolve interactions of the discrete phase with physical boundaries.

The Discrete Element Model is an extension of the Lagrangian Multiphase approach. In this approach the inter-particulate contact forces are explicitly accounted. For this numerical approach is typically suited for simulating motion of many interacting discrete objects that are usually solid particles. Though DEM modelling requires significant computing power, it provides a detailed resolution that other approaches cannot achieve. This model was primarily established by Cundall and Strack [9], where the inter-particle contact forces are included in the equations of motion.

The application of DEM can be broadly classified into two types – hard-particle and soft-particle approaches. While the former is suitable for rapid granular flows, the latter which allows multiple and enduring contacts between particles is appropriate for dense flows [38]. Thus, the soft-particle approach was chosen in the current study. Here the term “soft-particle” refers to the fact that the particles can deform during a contact. But calculating the structural deformation of every particle in the simulation would be computationally intensive. To avoid that, each particle is considered to remain geometrically rigid but is allowed to overlap with contact boundaries. The amount of overlap is considered analogous to the deformation at the contact boundary and the interaction forces are computed from the amount of overlap using different contact models. Since the deformations of the individual particles are relatively small in comparison with the deformation of the granular assembly (which is primarily due to the movements of the particles as rigid bodies) this assumption will not lead to un-realistic solution states. Hence, the soft-particle approach can give a good representation of the mechanical behavior of the system. The contact duration is finite, and multiple contacts may occur simultaneously with this approach. The soft-particle approach is a more flexible method as compared to the hard-particle method because of the variety of force

models and particle shapes that can be accounted for. On the other hand, it is typically a more time-consuming approach due to necessary small integration time steps

Typically, DEM includes three steps – 1) contact and overlap detection, 2) force calculation and 3) particulate motion. These individual computations are done continuously to update the state of the particles (position and velocity vector of its center) and the flow. The calculations performed in the discrete element method alternate between the application of contact-force laws and the Newtonian displacement laws. The solution state of each particle in the DEM methodology includes the particle centroid location, particle radius, particle velocity and the forces acting on each particle. The particle-particle overlap is calculated using the particle centroid locations. The following sections describe the governing equations involved in calculating the contact forces and the resulting particulate motion.

## **2.1 Governing Equations**

In the Discrete Element Method, the contact forces are usually divided into two components – normal component and tangential component as shown in Figure 4. The contact force formulation is considered as a variant of the spring-dashpot model. The spring model is used to generate the repulsive forces that act while the particles push against each other. On the other hand, the dashpot model represents the viscous damping forces that come into action when the particles have sustained contact. In this way, the spring model signifies the rigidity of the particles in contact and the dashpot model signifies the inelasticity of the collisions among them. To resolve the forces in both directions – normal and tangential, the particulate contacts are modeled as a pair of spring-dashpot oscillators with one for each component.

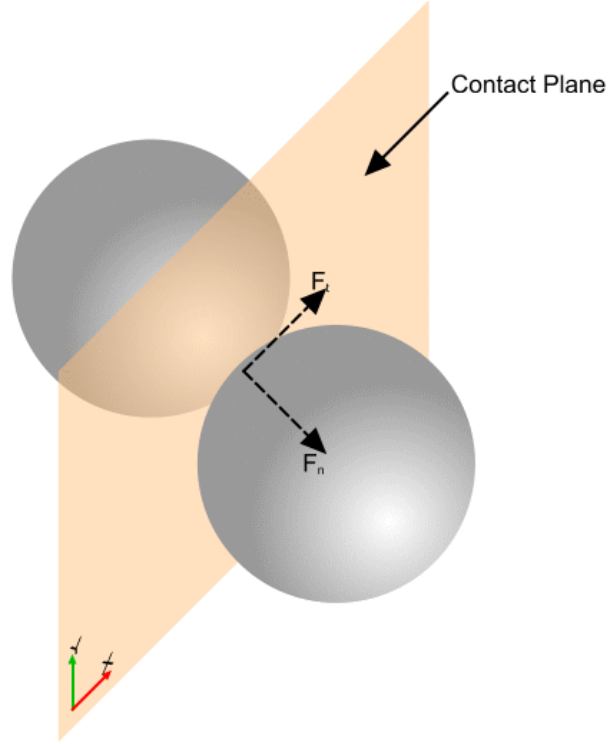


**Figure 4:** Particle contact force formulation on the contact plane

In the current simulation studies, the Hertz-Mindilin no-slip contact model is used for modelling the particle-particle and particle-wall contacts. This model is based on the Hertz-Mindilin contact theory[39]. As described above, the contact force is divided into normal and tangential components as follows:

$$F_{contact} = F_{normal} + F_{tangential} \quad (1)$$

Each force is calculated from the amount of overlap and the approach velocity at the point of contact; the former for repulsive and the latter for damping. Based on this, the repulsive normal contact forces are determined using the following equation:

$$F_N = -K_N O_N - N_N V_N \quad (2)$$

where  $K_N$  is the normal spring stiffness,  $O_N$  is the normal overlap,  $N_N$  is the normal damping coefficient and  $V_N$  is the normal approach velocity at the contact point. The subscript  $N$  in all these

relations represent the normal direction. The normal spring stiffness is computed using the following equation

$$K_N = \frac{4}{3} E_{eq} \sqrt{O_N R_{eq}} \quad (3)$$

where  $E_{eq}$  and  $R_{eq}$  are equivalent Young's modulus and equivalent radius. They are computed as follows:

$$E_{eq} = \frac{1}{\frac{1 - \nu_A^2}{E_A} + \frac{1 - \nu_B^2}{E_B}} \quad (4)$$

$$R_{eq} = \frac{1}{\frac{1}{R_A} + \frac{1}{R_B}} \quad (5)$$

where  $E_A$  and  $E_B$  are Young's moduli of the two particles in contact and  $\nu_A$  and  $\nu_B$  are the Poisson coefficients. The terms  $R_A$  and  $R_B$  are the radii of the two particles. On the other hand, the normal damping coefficient is computed using the following equation:

$$N_N = \sqrt{(5K_N m_{eq})} n_N^{damp} \quad (6)$$

where  $m_{eq}$  and  $n_N^{damp}$  are the equivalent mass and normal damping parameter. They are computed as

$$m_{eq} = \frac{1}{\frac{1}{m_A} + \frac{1}{m_B}} \quad (7)$$

$$n_N^{damp} = \frac{-\ln(C_N^{rest})}{\sqrt{\pi^2 + \ln(C_N^{rest})^2}} \quad (8)$$

where  $m_A$  and  $m_B$  are the masses of the two particles in contact. Here,  $C_N^{rest}$  is the normal coefficient of restitution between the two particles at the contact surface.

The contact forces in the tangential direction have similar relations only if the magnitudes are less than the maximum possible value – the static friction value from the Coulomb friction law.

As a result, the tangential force representations take the following form:

$$F_T = -K_T O_T - N_T V_T \quad \text{if } |K_T O_T| < |K_N O_N| C_{fs} \quad (9)$$

$$F_T = (|K_N O_N| C_{fs}) \frac{O_t}{|O_t|} \quad \text{if } |K_T O_T| > |K_N O_N| C_{fs} \quad (10)$$

where  $K_T$  is the tangential spring stiffness,  $O_T$  is the tangential overlap,  $N_T$  is the tangential damping coefficient and  $V_T$  is the tangential approach velocity at the contact point. Here,  $C_{fs}$  represents the static friction coefficient between the contact surfaces. With subscript,  $T$  representing the tangential direction, all the properties are calculated in similar way as in equations (4)-(9) except for the tangential spring constant, which is a function of equivalent shear modulus,  $G_{eq}$ . It is calculated as:

$$K_T = 8G_{eq} \sqrt{O_t R_{eq}} \quad (11)$$

Here, the equivalent shear modulus is calculated as follows:

$$G_{eq} = \frac{1}{\frac{2(2 - \nu_A)(1 + \nu_A)}{E_A} + \frac{2(2 - \nu_B)(1 + \nu_B)}{E_B}} \quad (12)$$

For particle-wall collisions, the formulas and the computations stay the same, but the wall radius and masses are assumed to be  $R_{wall} = \infty$  and  $M_{wall} = \infty$ . In this case, the equivalent radius is reduced to  $R_{eq} = R_{particle}$  and the equivalent mass would be  $M_{wall} = M_{particle}$ . Once these forces are computed, the net force on a particle, resulting from both the normal and tangential components of particle-particle and particle-boundary contacts, is calculated in the following manner:

$$F_{Contact} = \sum_{Neighboring\ Particles} F_c + \sum_{Neighboring\ boundaries} F_c \quad (13)$$

These are used in the momentum balance equation of the material particles as follows:

$$m_p \frac{dv_p}{dt} = F_{Fluid} + F_B + F_{Contact} \quad (14)$$

where  $F_B$  represents the body forces on the particles including gravity, while  $F_{Fluid}$  represents the surface forces that include the pressure gradient force and drag force from the surrounding air. Here  $m_p$  and  $v_p$  are the mass and velocity of each material particle. Similarly, the DEM particle equations of motion incorporate angular momentum conservation equations as:

$$\frac{d}{dt}(I_p \omega_p) = \sum_{Neighboring\ Particles} T_c + \sum_{Neighboring\ boundaries} T_c \quad (15)$$

where  $I_p$  and  $\omega_p$  are the moment of inertial and angular velocity of the particle. The contact torque is computed from the contact forces on the particles as:

$$T_c = r_c \times F_{Contact} - \mu_r |r_c| |F_{Contact}| \frac{\omega_p}{|\omega_p|} \quad (16)$$

where  $r_c$  is the vector from the particle's center of gravity to the contact point and  $F_c$  is the contact force acting on the particle. Here  $\mu_r$  is the coefficient of rolling friction.

From these momentum balance equations, the linear and the angular velocity at the updated time-steps are calculated. Using these values, the new position of the particulate network is calculated, and this cycle is repeated. Like the contact forces, the lift/drag forces can also be modelled using different techniques available in the literature. But in the current dense particle simulation study, it was observed that there was no noticeable influence of the interstitial air on the particles. To validate this, two set of simulations were conducted, one by considering the particle-continuum coupling and one without the coupling. In both the studies, the particulate velocities, the particulate flowrates and all the other parameters of the granular flows remained

virtually the same. In addition, the computational time of the problem was drastically reduced when the coupling was removed. Hence, all the simulations studies in the current research were conducted by ignoring the lift/drag/torque forces on the particles from the continuum and the particle motion was only governed by the gravitational force and collision interactions with other particles and rigid boundaries.

The governing equations of the particles were solved numerically in the Cartesian coordinate system. Since the interstitial air and the particles were completely de-coupled, the momentum equation of the continuum was not solved in the current studies. As a result, a coarser mesh was used as the grid resolution had no direct influence on the flow. The general purpose CFD code STAR-CCM+ [37] was used as the numerical solver to explicitly integrate the governing equations. Attempts were made to solve the problem on multiple processors to accelerate the computational speed, but since the number of particles in each simulation are very large, the data transfer and communication among each processor for the computations increased and slowed down the solution even with the slightest increase of processors. Hence, all the studies were conducted on a single core using an Intel<sup>®</sup> Xeon<sup>®</sup> E5-2687W processor.

A first order temporal discretization was used for the advancement of the solution state. A major assumption in DEM simulations is that the effect of contact between two particles is localized and does not propagate to the neighboring particles within a time-step[9]. Thus, the time step size needs to be restricted for these computations. This was done by limiting it to the time it takes the Rayleigh wave to propagate across the surface of the sphere to the opposite pole [39][40].

This time is calculated as:

$$\tau_1 = \pi \frac{R_{min}}{V_{Rayleigh}} \quad (17)$$

where  $R_{min}$  is the minimal particle radius. The Rayleigh wave velocity depends on the material properties of the particle. In addition, the time-step size is also limited by the duration of impact of two perfectly elastic spheres. This time is calculated as[41]:

$$\tau_2 = 2.94 \left( \frac{5\sqrt{2}\pi\rho}{4} \frac{1-v^2}{E} \right)^{\frac{2}{5}} \frac{R}{\sqrt[5]{v_{impact}}} \quad (18)$$

Finally, the third restriction on the time step size assumes that particles must not move too far within the time-step. This prevents missing contacts between DEM particles as well as particles and the wall. Thus, each particle is constrained such that it takes at least 10 time-steps for the particle to move a distance of one radius. Thus, the restriction is formulated as

$$\tau_3 = \frac{R}{10 v_{particle}} \quad (19)$$

## 2.2 Simulation Setup

The geometry was modelled with a batch funnel on the top of the tube and an orifice at the exit. Before any flow was initiated, the entire solution domain was filled with particles by keeping the exit orifice closed. The particles were added at every time step into the solution domain and allowed to settle in the tube and the funnel due to the gravitational force acting on them. This was done by assigning a lattice structure in the solution domain and by adding particles at every lattice point, if a free space was available. In this way, the amount of computational effort in setting up the simulation (adding particles alone) was avoided. Figure 5 gives a clear representation of the process. Once the entire solution domain is filled completely, the flow is initiated by removing the orifice. Finally, the required solution scalars and vectors are recorded at every time step and further post-processing was done to obtain necessary and meaningful results.

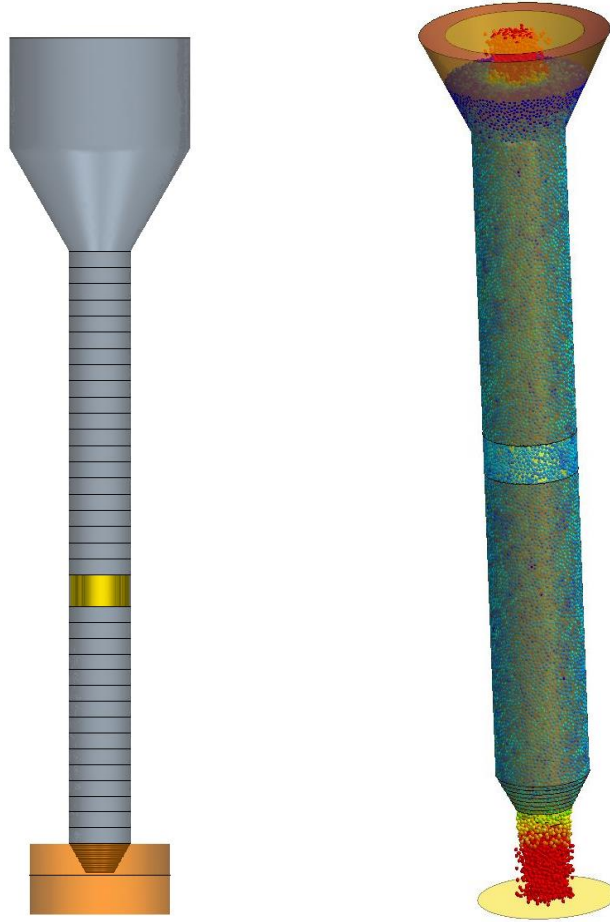


**Figure 5:** Simulation geometry without and with particles (left to right)

All the simulation studies were conducted with only a vertical configuration. Initially, a very long tube was modelled in the simulation. But as a result, the number of particles in the solution domain was huge, slowing down the computational process. Since the previous studies confirmed that the height of the tube didn't have a strong influence on the overall flow phenomena[22], to reduce the computational cost, the simulations were done with shorter tube lengths.

In the current research, each of the simulation cases with a specific tube diameter, tube length, and particle diameter were performed with different orifice opening diameter. This was done to observe the flow physics for different flow rates. It was mentioned earlier that every

simulation takes a considerable amount of computational effort and solution time to fill the domain with particles. Hence, the simulation geometry was modelled in such a manner that the filling was performed only once for each tube diameter and length, and the orifice openings were changed after being filled.

The particle-particle frictional properties were obtained by matching the experimentally determined angle of repose. The particle-boundary (tube-wall) friction was obtained by matching the flow rate of one orifice size to its experimental value and validating it with other orifice sizes. The restitution properties, were found to have no influence on the dense regime flows [15] considered here. Hence, a typical value was selected for the simulation. The structural properties of the particles and the boundary (tube-wall) were chosen to be the standard values of the respective materials. To reduce computational complexity, we used mono-sized spherical particles of with uniform properties. The particulate properties used for our simulation are listed in Table 1.

**Table 1:** Particle Properties for the Simulation Studies

<b>Diameter</b>		0.0003 m
<b>Density</b>		3934.06 kg/m <sup>3</sup>
<b>Young's Modulus</b>		75800 MPa
<b>Poisson's Coefficient</b>		0.235
<b>Static Friction Coefficient</b>	Particle-Particle	0.8
	Particle-Wall	0.5
<b>Rolling Friction Coefficient</b>	Particle-Particle	0.001
	Particle-Wall	0.001
<b>Normal Restitution Coefficient</b>	Particle-Particle	0.6
	Particle-Wall	0.5
<b>Tangential Restitution Coefficient</b>	Particle-Particle	0.8
	Particle-Wall	0.5

## 2.3 Particle-Wall Contact Behavior

Since a primary objective of the current research is to evaluate the usage of dense granular media as heat transfer fluids, the particle-wall contact behavior becomes an important parameter to observe. Similar to the case with continuous fluids, the overall heat transfer in granular flow includes two mechanisms – radial conduction of heat from the tube wall to the particles and axial convection of heat by the particles in the direction of the flow. Radial conduction involves transfer of heat from one particle to another due to the contact between them, while axial convection includes transfer of heat energy by the bulk motion of particles moving in the flow direction. While the latter is primarily a function of the velocity profiles and flow rate magnitudes, the radial conduction is primarily governed by the temperature profile and the particle to wall contact behavior. Hence it is tantamount to study this phenomenon for particulate flows.

The contact behavior was studied by counting the number of particles that come in contact with tube wall at any time instant. This was observed per unit tube wall area. The simulation geometries were like those described in previous sections with particle flow rate being controlled by different orifice diameters. In Figure 6, the variation of particle-wall contact behavior was observed with different particle sizes – 300, 450, and 600 microns. To maintain homogeneity, the orifice size in each case was tuned in such a manner that all cases have equal mass flow rates. It can be observed that with increasing particle diameter, the number of contact points is reduced. At this point of discussion, it is important to note that the contact stiffness and damping coefficients in the DEM contact models are a function of particle geometry. As a result, the larger the particle diameter, the smaller the stiffness of the contact points. As a result, larger particles end up having more overlap as compared to the smaller particles for similar loading conditions. Since the amount of overlap between two particles is directly analogous to the contact area, it is natural to understand

that larger particles have higher particle-wall/particle-particle contact area as compared to smaller particles. This was observed in the simulations where the average particle-wall contact area for a single contact point increases almost linearly from  $1.10\text{E-}08 \text{ m}^2$  to  $2.01\text{E-}08 \text{ m}^2$  for particle diameters varying from 300 to 600 microns. Though this may counter the effect of reducing number of contacts, the overall particle-wall contact area per unit tube wall area still decreases with increasing particle diameter. This can be observed from the secondary axis of Figure 6.

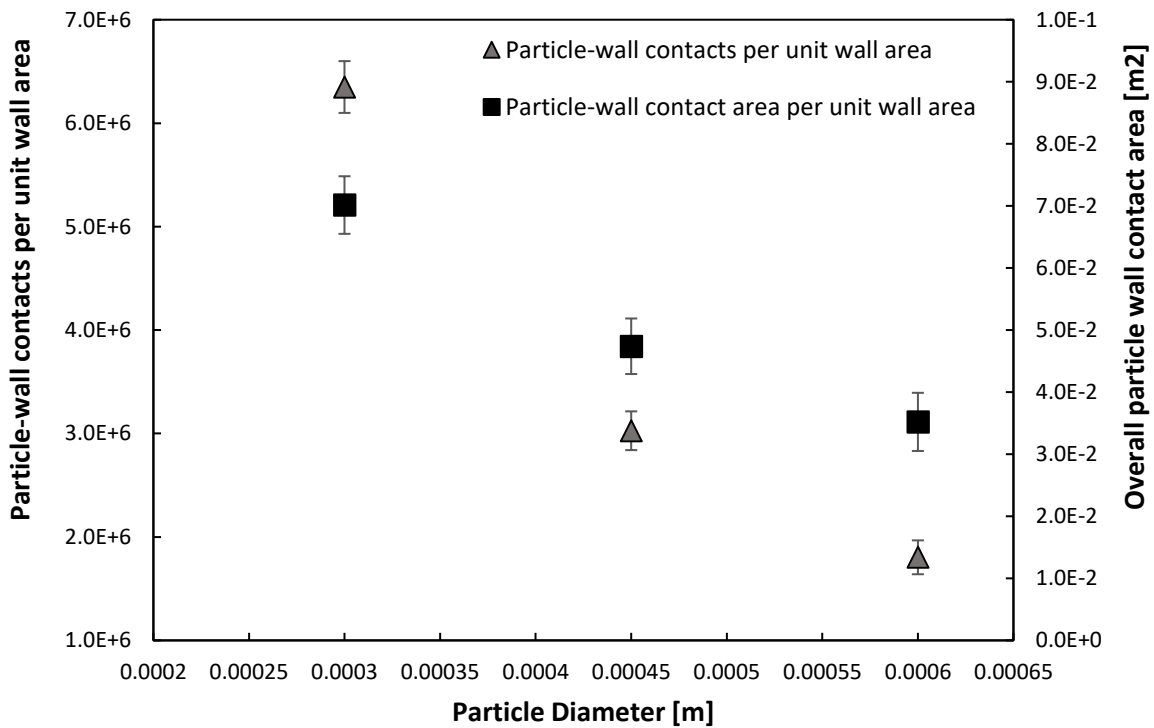


**Figure 6:** Particle-wall contact behavior with different particle diameters in 0.007747m inner diameter tube

In general, the conduction between a single particle and the tube wall, which is the first line of radial conduction, depends on the magnitude of contact area. Since Figure 6 suggests that the overall particle-wall contact area decreases with increasing particle diameter, radial conduction from the tube wall to the particulate flow is expected to decrease with increasing particle diameter.

Thus, for a similar flow rate where the axial convection remains the same, increasing the particle diameter may result in weaker heat transfer owing to poor thermal contact behavior. This was in fact observed in the experimental runs conducted in a previous study. [18]. In a previous study, it was also observed that that the packing fraction decreased with increasing particle diameter (~3% reduction). So finally, it can be concluded that the smaller the particle size, the higher the heat transfer rate. This statement would be valid only if the particle thermal properties remained the same and if there is no detrimental influence from the static charge forces for smaller particles.

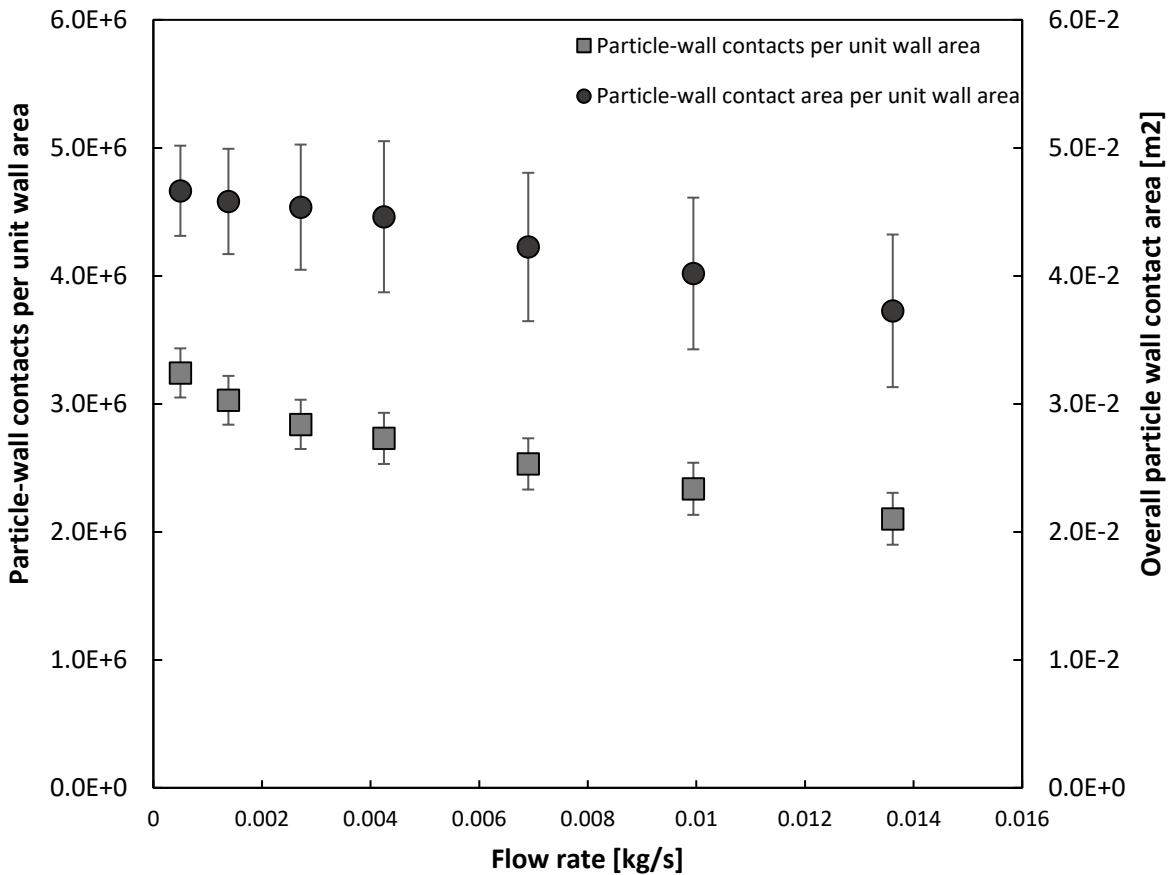


**Figure 7:** Particle-wall contact behavior with different flow rates in 0.007747m inner diameter tube

Studies were also conducted to understand the influence of flow rates on the particle-wall contact behavior by keeping the particle size constant. From Figure 7, it can be understood that the number of particle-wall contacts per unit area decreases with increasing flow rates. On the other hand, though not plotted in Figure 7, it was observed that the individual particle-wall contact area with increased with increasing flow rate. This could be due to the increased agitation of the particles at higher flow rates. As a result, the higher approach velocity of each collision at higher flow rates may lead to higher contact deformation and thus larger contact area. In spite of this phenomenon counteracting the reduction of particle contacts, the overall particle-wall contact area still decreases with increasing flow rate. Hence it can be expected that with increasing flow rates, the radial conduction from the tube wall to the particle flow decreases. Comparing the secondary axes in Figures 6 and 7, it can be observed that the variation in the overall particle-wall contact area with flow rate is relatively smaller as compared with changing particle diameter. In a previous experimental study [18], it was observed that the convective heat transfer coefficient increases with increasing flow rate, despite the currently predicted reduction in particle contact rate with flow rate. To understand this behavior, further analyses were conducted to study the average time a particle stays in contact with a wall section while it traverses along it.

## **2.4 Residence Times and Fluctuations**

Residence time in the current discussion is defined as the amount of time a particle remains in contact with the tube wall. This was computed by associating a time counter to every particle in the simulation domain and by running the counter whenever the particle stays in contact with the tube wall. An average of all the non-zero values of these time counters gives the average particle-wall contact residence time. To make this value independent of the length of the tube wall, the

final value is divided by this magnitude. This metric not only gives a qualitative sense of the contact behavior, but also helps in the direct quantification of the particle-wall heat transfer.

In both the simulations and experiments, it was observed that particles in the outer layer of the flow cross-section continue to stay near the wall, with minimal radial displacement. These outer layer particles, as they traverse downstream, can either maintain a continuous contact with the wall or touch it intermittently. In a case where a near-wall particle always touches the wall, the residence time can directly be estimated as the reciprocal of the slip-velocity of the particles (average velocity of the first layer of particles adjacent to the tube wall). This quantity – defined as Estimated Residence Time – is calculated for different flowrates and is plotted in Figure 8. The actual Residence Time, calculated by the previously mentioned method, is also plotted in Figure 8, and a comparison is made between the two quantities.

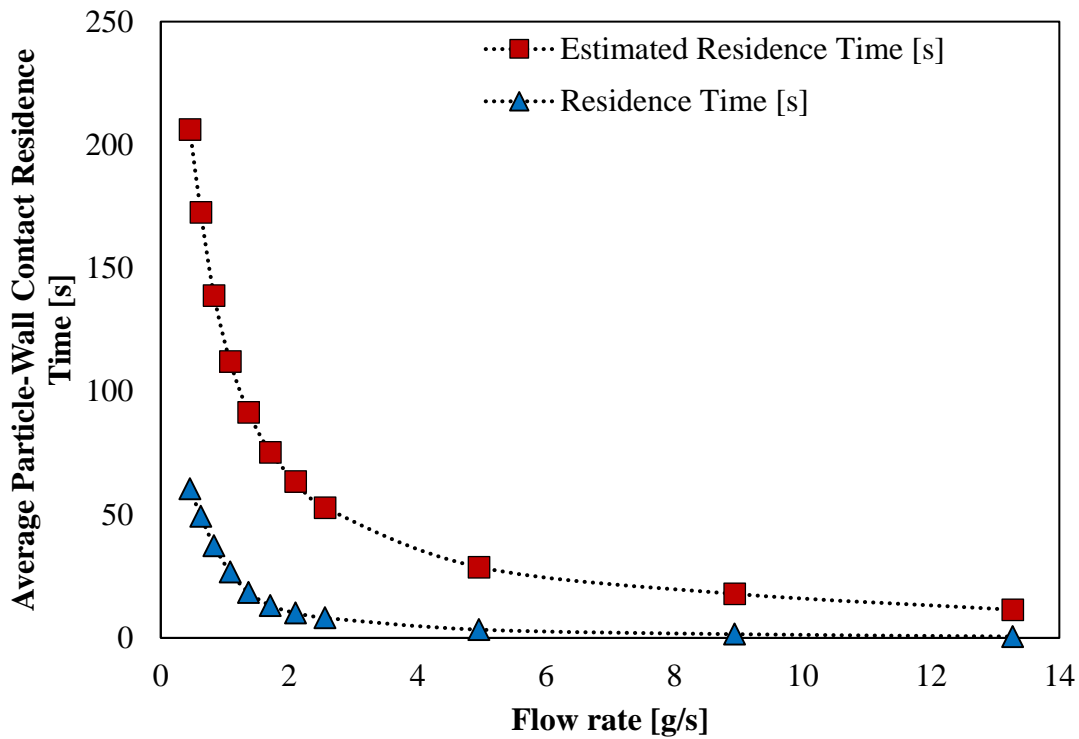
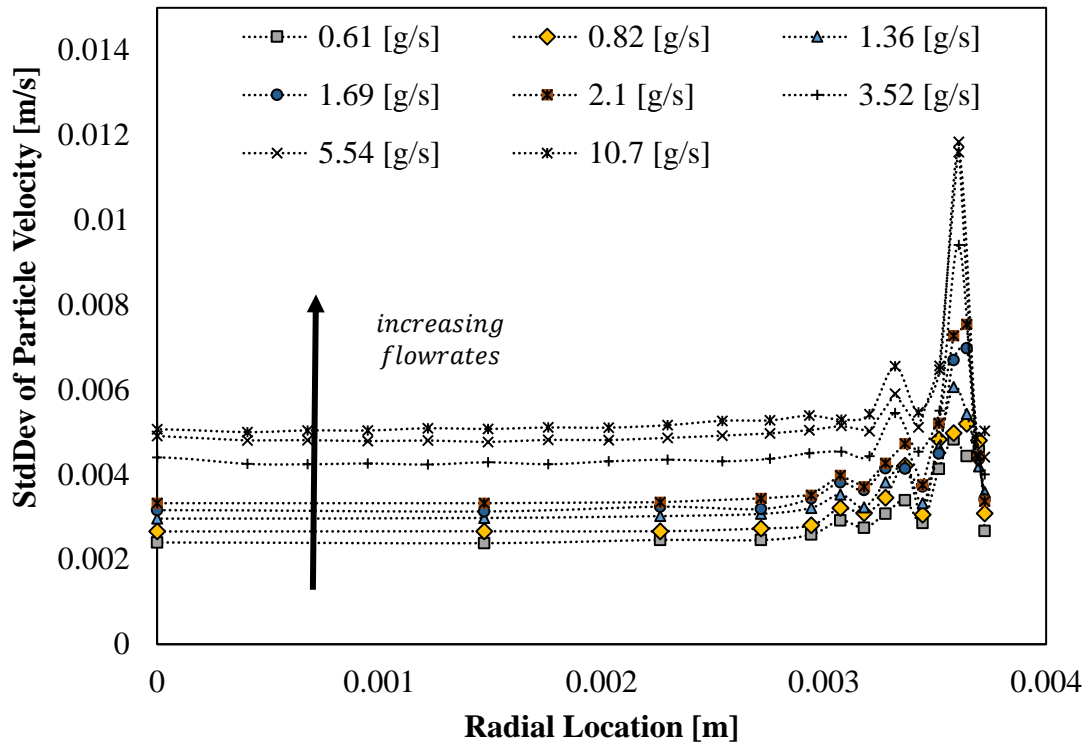


**Figure 8:** Variation of average particle-wall contact residence time with flowrate

In Figure 8, it can be observed that the actual residence time is less than the estimated residence time. This indicates that the near-wall particles do not maintain a continuous contact with the wall but touch it intermittently. It is important to note that the difference between estimated and actual residence time is of no physical consequence but only a measure of the intermittency of the particle-wall contacts. Furthermore, important observations can be made from the trend of residence time with flowrates. Since the estimated residence time is a function of the slip velocity and since the velocity increases linearly with flowrate [22], the estimated residence time exhibits a hyperbolic profile with flowrate. The actual residence time also follows a similar trend, but with an offset. Note that the difference between the estimated and the actual value decreases with increasing flowrates. This suggests that the intermittent particle-wall contact events occur more often as the flowrate increases.

Since the flow fluctuations play a crucial role in “mixing” that could impact the heat transfer behavior [18], [19], standard deviations of the particle velocity are also studied. In Figure 9, radial profiles of the particle axial velocity standard deviation are plotted for different flowrates. For all the flow rates, it can be observed that the standard deviation is uniform near the central core and is higher and varying in the shear layer. This profile is very similar to the mean velocity profiles that we observed in our previous studies [22], [23]. The standard deviation values are higher in the shear layer as compared to the core. This is because the particles have to rearrange among themselves more often near a boundary than in the core. It can also be observed that there are local fluctuation peaks at two locations near the wall. The locations are at approximately 0.0003 m and 0.0006 m from the wall. These local peaks are due to the layered fashion in which the particles move near wall and are a result of the discrete and intermittent nature of the flow. It was

also observed that with increasing flowrates, the absolute values of the standard deviation increased.



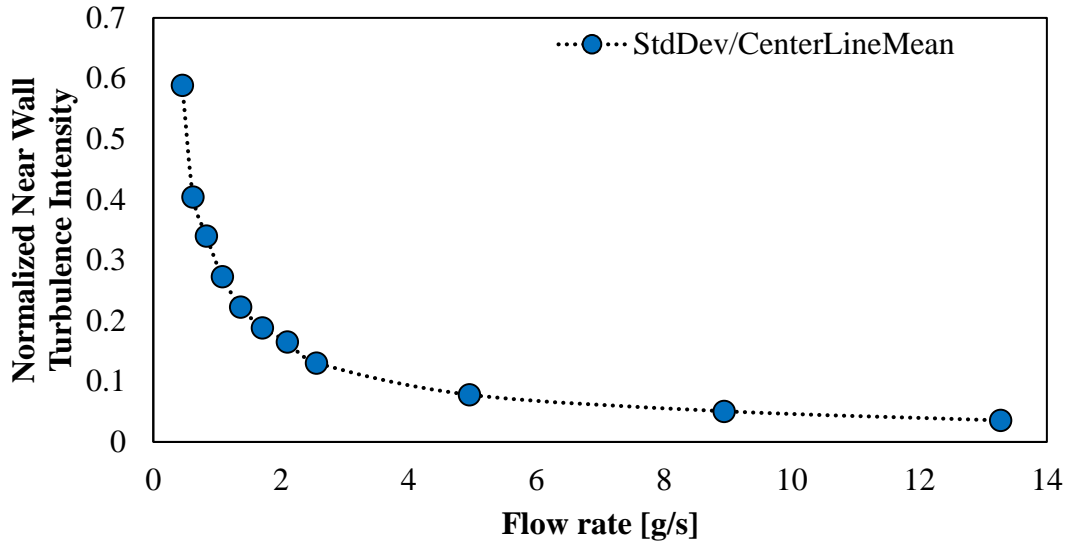


**Figure 10:** Variation of Normalized Near Wall Turbulence Intensity with different flowrates

As mentioned earlier, these observations help in gaining a qualitative understanding of the particulate mixing in granular flows – particularly near the wall. Several researchers studied the two-dimensional gravity driven granular flows in rectangular chutes and proposed constitutive relations that could explain their rheology [17], [42]. The length and time scales used in modelling these relations relied primarily on the fluctuation intensities of the granular flows. In that context, the statistical data presented in this work also serves as the first-step in the modeling of flow rheology in three-dimensional granular flows

## 2.5 Wall-adjacent Particle Mechanics

The importance of a wall on the heat transfer to a particulate bed or flow is well documented. A common approach taken to model the heat transfer from a heated surface to a particulate bed is to divide the bed into two regions: a region that encompasses the majority of the bed (often referred to as the bulk region) and a second region adjacent to the surface, with a thickness of one particle radius. The latter accounts for the increased resistance to heat transfer

due to the more ordered arrangement of particles along a surface. Each region is typically characterized by an effective thermal conductivity and/or density, which accounts for the variation in packing fraction between regions. As mentioned earlier, the bulk behavior is straightforward, but the wall-adjacent behavior is the one that needs attention. Various attempts have been made to describe the effective thermal conductivity of the wall-adjacent layer in static particle beds, ranging in complexity from simple [43] to moderately complex [44]. While most of the works studying the heat transfer to dense granular flows have acknowledged the presence of an increased thermal resistance at the wall, they have failed to provide an in-depth understanding of the heat transfer from the surface through this layer. Sullivan & Sabersky [19], for example, rely on an empirical constant determined by fitting to experimental data, while Denloye & Botterill [45] utilize relations developed for static beds. But these models are not universally spanning and have restricted applicability. The current work seeks to fill this gap by incorporating the influence of wall-adjacent flow phenomena into these models.

The work of Legawiec & Ziolkowski [43] was used as a guide in the derivation of an effective thermal conductivity (ETC) for the wall-adjacent layer. Since Legawiec & Ziolkowski were developing a correlation to describe the heat transfer through the contact layer of a static particle bed, they assumed that all particles in the contact layer were in contact with the wall. The heat transfer to a single particle was analyzed, considering the heat transfer through both the interstitial gas and the particle. The ETC of the wall-adjacent layer was then determined based on the number of particles in the layer, assuming each particle demonstrated the single particle heat transfer. For a flowing granular bed, the assumption that all particles in the wall-adjacent layer are in contact with the wall is no longer accurate. Though this was already depicted through the contact intermittency shown in Figure 8, Figure 11 gives a better visual understanding of the same where

the particle arrangements in the wall-adjacent layer at different flow rates are shown. The red particles in Figure 11 represent particles in contact with the wall, while the blue particles represent particles not in contact with the wall, and the yellow represents void spaces where no particle is present. For faster flowrates, the percentage of blue particles increases in the wall-adjacent layer. This emphasizes the fact that the number of particles in contact with the wall decreases with increasing flow rate. It should also be noted that the amount of void space (yellow) increases with increasing flow rate, resulting in a reduced packing fraction at faster flow rates. Thus, it is important for the model to capture these fundamental flow mechanics for better accuracy. A detailed explanation of the developed model is described in a previous publication [29]. Nevertheless, a brief description is presented here.

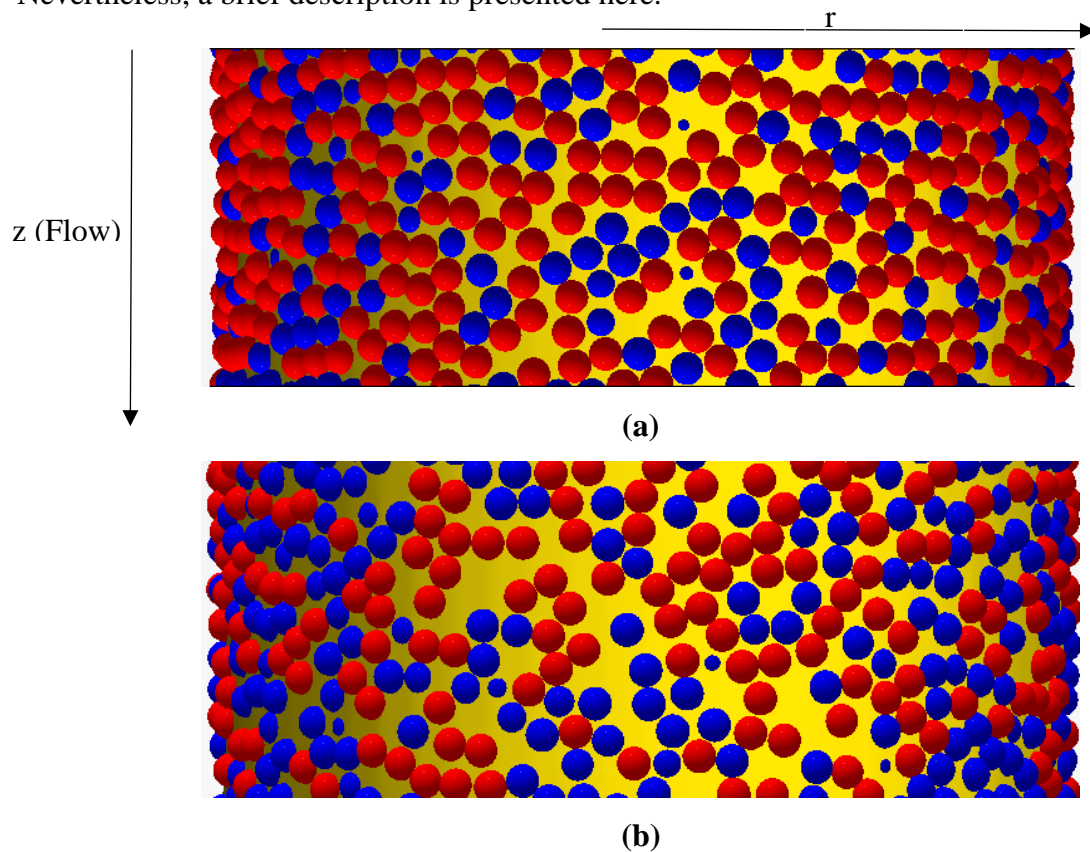


**Figure 11:** Particle arrangements in the wall-adjacent layer for mean axial flow velocities of (a) 0.023m/s and (b) 0.25m/s (using 7.75mm tube and 300 $\mu$ m particles).

The model developed assumes that the heat transfer through the wall-adjacent layer is composed of three thermal resistances: a resistance due to particles in contact with the wall ( $R_C$ ), a resistance due to particles not in contact with the wall ( $R_{NC}$ ), and a resistance due to void spaces where no particle is present ( $R_{void}$ ). Figure 12 provides a clear representation of each of these thermal resistances, with the sum of each color representing the total thermal resistance of each type.

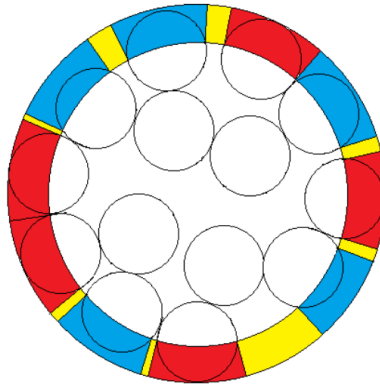


**Figure 12:** Depiction of thermal resistances used to model wall-adjacent layer heat transfer [46]. Red denotes resistance considered for contact particles, blue denotes resistance for particles not in contact, and yellow denotes resistance for void spaces.

The three resistances acting in parallel are added to calculate the total resistance to heat transfer through the wall-adjacent layer as

$$\frac{1}{R_{wa}} = \frac{1}{R_C} + \frac{1}{R_{NC}} + \frac{1}{R_{void}} \quad (20)$$

$$R_{wa} = \frac{\ln\left(\frac{R_t}{R_t - r_p}\right)}{k_{wa}} \frac{R_t}{A_{total}} \quad (21)$$

$$R_C = \frac{\ln\left(\frac{R_t}{R_t - r_p}\right)}{k_C} \frac{R_t}{A_C N_C} \quad (22)$$

$$R_{NC} = \frac{\ln\left(\frac{R_t}{R_t - r_p}\right)}{k_{NC}} \frac{R_t}{A_{NC}N_{NC}} \quad (23)$$

$$R_{void} = \frac{\ln\left(\frac{R_t}{R_t - r_p}\right)}{k_g} \frac{R_t}{A_{total} - N_C A_C - N_{NC} A_{NC}} \quad (24)$$

Here,  $R_{wa}$  represents the total thermal resistance of the wall-adjacent layer.  $k_C$ ,  $k_{NC}$ ,  $k_g$ , and  $k_{wa}$  represent the thermal conductivities for a particle in contact with the wall, a particle not in contact with the wall, the void spaces (i.e. the interstitial gas), and the wall-adjacent layer, respectively.  $A_C$  and  $A_{NC}$  represent the areas of the tube wall considered in the calculation of the heat transfer to a single particle in contact with the wall and a single particle not in contact with the wall respectively.  $A_{total}$  represents the total area of the tube wall under consideration,  $R_t$  represents the radius of the tube, and  $N_C$  and  $N_{NC}$  represent the number of particles in contact with the wall and not in contact with the wall in the area under consideration, respectively. Equations 20-24 were rearranged to solve for the ETC of the wall-adjacent layer, yielding

$$k_{wa} = k_g(1 - n_C A_C - n_{NC} A_{NC}) + k_C n_C A_C + k_{NC} n_{NC} A_{NC} \quad (25)$$

where,  $n_C$  and  $n_{NC}$  represent the number of particles with and without contact per unit wall area, respectively. To simplify the problem, all the particles not in contact with the wall were assumed to be at the same distance from the wall, yielding two groups of particles: those in contact with the wall and those at a distance  $a r_p$  from the wall (where  $r_p$  represents the particle radius). So, the remained of the section focuses on understanding the terms,  $n_C$ ,  $n_{NC}$  and  $a$  with the help of DEM simulations.

In Figure 13, the variation in the number of particle contacts per unit wall area with average flow velocity is plotted for different particle diameters. The number of contact particles was

normalized with the maximum number of possible contacts, which was defined assuming a hexagonal packing of particles along the tube wall  $\left(n_{c,max} = \frac{(1-1/A)}{2\sqrt{3}r_p^2}\right)$ .

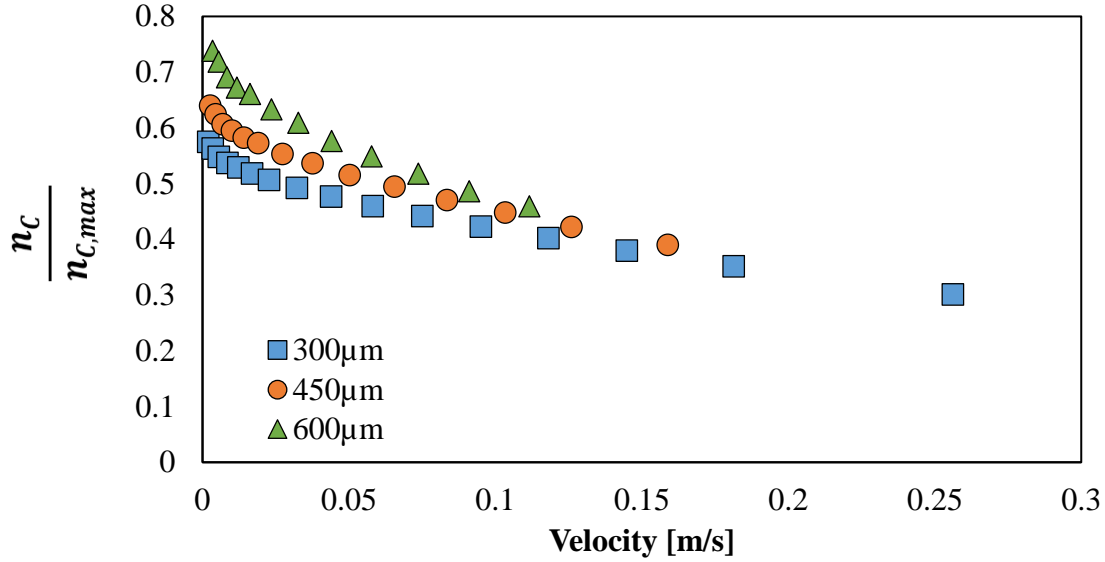


**Figure 13:** Variation in the normalized number of particle contacts per unit wall area with average flow velocity and particle diameter in the 7.75mm tube

With increasing flow velocity, the number of contact particles decrease. This can be attributed to the increased flow agitation present at higher velocities. In the previous simulation studies [47], the granular temperature was used as a metric to examine the particle fluctuations. The granular temperature, which increases with increasing velocity, yields a larger mean free path for each particle temperature increases. This leads to the particles being spaced far away at higher flowrates and a reduced number of contact points. An empirical correlation was developed to capture the trends observed in Figure 13 as:

$$\frac{n_c}{n_{c,max}} = \left(0.336 + \frac{2.122}{A^{0.665}}\right) \exp\left(-\left(0.086 + \frac{893}{A^{3.194}}\right) \frac{U}{\sqrt{gd_p}}\right) \quad (26)$$

Here,  $A$  represents the ratio of the tube-to-particle radii ( $A = R_t/r_p$ ). The correlation agrees with the simulation results to within 12%. Although this error may seem large, the error observed in  $k_{wa}$  as a result of the error in both the packing fraction and the number of contacts is less than 5%.

The variation in the fraction of particles not in contact with the wall (defined as the ratio of the number of particles not in contact with the wall to the total number of particles with partial volume in the wall-adjacent layer) with flow rate is displayed in Figure 14. As suggested by the observations made from contact particles, the non-contact particles can be seen increasing with increasing flowrates.

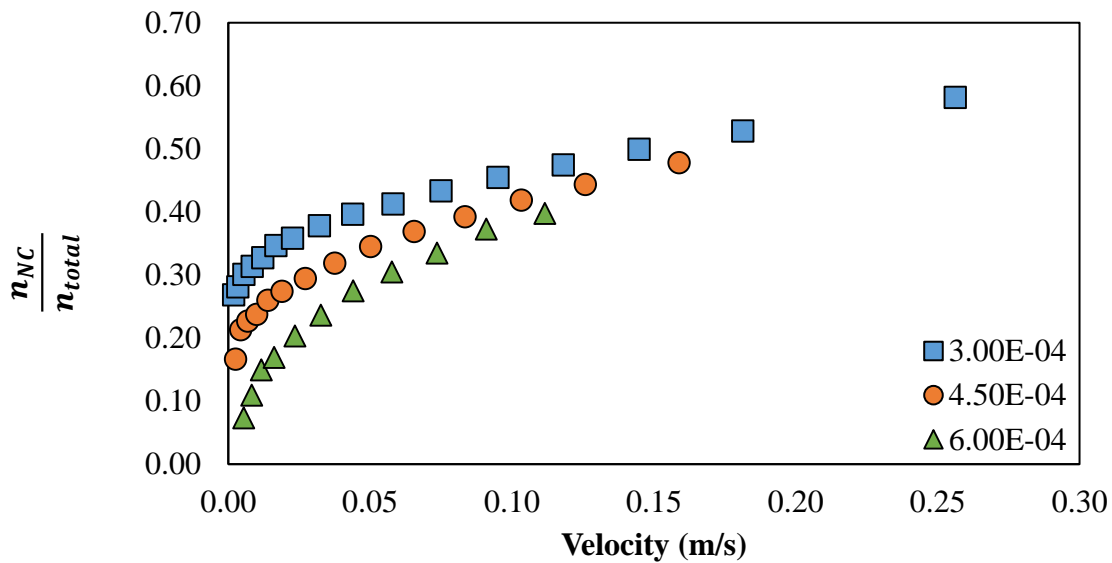


**Figure 14:** Fraction of particles in wall-adjacent layer that are not in contact with the wall as a function of mean flow velocity and particle diameter. Results for 7.75mm tube

Another parameter that the particle-wall contact heat transfer depends on is the near-wall packing fraction. Not only does it play a role in determining the bulk heat transfer properties like effective heat capacity, but it also helps in identifying which heat transfer mechanism is dominant. If the particles are densely packed near the wall, owing to the high number of particle contacts,

conduction would be the primary mode of heat transfer from the wall to particles [35], [48]. On the other hand, if the particles are loosely packed, the wall-interstitial gas plays a dominant role in the heat transfer phenomenon. Furthermore, at high temperatures, loosely packed beds near the wall also enhance the radiation heat transfer phenomenon as the photons are able to penetrate to deeper particulate layers [48], [49]. Hence, the near-wall packing fractions were calculated and their variation with increasing flowrates is plotted in Figure 15. In addition to the qualitative analyses, the wall-adjacent packing fractions can also be used to calculate the number of non-contact particles as:

$$n_{NC} = \frac{1}{V_{NC}} \left[ r_p \left( 1 - \frac{0.5}{A} \right) \phi_{wa} - V_C n_C \right] \quad (27)$$

where,  $V_C$  and  $V_{NC}$  represent the volume of a single particle in the wall adjacent layer for both particles in contact with the wall (assuming a point contact) and those particles a distance  $ar_p$  from the wall.  $A$  represents the ratio of the tube-to-particle radii ( $A = R_t/r_p$ ).

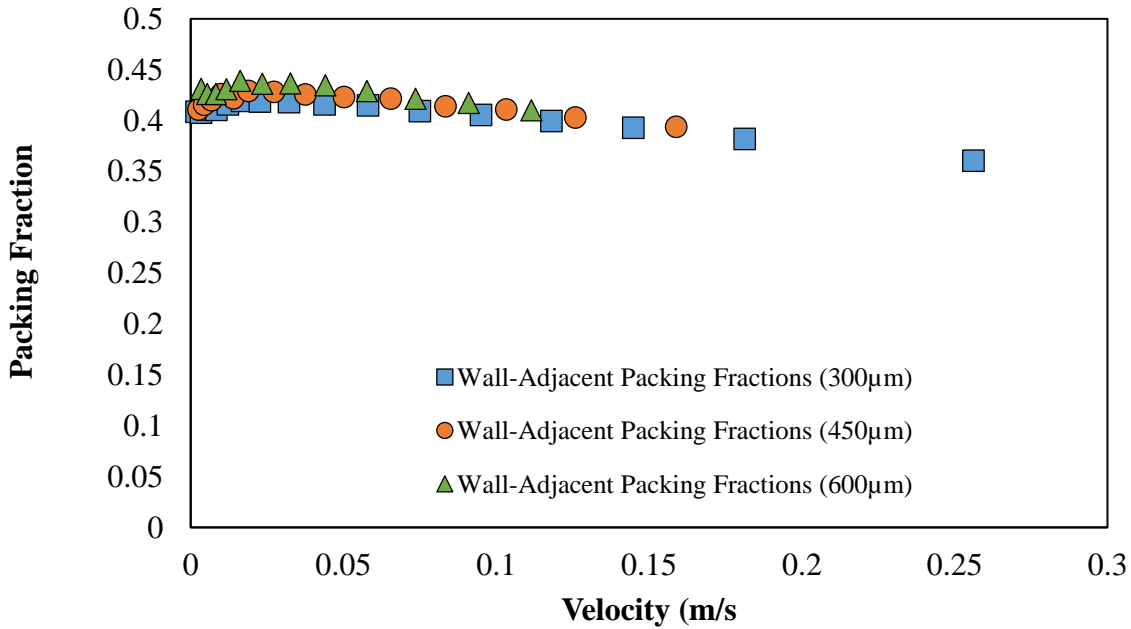


**Figure 15:** Variation of the wall-adjacent layer packing fraction

From Figure 15, it can be observed that the packing fraction decreases with increasing axial flow velocity. The packing fraction results for all test cases were used to develop an empirical correlation that can be used to predict the packing fraction for different system configurations and mean flow velocities. The correlation agrees with the simulation results within 4%.

$$\phi_{wa} = 0.405 + \frac{0.797}{A^{1.149}} - \left( 0.00147 + \frac{0.252}{A^{0.943}} \right) \frac{U}{\sqrt{gd_p}} \quad (28)$$

The decrease observed in the packing fraction can be attributed to the pressure inside the tube for dense flows. In our previous studies [22], the pressure inside the tube was observed to increase with increasing depth, saturating to a constant value, termed the saturation pressure. This observation, which agreed with the experimental investigations of Janssen [7], was attributed to the increasing frictional force between the tube and the particles with increasing depth. In general, the pressure inside a tube manifests itself by pushing the particles against the tube wall. A higher pressure thus results in a greater force with which the particles are pushed against the wall, forcing the granular media to fill in the available void spaces and thereby increasing the wall-adjacent packing fraction. Hence, we believe that the packing fraction in the wall-adjacent layer depends on the pressure inside the tube. Figure 16 displays the variation of the saturation pressure with flow velocity for different particle diameters in the 7.75mm diameter tube. The saturation pressure decreases approximately linearly, similar to that of the wall-adjacent layer packing fraction, thus corroborating the above hypothesis.

As discussed in the previous section, the average distance of the non-contact (NC) particles from the wall is also important for the simplified ETC model. This was calculated by taking the average radial location of all the NC particles in the wall-adjacent layer. Figure 17 shows the variation in ‘ $a$ ’ with the average flow velocity for different particle diameters in the 7.75mm tube. The average distance drops initially and saturates to an essentially constant value for higher

velocities. In this way, all the microscopic flow mechanics are incorporated into the heat transfer model that proved to have better accuracy and applicability [29]

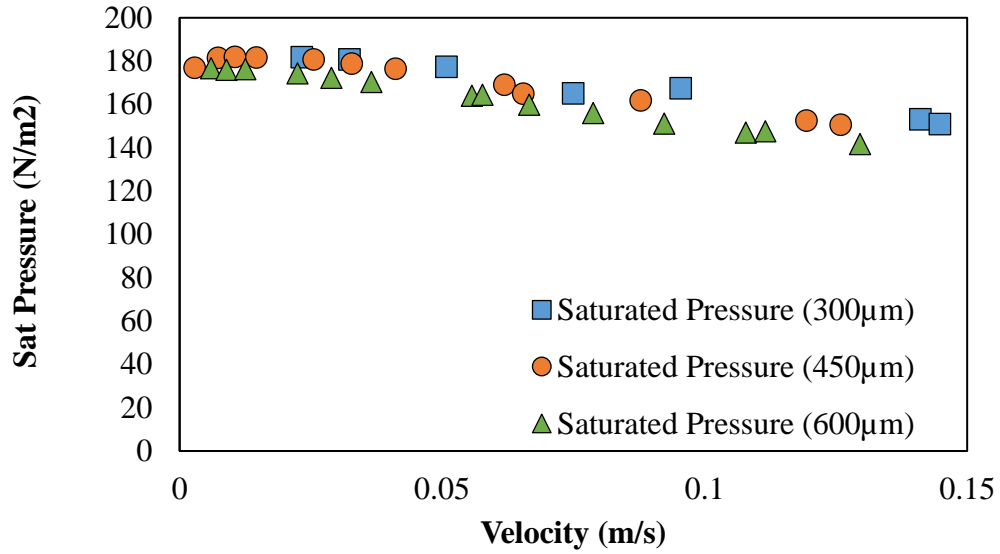


**Figure 16:** Variation of the saturation pressure with average flow velocity for different particle diameters in the 7.75mm diameter tube.

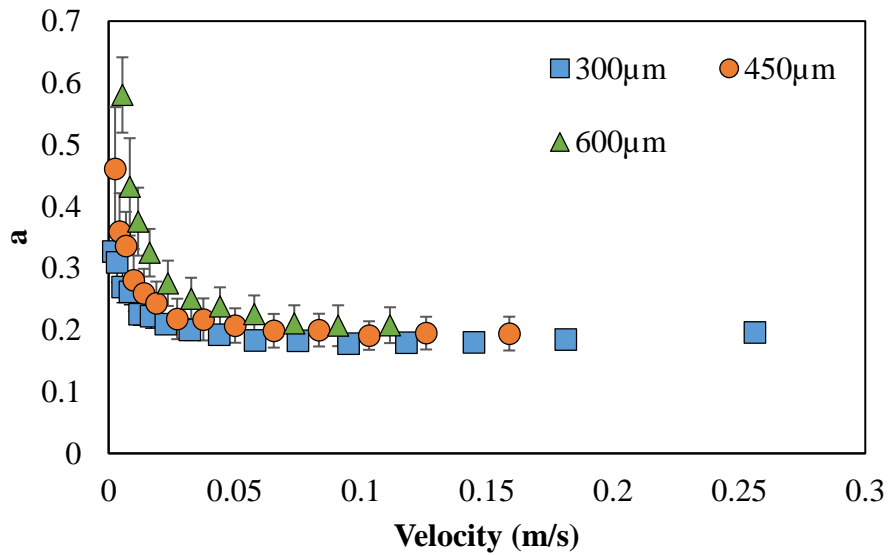


**Figure 17:** Variation in the average distance of NC particles with average flow velocity and particle diameter in the 7.75mm tube.

## Chapter 3

# CFD-DEM Coupling

It has been widely accepted that the micro-structure of particle packing has strong influence on the thermal behavior of packed beds. Since the particle arrangement varies from application to application, the best way to study the heat transfer behavior is by resolving the particle motion computationally on an application-by-application basis. Theoretical analyses in the literature suggest the existence of several modes of heat transfer in flowing granular media [32]. Since it is beyond the scope of our research to analyse all of them, the heat transfer studies in this current work are restricted to static bed configurations. As mentioned before, there exist 4 major multi-scale modelling approaches, and out of which, the Discrete Particle Models provide required accuracy at much less computational cost. Since the interstitial air has a strong effect on the heat transfer behavior of particle beds, it is important to resolve its continuum physics as well. For this purpose, the current section explores the use of Discrete Element Methods for particles and Finite Volume methods for the interstitial air by two-way coupling.

The particle motion equations of the DEM implementation were already discussed in the previous sections. As previously mentioned, the commercial software package called Star-CCM+ was used to implement the DEM algorithm to study the flow behavior of particles. But StarCCM+ does not provide enough robustness to modify the governing equations. Moreover, the

implementation of two-way coupling in Star-CCM+ is erroneous because it assuming a zero volume to the particles. Hence, an open source DEM code called LIGGGHTS was implemented for the subsequent heat transfer studies. It stands for LAMMPS improved for general granular and granular heat transfer simulations. LAMMPS is a classical molecular dynamics simulator. It is widely used in the field of Molecular Dynamics. In the most general sense, LIGGGHTS integrates Newton's equations of motion for collections of atoms, molecules, or macroscopic particles that interact via short- or long-range forces with a variety of initial and/or boundary conditions. For computational efficiency LIGGGHTS uses neighbor lists to keep track of nearby particles. On parallel machines, LIGGGHTS uses spatial-decomposition techniques to partition the simulation domain into small 3d sub-domains, one of which is assigned to each processor. Processors communicate and store "ghost" atom information for atoms that border their sub-domain [50].

In general, LIGGGHTS functionalities are executed by reading commands from an input script (text file), one line at a time. When the input script ends, LIGGGHTS exits. Each command causes LIGGGHTS to take some action. It may set an internal variable, read in a file, or run a simulation. Usually, a LIGGGHTS input script includes four parts:

1. Initialization
2. Particle Definition and Insertion
3. Simulation Settings
4. Run Commands

These four parts encapsulate all the steps that are necessary in conducting any DEM simulation. A typical LIGGGHTS input script is described in Figure 18, where particles are just added into a cylindrical domain and are allowed to settle under gravity. It can be observed that the initialization part includes defining the units of the simulation, style of the particles, simulation domain

boundaries, contact models, heat transfer models and boundary conditions. The particle definitions and insertion part define all the structural and thermal properties required for the simulation, the size of the particles, and the way they are inserted into the simulation domain. The simulation settings define the integration scheme, timestep and other necessary parameters while the run commands list the different executions required for the simulation.

```

##### Initialization #####
## Units, atom types and communication parameters
units          si
atom_style     granular
processors     2 2 1
## Simulation domain definitions
boundary       m m m
region         domain block ${xLowBlock} ${xHighBlock} ${yLowBlock} ${yHighBlock} ${zLowBlock} ${zHighBlock}
## Contact Models
pair_style     gran model hertz tangential history
pair_coeff     * *
## Heat Transfer Models (Heat conduction between particles)
fix            heatTransfer all heat/gran/conduction initial_temperature 300.00 contact_area overlap
## Geometries
fix            bottomwall all wall/gran model hertz tangential history primitive type 2 zplane ${zLowBlock}
fix            topwall all wall/gran model hertz tangential history primitive type 2 zplane ${zHighBlock}
fix            cylwall all wall/gran model hertz tangential history primitive type 2 zcylinder ${cylinderRadius} 0.0 0.0

##### Particle Definition and Insertion #####
## Material properties: Contact and thermal properties
fix            m1 all property/global youngsModulus peratomtype 5.0e6 5.0e6
fix            m2 all property/global poissonsRatio peratomtype 0.235 0.33
fix            m4 all property/global coefficientFriction peratomtypepair 2 0.8 0.4 0.4 0.8
fix            m3 all property/global coefficientRestitution peratomtypepair 2 0.06 0.08 0.08 0.06
fix            ftco all property/global thermalConductivity peratomtype ${kPart} ${kPart}
fix            ftca all property/global thermalCapacity peratomtype 1 1
## Particle properties: Material, size and density
fix            particles all particletemplate/sphere 15485863 atom_type 1 density constant 3820.0 radius constant 0.00015
## Insertion regions and group
region         insertionRegion cylinder z 0.0 0.0 ${cylinderRadius} ${zLowBlock} ${zHighBlock} units box
## Insertion distribution
fix            particleDistribution all particledistribution/discrete 15485867 1 particles 1.0
## Insertion rate parameters
fix            insertion all insert/pack seed 32452843 distributiontemplate particleDistribution vel constant 0. 0. -0.01
insert_every 500 & particles_in_region 300 region insertionRegion

##### Simulation Settings #####
## Integrator (nve for single inserted particles)
fix            integr all nve/sphere
## Time step
timestep       0.000005
## Gravity
fix            gravi all gravity 9.81 vector 0.0 0.0 -1.0
## Timestep check
fix            timeStepCheck all check/timestep/gran 1 0.01 0.01
## Output parameters
dump           dmp all custom 10000 post/dump*.liggghts_init id type x y z radius vx vy vz omegax omegay omegaz fx fy fz f_Temp[0] f_heatFlux[0]

##### Run Commands #####
## Fill and settle particles
run            5000
unfix         insertion
run            95000

```

**Figure 18:** Example of a typical LIGGGHTS simulation input script

To maintain homogeneity in the observations made from Star-CCM+ and LIGGGHTS, each and every model implemented in the former are replicated with exact parameters in the latter. Once all the simulations are validated in LIGGGHTS, modifications required for two-way coupling are implemented by changing the necessary source code sub-routines and recompiling

them. LIGGGHTS is designed in a modular fashion to be easy to modify and extend with new functionality. The source code is written in C++ with object-oriented class organization. The functions (class methods) that do actual computations are written in vanilla C-style code and operate on simple C-style data structures (vectors and arrays). The advantage of C++ and its object-orientation is that all the code and variables needed to define any new feature can be written or edited in specific files, without modifying the rest of the source code. This makes the entire process robust and causes less side-effect bugs.

With this brief description of the DEM aspect of the two-way coupling, the following sections elaborate on the governing equations for the Finite Volume side of the implementation. A short explanation of the heat transfer equations used in the DEM implementation is also presented.

### 3.1 Governing Equations

The energy equation for every particle in a standard DEM solver is applied by assuming a lumped capacitance approximation as follows:

$$m_p c_{p,s} \frac{dT_p}{dt} = \sum \mathbf{Q}_{neigh} + \mathbf{Q}_{fluid} + \sum \mathbf{Q}_{source} \quad (28)$$

Here,  $m_p$  is the mass of the particle,  $c_{p,s}$  is the specific heat capacity of the solid particle and,  $T_p$  is the temperature of the particle.  $\mathbf{Q}_{neigh}$  is the heat exchange with neighbouring particles,  $\mathbf{Q}_{fluid}$  is the heat exchange with the surrounding interstitial fluid and  $\mathbf{Q}_{source}$  is the heat generation term inside the particle. The terms  $\mathbf{Q}_{neigh}$  and  $\mathbf{Q}_{fluid}$  include the important modes of heat transfer (i.e. particle-particle contact conduction and particle-air convection). The calculation of these terms is presented in subsequent sections.

To solve for the motion of the interstitial fluid the typical Navier-Stokes equations need to be modified to accommodate for the volume occupied by the particles. This is done as

$$\frac{\partial(\rho\epsilon)}{\partial t} + \nabla \cdot (\rho\epsilon\mathbf{u}_f) = 0 \quad (29)$$

$$\frac{\partial(\rho\epsilon\mathbf{u}_f)}{\partial t} + \nabla \cdot (\rho\epsilon\mathbf{u}_f\mathbf{u}_f) = -\nabla\epsilon p + \nabla \cdot (\epsilon\boldsymbol{\tau}) - \mathbf{F}_{fs} + \mathbf{F}_{body} \quad (30)$$

Here,  $\epsilon$  is the local porosity (volume fraction of fluid in a mesh cell),  $\mathbf{u}_f$  is the fluid velocity vector,  $p$  is the local pressure,  $\rho$  is the fluid density,  $\boldsymbol{\tau}$  is the local stress tensor and  $\mathbf{F}_{fs}$  is the momentum exchange term between the solid particles and the interstitial fluid. Like equation 30, the temperature of the interstitial fluid is solved by the following transport equation.

$$\frac{\partial(\rho\epsilon c_p T_f)}{\partial t} + \nabla \cdot (\rho\epsilon c_p \mathbf{u}_f T_f) = \nabla \cdot (k_f \epsilon \nabla T_f) + \mathbf{S}_{fs} \quad (31)$$

Here  $T_f$  is the temperature of the interstitial fluid,  $k_f$  is the thermal conductivity of the fluid and  $\mathbf{S}_{fs}$  is the energy exchange term between the solid particles and the interstitial fluids. The exchange terms  $\mathbf{F}_{fs}$  and  $\mathbf{S}_{fs}$  are calculated from the terms  $\mathbf{F}_{fluid}$  and  $\mathbf{Q}_{fluid}$  in equations 14 and 28, respectively. The incompressible PISO solver of the open-source library OpenFOAM was used to solve equations 29-31. To compute  $\mathbf{S}_{fs}$ , the  $\mathbf{Q}_{fluid}$  terms of all the particles inside a mesh cell are lumped as follows:

$$\mathbf{S}_{fs} = \frac{\left( \sum_{\substack{i=No. \text{ of particles} \\ \text{inside a mesh}}} (Q_{fluid})_i \right)}{\text{Volume of mesh cell}} \quad (32)$$

### 3.2 Heat Transfer Models

As mentioned above, the computation of  $\mathbf{Q}_{neigh}$  and  $\mathbf{Q}_{fluid}$  involves the modelling of the two dominant heat transfer mechanisms – particle-particle contact conduction and particle-air

convection. The conduction model proposed by Batchelor and O'Brien [33] has been the most popular one for several decades due to its simplicity and robustness. It was derived by assuming that the heat transfer between two particles results in a temperature distribution that is approximately the same as that of the velocity potential of irrotational incompressible fluid flow through a circular hole in the wall. The solution of the analogous fluid problem was thus used to compute the heat flux through the contact area between two particles as:

$$Q_{AB}^{Cond} = 4 \frac{k_{S,A} k_{S,B}}{k_{S,A} + k_{S,B}} R_{Con,AB} (T_A - T_B) \quad (33)$$

where  $Q_{AB}^{Cond}$  is the heat exchange [W] between two contacting particles A and B, through the contact area. Here,  $k_{S,A}$  and  $k_{S,B}$  are the thermal conductivities of the particles A and B, while  $T_A$  and  $T_B$  are their corresponding temperatures.  $R_{Con,AB}$  is the radius of the contact patch area between the two particles. Note that equation 33 is a slightly modified version of the one proposed by Batchelor and O'Brien. Using this equation, the contact conduction heat rates at all the contact points are calculated and their net contribution is used in the  $Q_{neigh}$  term of equation 28.

The time-step of a DEM simulation, in general, is restricted by the Young's modulus of a particle. The higher the Young's Modulus, the smaller the time-step should be. For ceramic particles under consideration, the Young's Modulus is roughly 75000 MPa, which results in a timestep of 1E-09 sec. This time-step would drastically slow down the simulation. In the previous simulations, it was observed that the bulk flow behavior of the particles is not sensitive to the Young's Modulus. Hence, a smaller Young's Modulus can be used in general. In our cases, the particle's Young's Modulus was reduced 5 MPa, giving a timestep of 1E-05 sec. But reducing the Young's Modulus increases the particle-particle contact area, as the spring-dashpot formulation of contact forces depends on the Young's modulus of the particles. Though reducing the Young's

modulus this may not affect the flow behavior, the particle-particle heat transfer will be overestimated. From equation 3, for a constant load on a particle, we can understand that

$$Y_{particle}\delta_n^{1.5} = const \quad (34)$$

$$\delta_n \sim \left( \frac{1}{Y_{particle}} \right)^{1.5} \quad (35)$$

And since for particle-particle overlaps are typically very small, the contact area is proportional to the amount of overlap. Thus, we have

$$contactArea \sim \left( \frac{1}{Y_{particle}} \right)^{1.5} \quad (36)$$

Using the above relation, the contact area that is used to calculate the particle-particle heat transfer is scaled down from the calculated using the actual Young's Modulus of the particles, using an area correction factor. In this way, the overestimation of conduction heat transfer is resolved.

Convection heat transfer between particles and interstitial air in packed beds has been studied extensively by several research efforts. A Nusselt number ( $Nu_p$ ) is usually defined from which the convection heat transfer coefficient ( $h_{conv}$ ) can be calculated to find the particle-air heat rate ( $\dot{Q}_{fluid}$ ) as:

$$Nu_p = \frac{h_{conv}D_p}{k_f} \quad (37)$$

$$Q_{fluid} = h_{conv}A_p(T_f - T_p) \quad (38)$$

The most popular model is the one proposed by Li and Mason [34], which describes the particle Nusselt number as a function of particle Reynolds number ( $Re_p$ ), fluid Prandtl number ( $Pr$ ) and local porosity( $\epsilon$ ) as:

$$Nu_p = 2 + 0.6\epsilon^{3.5}Re_p^{1/2}Pr^{1/3} \quad Re_p < 200 \quad (39)$$

$$Nu_p = 2 + 0.5\epsilon^{3.5}Re_p^{1/2}Pr^{1/3} + 0.02\epsilon^{3.5}Re_p^{0.8}Pr^{1/3} \quad 200 < Re_p < 1500 \quad (40)$$

$$Nu_p = 2 + 0.000045\epsilon^{3.5}Re_p^{1.8} \quad 1500 < Re_p \quad (41)$$

where  $Re_p$  is defined as

$$Re_p = \frac{|\mathbf{u}_f - \mathbf{u}_p|D_p}{\nu_f} \quad (42)$$

and the exponents  $n$ ,  $a$ , and  $b$  are empirical constants usually derived on an ad-hoc basis. Here,  $\mathbf{u}_p$  is the particle velocity,  $\mathbf{u}_f$  is the fluid velocity inside the mesh cell that the particle occupies, and  $\nu_f$  is the fluid kinematic viscosity.

### 3.3 Coupling Paradigm

To achieve two-way coupling between the Finite Volume solver and the DEM solver, an open-source framework called CFDEM Coupling [51] was implemented in this study. It provides an open source parallel coupled CFD-DEM framework combining the strengths of the LIGGGHTS DEM code and the Open Source CFD package OpenFOAM. The CFDEM coupling toolbox allows for the expansion of the standard CFD solvers of OpenFOAM to include a coupling to the DEM code LIGGGHTS. The CFDEM Coupling library fundamentally takes care of the control and communication of information between LIGGGHTS and OpenFOAM. It also provides several models to calculate CFD fields using DEM scalars and vice-versa. Similar to LIGGGHTS, these models are also written in C++ and allow easy source code modification. To elaborate on all the models that are included in CFDEM Coupling would deviate from the main discussion of the manuscript. Hence, only the most important aspects are mentioned here. A typical CFD-DEM coupling implementation takes places in the order described in Figure 19.

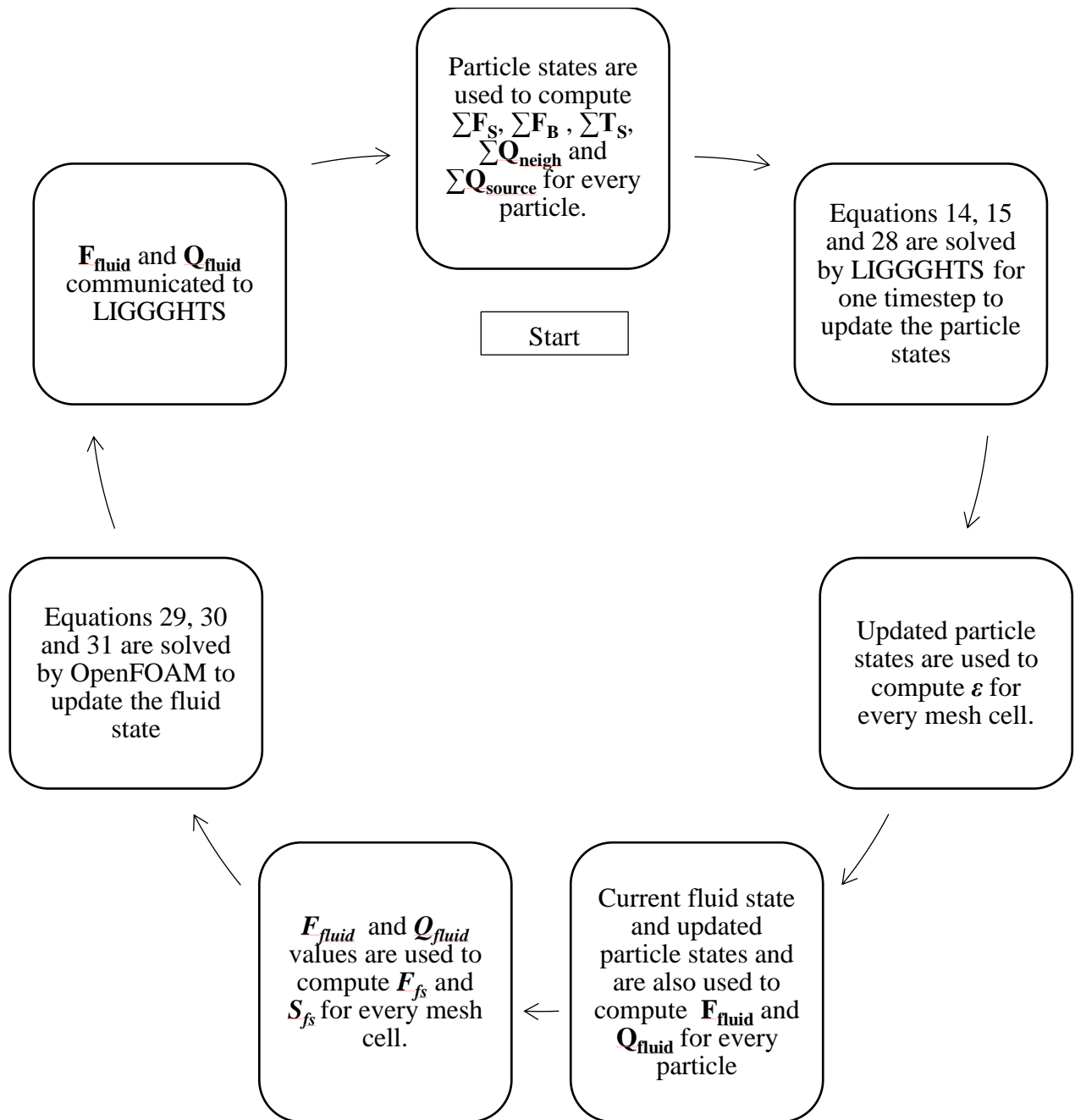


**Figure 19:** Steps involved in CFD-DEM coupling

Computing  $\epsilon$  for every mesh cell requires two models from CFDEM Coupling – 1. Locate Model that searches for the CFD cell a particle is present in, and 2. Void Fraction Model that lumps all the particle volume present in a CFD cell to calculate the void fraction. In the current study, the default search engine available in the CFDEM Coupling library is implemented. However, a

different void fraction model had to be used to get accurate results. This is because available the default models work better if the particles are relatively small compared to the CFD mesh cells. They fail if a particle spans across more than one CFD cell. Since the current study is focused on heat transfer of packed beds, the typical simulation domain is on the order of 5-15 times the particle radius diameter. As a result, when a fine mesh is used for better CFD accuracy, a single particle ends up occupying more than one CFD cell. To address this issue, a technique called the Divided Void Fraction model is used in the current study.

### 3.3.1 Void Fraction Model

In the Divided Void Fraction model, a particle of radius  $R$  and its volume is divided into 29 non-overlapping regions of equal volume. The centroids of these volumes are then used to reproduce each volume. The first volume is a sphere with the center coinciding with the particle center. Radius of this sub-sphere can be calculated as:

$$\frac{V(r_1)}{V(R)} = \frac{r_1^3}{R^3} = \frac{1}{29} \quad (43)$$

$$r_1 = R\sqrt[3]{1/29} \quad (44)$$

The remaining volume is a spherical layer that is divided into 2 layers of equal volume. The radial position of the border between these two spherical layers in radial direction can be easily calculated as:

$$\frac{V(r_2)}{V(R)} = \frac{r_2^3}{R^3} = \frac{15}{29} \quad (45)$$

$$r_2 = R\sqrt[3]{15/29} \quad (46)$$

Each of these spherical layers is then sub-divided in 14 elements of equal volume. The radial position of the centroid point of each sub-volume in the first spherical layer is as follows:

$$r_{s,1} = \frac{\int r dV}{\int dV} = \frac{3 r_2^4 - r_1^4}{4 r_2^3 - r_1^3} \approx 0.62761R \quad (47)$$

Similarly, for the second spherical layer remembering that the external radius is the particle radius:

$$r_{s,1} = \frac{\int r dV}{\int dV} = \frac{3 R^4 - r_2^4}{4 R^3 - r_2^3} \quad (48)$$

In this way instead of lumping the entire particle volume into one single CFD cell, each of the 29 sub-volumes of the particles are added to the CFD cells that contain their corresponding centroids. This improved the void fraction estimates and subsequently the CFD-DEM accuracy.

### 3.3.2 Smoothing Exchange Scalars

Even though the CFDEM Coupling framework distributes a particle's volume in all the CFD cells it occupies with the Divided Void Fraction mode, the coupling terms (Momentum Exchange Term and Energy Exchange Term) are still added in only one CFD cell. This was not a problem for the Energy Exchange term, as it is a scalar solved by a single equation. But the Momentum Exchange term resulted in very large residuals shooting up, ultimately affecting the solution stability. To address this, the exchange fields were artificially spread out by implementing smoothing algorithms. Unlike the distribution of particle volume, these scalars are spread out on the CFD cells by taking into effect the neighboring particles as well. To do that, a smoothing field was defined throughout the CFD domain with an initial value of 0. At each coupling instance, a smoothing field (SMF in equation 49) value of 1 is imposed on the cells that have a particle centroid within them. Then, using a Laplace Equation, the smoothing field is diffused across the CFD mesh, until each spike is diffused to a span of particle radius. The diffused smoothing field is then multiplied by the Exchange term's magnitude, which is then added to the CFD solver. In this way, instead of adding the entire exchange scalar into one CFD cell, it is distributed over

several CFD cell. This algorithm, when implemented, proved successful in controlling the discontinuities rising from the exchange terms.

$$\frac{\partial(SMF)}{\partial t} + \nabla^2 \cdot (SMF) = 0 \quad (49)$$

### 3.4 Preliminary Heat Transfer Studies

To evaluate the applicability of the above-mentioned models, a basic simulation setup was designed to find an estimate of the effective thermal conductivity (ETC or kEff) of a static bed of particles. The simulation setup is composed of a hollow cylinder filled with ceramic particles. The diameter of the cylinder is 0.001 m while the height is 0.005 m. Particles of is 300  $\mu\text{m}$  in diameter are filled inside the cylinder until they occupy  $\frac{1}{4}$  of the total cylinder height. Once these particles are settled at the bottom of the cylinder with zero kinetic energy, constant temperature boundary conditions of 1000K and 300K are applied to the bottom and top surfaces, respectively. The simulation setup is depicted in Figure 20. The CFD-DEM simulation is run until a steady state is reached for the entire system.

The CFD-DEM simulations were conducted using the following particle properties: thermal conductivity (2 W/m-K), thermal heat capacity (500 J/kg-K) and density (3820 kg/m<sup>3</sup>). These are the properties of the particles used in a previous experimental study where kEff values of the same configurations as shown in Figure 20 were calculated. This was done to facilitate the validation of the CFD-DEM simulations with actual experimental data. For ceramic particles, the Young's Modulus values are in the range of 75000 MPa. As mentioned in section 3.2, these values are artificially reduced to a mere 5 MPa to increase the simulation speed. Subsequently, the particle-particle contact areas are scaled down to accommodate for this change using an *area correction factor (ACF)* given in equations 50 and 51. This relation was based on the observations made in equation 36.

$$ACF \sim \left( \frac{Y_{eff}^{Reduced}}{Y_{eff}^{Original}} \right)^{1.5} \quad (50)$$

$$Corrected \ Contact \ Area = ACF * \ Calculated \ Contact \ Area \quad (51)$$

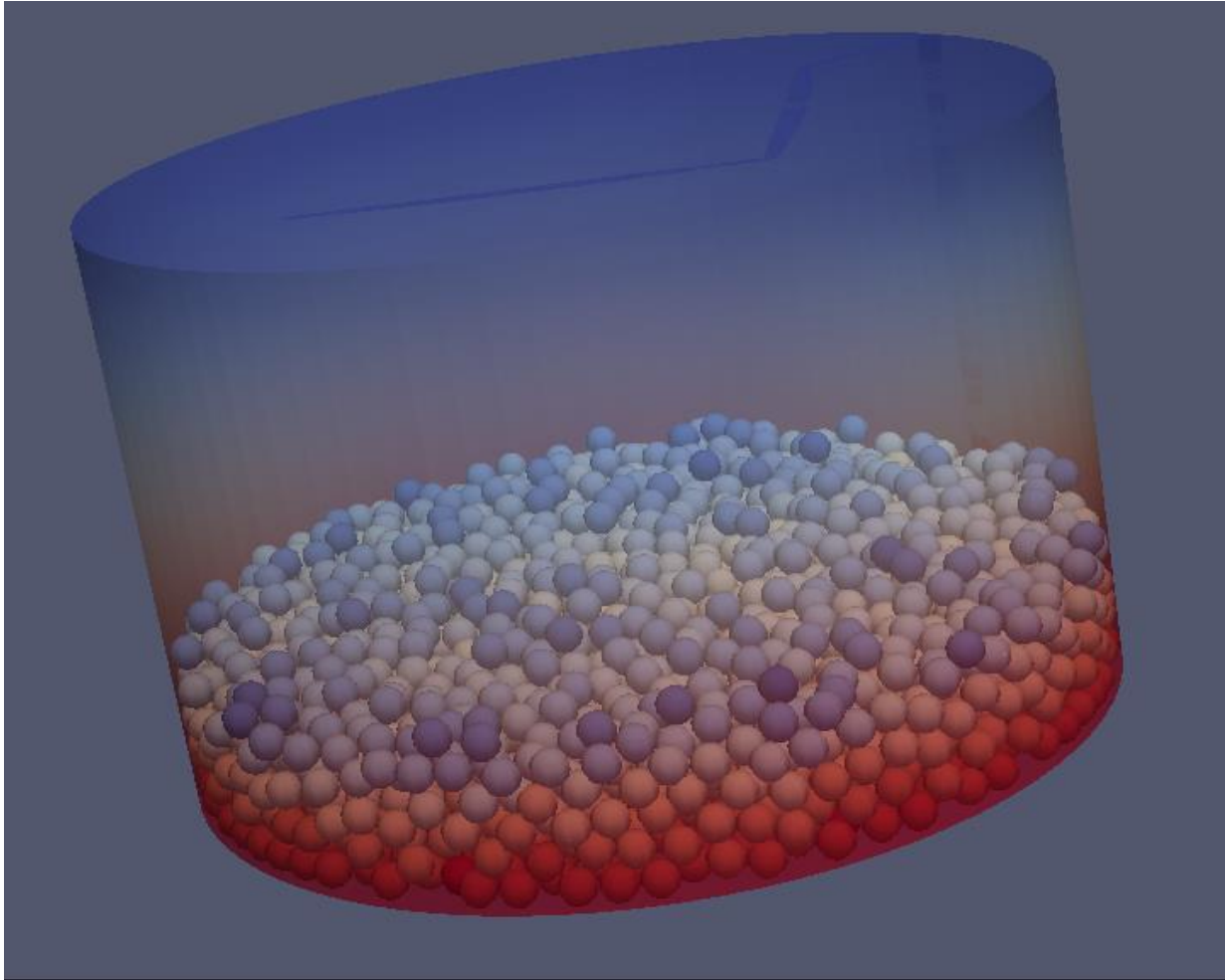


**Figure 20:** CFD-DEM simulation setup with 1000K temperature on the bottom wall and 300 K on the top wall

Since the cylinder walls are thermally insulated, there is no thermal gradient in the radial direction. As a result, only the axial temperature profile needs to be considered to characterize the heat transfer and is plotted in Figure 21. The temperature profiles were obtained both from the particles and the interstitial air. It can be observed that there is thermal equilibrium between them.

To verify this temperature profile, a one-dimensional heat transfer equation (HTE) was solved in Matlab using the experimentally determined values of  $k_{\text{Eff}}$ . The temperature profile of the 1D HTE is presented in Figure 22. It can be observed that the temperature gradient in the particle beds is steeper in CFD-DEM simulations compared to the 1D HTE solution. Since the axial heat flux is constant for this system, one can easily calculate the effective thermal conductivity of the particle bed by comparing the temperature gradients in both cases as

$$k_{\text{particleBed}} \left( \frac{\partial T}{\partial z} \right)_{\text{particleBed}} = k_{\text{air}} \left( \frac{\partial T}{\partial z} \right)_{\text{air}} \quad (52)$$

Using equation 52, it was observed that the CFD-DEM simulations suggested a very low value of  $k_{\text{Eff}}$ , 0.016 W/m-K, as opposed to the experimental value of 0.2 W/m-K. This verifies that the CFD-DEM was not able to accurately capture the heat transfer physics.

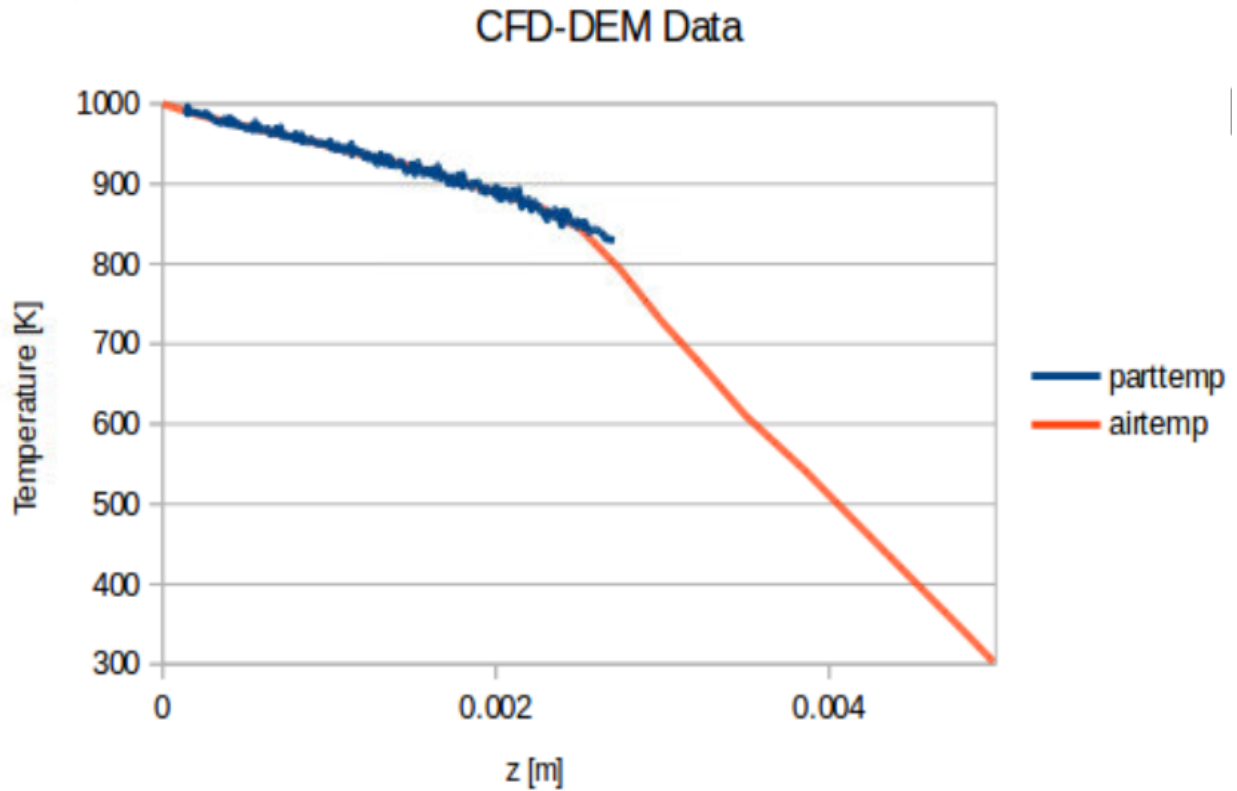


**Figure 21:** Temperature profiles of CFD-DEM solution after achieving steady state

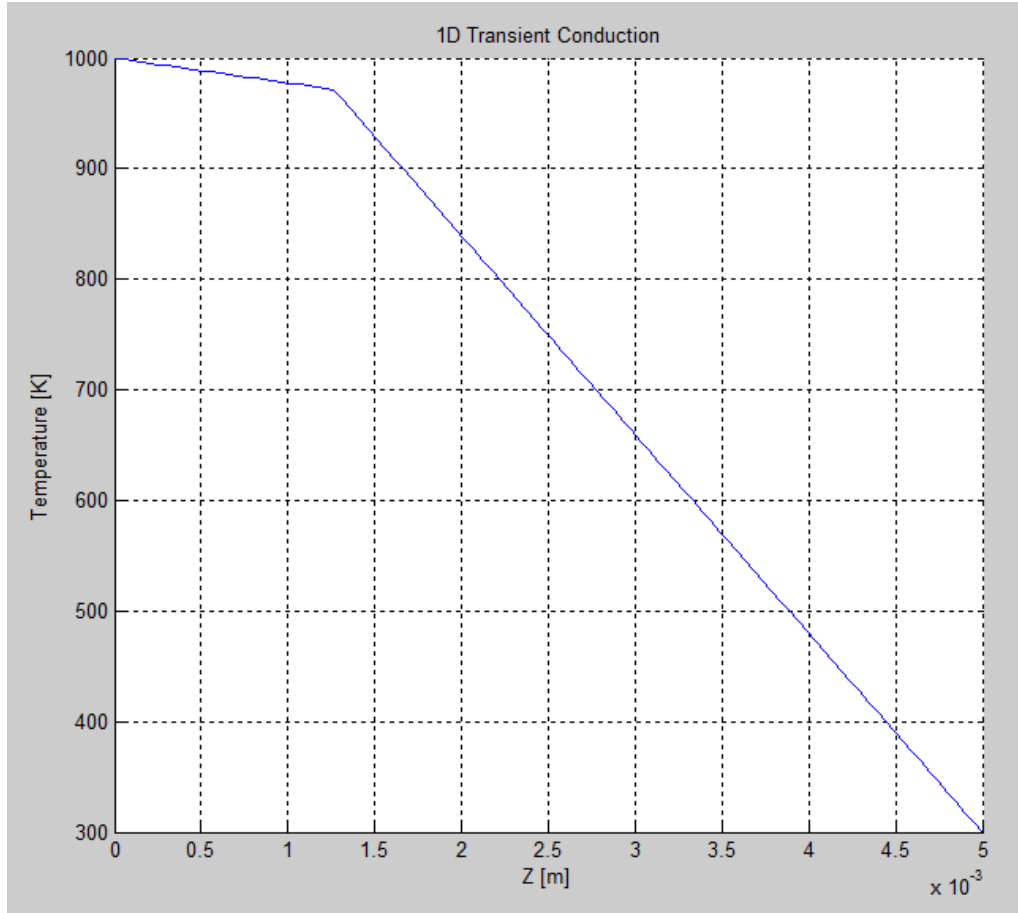


**Figure 22:** Temperature profiles of 1D Transient conduction equation in MATLAB after achieving steady state

It was initially hypothesized that the *area correction factor (ACF)* is reducing the particle-particle contact area to negligible magnitudes and is thus causing the poor thermal behavior in CFD-DEM simulation. Hence, the ACF was further tuned, ignoring the physics-based predictions from equation 51, to match the CFD-DEM results with experimental values. But tuning the ACF to increase the particle-particle contact area led to relatively higher particle-particle contact heat fluxes compared to the particle-air convective heat fluxes. This was contradicting the observations made from the theoretical model developed from the previous experimental works [46]. The

model, which was extensively validated, suggested that the contribution of particle-particle contact conduction is usually negligible for such high Young's Modulus particles. Hence, further investigation was conducted to see if manipulating the particle-particle contact area on an ad-hoc basis is physically accurate or not.

In one of the experiments conducted previously, the variation of effective thermal conductivity ( $k_{\text{Eff}}$ ) with pressure was analyzed. In general, with increasing pressure, particle-particle contact deformation increases due to higher contact load. This should improve particle-particle conduction and increase  $k_{\text{Eff}}$ . The percentage of increase is governed by how sensitive the overall thermal behavior is to the particle-particle conduction mode. Figure 23, which was plotted to track the  $k_{\text{Eff}}$  with different applied pressures, confirms that  $k_{\text{Eff}}$  increases with increasing pressure, but the percentage of increase is not large.

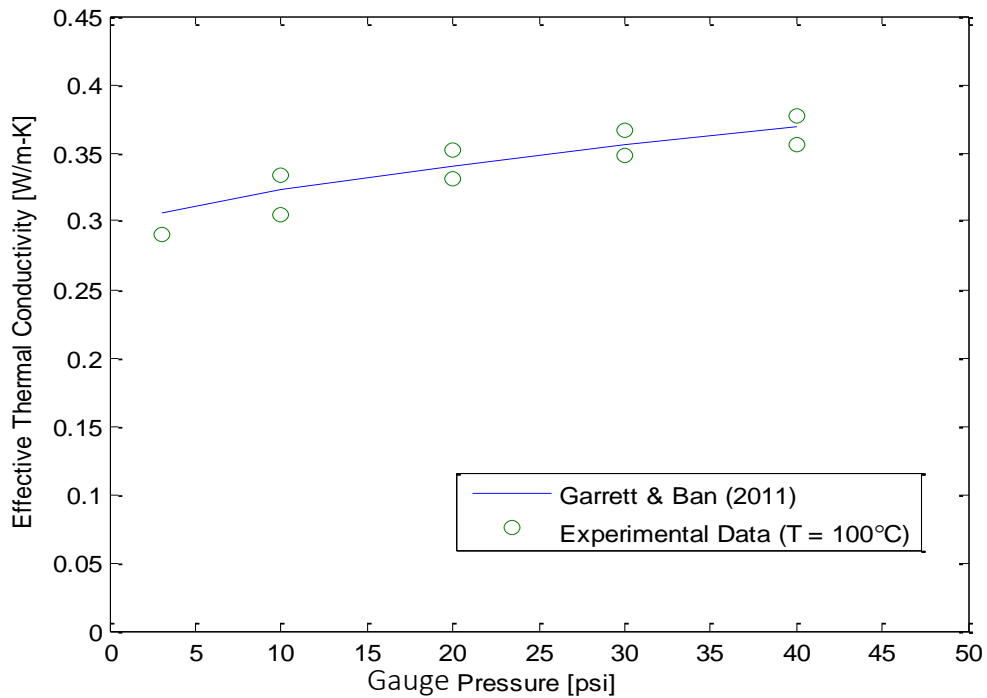


**Figure 23:** Variation of Effective Thermal Conductivity as seen in experiments [46]

Now, if the CFD-DEM framework with ACF tuning is accurate, it should also replicate a similar behavior and slope. Hence studies were conducted using CFD-DEM framework with ACF tuning and the results are plotted in Figure 24. Since the slope is very high compared to the one in Figure 23, it can be concluded that the sensitivity of  $k_{\text{Eff}}$  to pressure is very high in the current CFD-DEM framework. This clearly implies that the tuning of ACF to increase the particle-particle contact area and particle-particle conduction does not restore the physics of the problem.

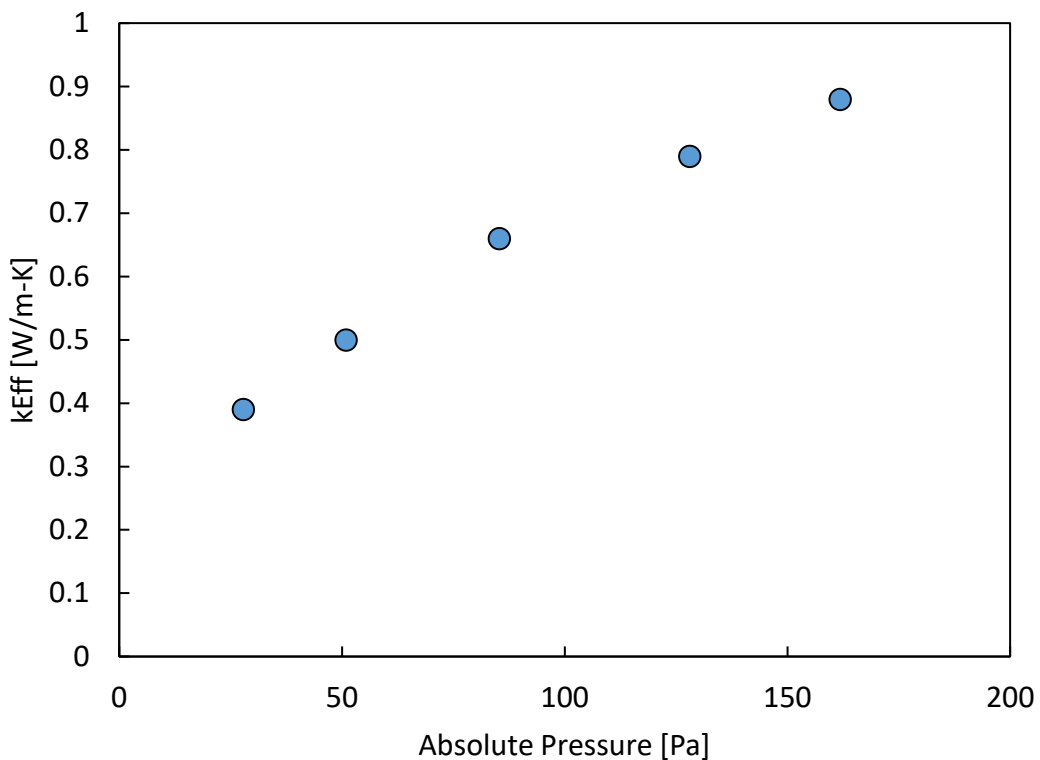


**Figure 24:** Variation of Effective Thermal Conductivity ( $k_{\text{Eff}}$ ) with Pressure as observed from CFD-DEM framework with ACF tuning

Thus, instead of tuning the ACF to artificially control the particle-particle contact area, other aspects of the CFD-DEM framework, namely – Lumped Capacitance, Particle-Particle

Conduction Model and Particle-Air Convection Model – need to be evaluated for making this method of two-way coupling applicable for heat transfer analyses in dense granular media.

## Chapter 4

# Particle-Resolved DNS

Most of the previous research that focused on understanding the heat transfer physics in packed beds used experimental data to validate their insights and models. Experimental runs were performed on packed beds to evaluate the effective thermal conductivities (ETC) and the proposed models were tuned to match these values. Although practically useful for global heat transfer calculations, they do not provide particle-scale insights into the heat transfer physics. It is important to incorporate these insights into closure models implemented in Discrete Particle Methods. If not, the multi-scale modelling techniques fail to capture the proper heat transfer as illustrated observed in the previous chapter. Additionally, experimental data also has restrictions on the configurations that can be tested and the parameters that can be varied. To circumvent these issues, the current work explores the use of Particle-Resolved Direct Numerical Simulations (PR-DNS) to observe the overall thermal performance and to understand the intricate heat transfer mechanisms in a packed bed. This method stands as a simple modification to the conventional DNS approach. It is relatively straightforward to implement and can provide high fidelity particle-scale insights. Hence, the current chapter provides a brief description of PR-DNS methodology and the heat transfer insights obtained from this approach. It is to be noted that all the observations

and discussions herein are limited to cases where no radiation heat transfer occurs and where the variation of thermal properties with temperature are not considered.

## **4.1 Simulation Methodology**

Among the different multi-scale modelling approaches [30], Discrete Particle Models (DPM) and Direct Numerical Simulations (DNS) are usually selected for high fidelity results. As mentioned in chapter 3, the advantage of Discrete Particle Models lies in accurately solving for the positions of individual particles in the computational domain by calculating the interaction forces between neighbouring particles and the surrounding fluid. Recently, researchers have added heat transfer models to this approach to solve for the thermal transport in particulate systems as well [52]. But since each particle is considered as a single lumped system in DPM, this approach can neither resolve intra-particulate thermal gradients nor non-uniform thermal fluxes on a particle surface. DNS stands as the most accurate method as it tracks all the solid-fluid interfaces to resolve every possible fluid-particle and particle-particle interaction (these methods include Immersed Boundary Methods, Lattice Boltzmann Methods, etc.). But such level of accuracy comes with a huge computational cost. As a result, the solution of any practical problem requires balancing the required accuracy with available computational resources.

To tackle the above-mentioned short-comings of these methods, both DNS and DPM can further be combined to form Particle-Resolved Direct Numerical Simulations (PR-DNS), leveraging the advantages of both. In this approach, the packing structure of the particles is first determined by a DPM solver. This information is then used to model a multi-phase computational domain composed of solid particles and fluid void-spaces. Finally, the heat transfer behaviour of this domain is calculated using a DNS solver. It is to be noted that this approach is different from a typical two-way coupled multi-phase simulation, where the simulation accuracy depends on the

closure models between the phases. The following sub-section details the implementation of PR-DNS for the current study.

In the current study, PR-DNS is implemented to gain insights into the detailed heat transfer characteristics of packed beds. The simulation domain, shown in Figure 25, is a cylindrical cell with a packed bed of particles at the bottom. This is very much the same as the domain considered in the previous chapter. Throughout this chapter, four particle radii ( $R_p$ ) were used with four different fluid thermal conductivities ( $k_f$ ) and 9 different solid-fluid thermal conductivity ratios ( $k_s/k_f$ ). The cylinder diameter in all the cases is roughly 10 particle diameters and the cylinder heights are adjusted such that a considerable amount of air column is present on the top of the settled particle bed.

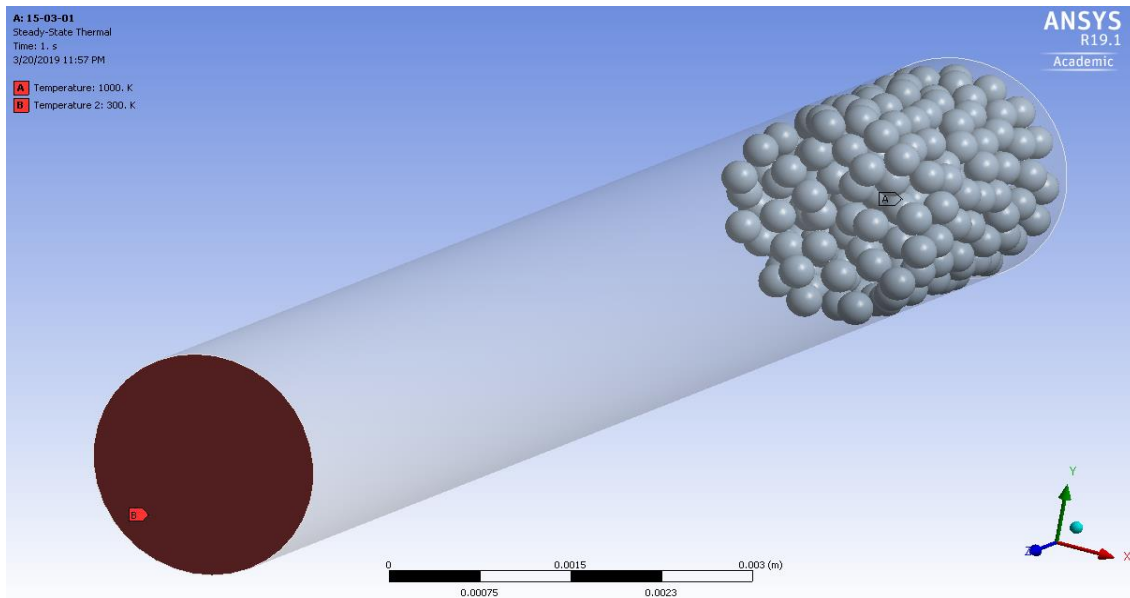


**Figure 25:** Simulation Domain (Gravity in negative Z-direction)

Initially, the particles are added into the cylinder at random locations and are allowed to settle under the action of gravity. The DPM aspect of PR-DNS is used to solve for the settling of particles (i.e. particle structure) at the bottom of the cylinder. Similar to the previous chapter, the

open-source DEM code LIGGGHTS [50] was used to solve for the motion of individual particles in a Lagrangian framework. Once the inserted particles are settled, their centroid locations are extracted from the DEM code. A Visual Basic macro was written to use this information to create a three-dimensional geometry of particle-bed and void-spaces in Dassault Systèmes SOLIDWORKS. The macro first creates a 3D sketch with points located at the locations of the particle centroids. Then a solid sphere is created using revolve tool. This solid sphere is then copied at all the generated 3D points using a sketch-driven pattern tool. These two steps are depicted in Figure 26 (a) and (b), respectively. Finally, a cylindrical enclosure is added to the particle assembly to generate the simulation domain as shown in Figure 25. The enclosing cylinder is generated such that its volume does not overlap with the already existing particles in the domain.

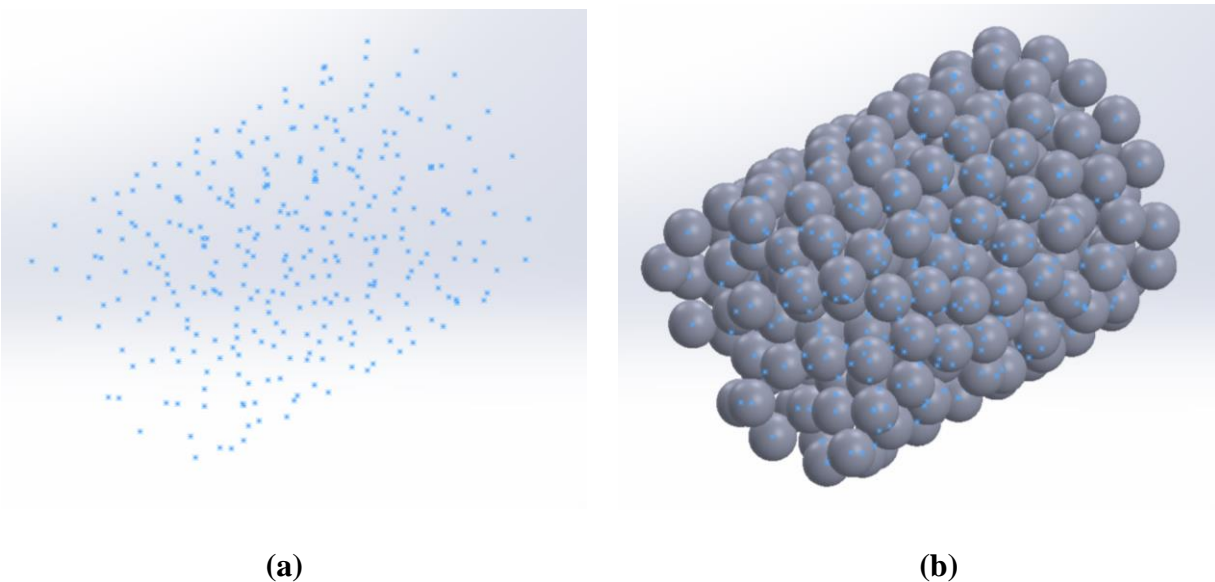


**Figure 26:** Generation of a Three-Dimensional particle cloud using a Visual Basic Macro in Solidworks. (a) 3D sketch with points at the particle centroid locations; (b) Sketch-driven pattern of solid particles at the particle centroid locations

The generated 3D geometry is further used to generate an unstructured mesh that is used for the DNS calculation. Figure 27 depicts a section of the three-dimensional mesh used for the

DNS calculation. The mesh has two separate zones, one for the particles (shaded in blue) and the other for the void-spaces (shaded in grey). The meshing was done such that any mesh cell on the particle surface can be no larger than  $1/25^{\text{th}}$  of the overall particle surface area. Owing to the dense nature of the particle packing considered here, the geometry resulted in sharp corners and thin wedges at particle-particle and particle-wall contact points. As a result, the mesh cells in these regions are highly skewed and are of poor quality. When a Finite Volume solver was used on such a mesh, the calculations led to convergence problems and inaccurate results. On the other hand, Finite Element solvers showed faster solution convergence and better accuracy. Thus, the commercial Finite Element package (ANSYS APDL) was used as the DNS solver to evaluate the heat transfer behaviour in the current study.

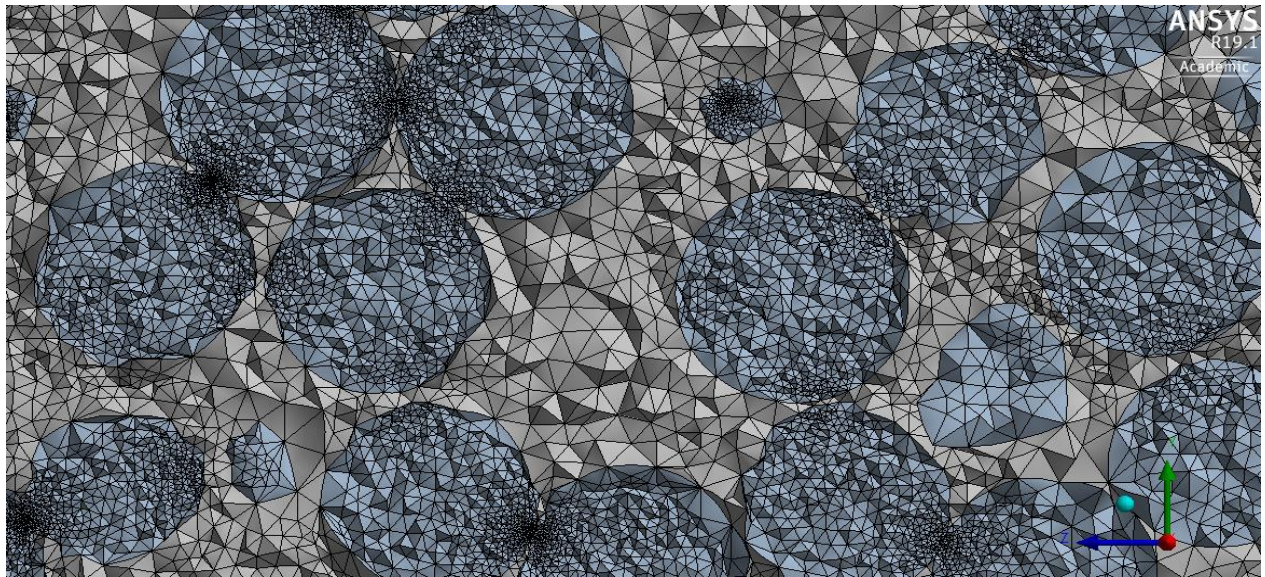


**Figure 27:** Three-dimensional mesh used for DNS (Blue mesh cells represent particles while grey mesh cells represent the interstitial air)

The Finite Element code was run until the system reached steady state and the temperature distributions of the entire system were computed. This information was then used to calculate the

effective thermal conductivity (ETC or  $k_{eff}$ ) of the system. Though the ETC results are not presented in the current chapter, they are described later and in chapter 5. To ensure that the heat transfer observations made are not limited to a specific single particle arrangement, three different random packed bed configurations were evaluated for every simulation case. In addition to the temperature profiles and ETC, the heat flux vectors on every particle surface were also calculated. A mesh convergence study was also conducted tracking the calculated ETC values with different mesh resolutions. It was observed that with increasing number of mesh cells, the ETC values asymptotically merge to a single value suggesting that the obtained solution is grid independent. The required mesh resolution to obtain such solution varied among the different cases tested in the current study. The following sub-section briefly describes all the important observations that can be drawn from a PR-DNS implementation on a packed bed, where grid-independence was reached.

As boundary conditions for the DNS solver, the top wall of the cylinder is maintained at 300 K and the bottom wall is maintained at 1000 K (highlighted in Figure 25). Though the boundary temperature is high, as mentioned above, effects of radiation heat transfer and the variation of properties with temperature are not considered in this study. An insulated boundary condition is imposed on the cylindrical wall. Typically, all the PR-DNS studies conducted in the current study had 2 million tetrahedral mesh cells. It roughly took 10 minutes to obtain the particle packing in DEM simulation, 10 minutes to run the macro and tune the 3D geometry, and 30 minutes to run the DNS solver.

The series of steps usually involved in a PR-DNS setup can be summarized as follows in Figure 28. These results, since do not involve any modelling assumptions, can be used as benchmark data for developing models and to gain important theoretical insights into the heat transfer physics of densely packed particle assemblies.

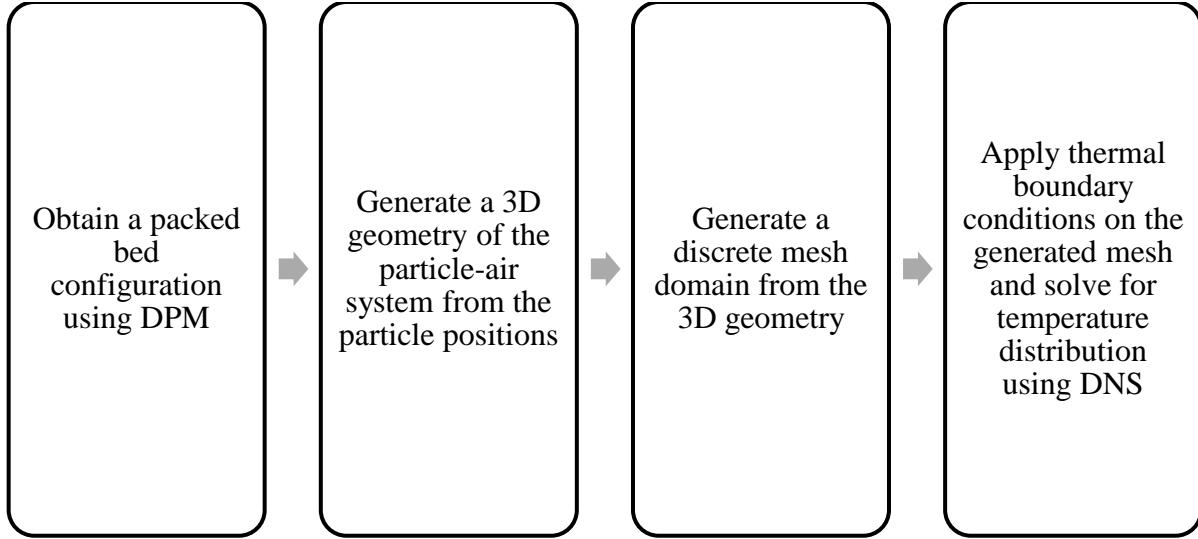
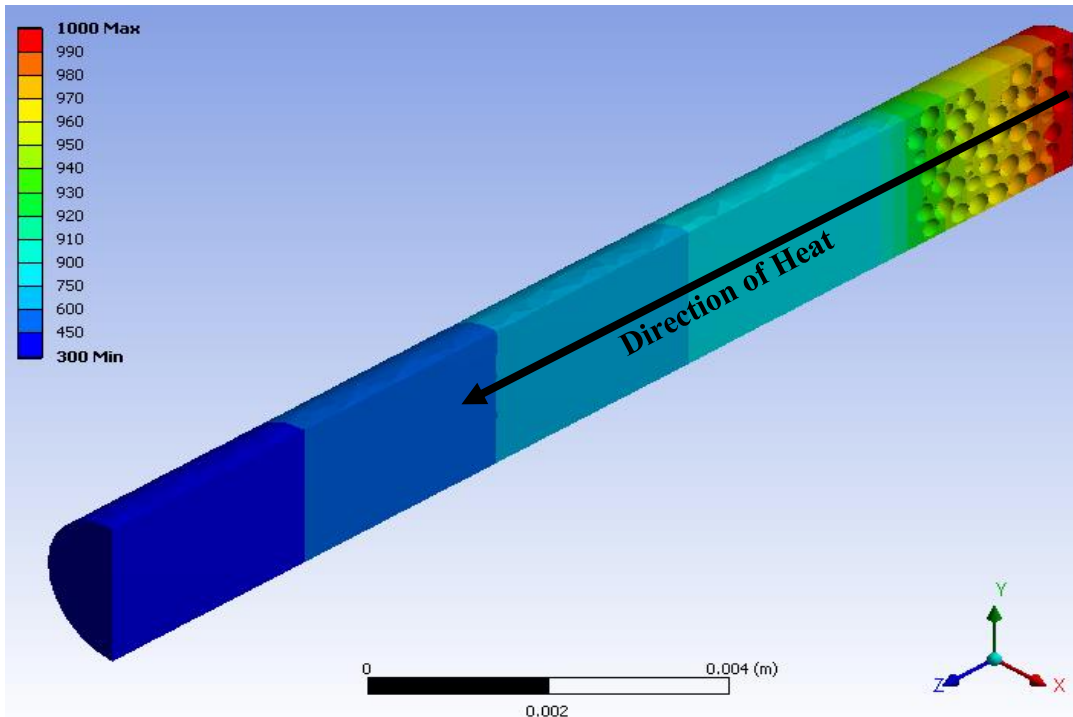


**Figure 28:** PR-DNS Implementation

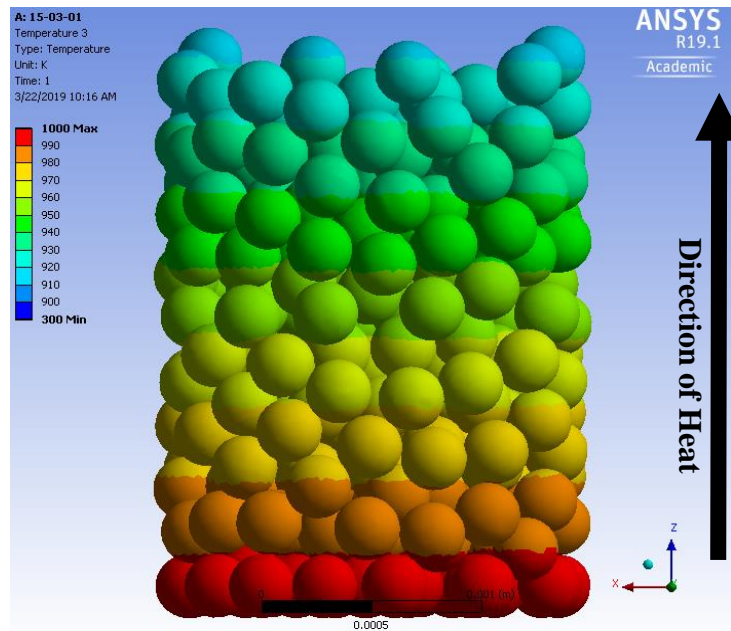
## 4.2 Heat Transfer Studies of a Randomly Arranged Particle Bed

The steady state solution of a PR-DNS simulation for a packed bed of 300 particles, each of 300-micron diameter, in a 0.001 m radius cylinder with 0.015 m height is depicted in Figure 29. For this simulation, the fluid was air with thermal conductivity ( $k_f$ ) of 0.02534 W/m-K and a low solid-fluid thermal conductivity ratio ( $k_{Particle}/k_{Air}$ ) of 2.5 was chosen. It can be observed that heat is being transferred from the bottom surface to the top surface. Owing to the insulated boundary condition on the cylindrical wall, all the isotherms are parallel to the gas-particle interface. The axial temperature profile for this case is plotted in Figure 30. It can be observed that a uniform temperature gradient occurs, both in the air domain and in the particle bed domain. Using these gradients, the ETC values of the packed bed can be obtained from the thermal conductivity of air,  $k_f$ , as follows:

$$ETC = k_{Eff} = \left( k \frac{\partial T}{\partial z} \right)_{fluid} / \left( \frac{\partial T}{\partial z} \right)_{bed} \quad (53)$$



(a)



(b)

**Figure 29:** PR-DNS solution of a packed bed. Temperature distribution inside (a) Interstitial Fluid (Air) and (b) Particle.

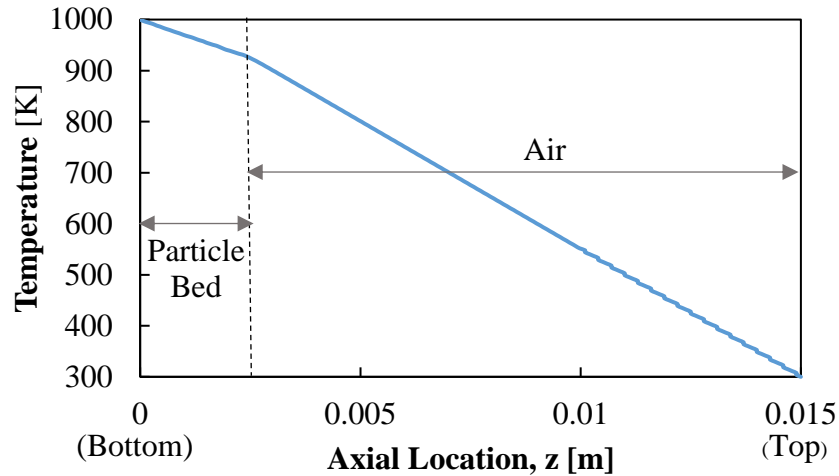


**Figure 30:** Axial temperature profile inside the packed bed and the air column

To observe how the heat is distributed on the surface a particle, heat flux vectors are plotted as shown in Figure 31. For illustration purposes, a particle is chosen such that it has three neighbouring particles on one half of its surface, while being in contact with only one of them. It can be observed that the heat exchange with neighbouring particles is more dominant than with the surrounding air (shown by long heat flux vectors on particle surface areas close to the neighbouring particles). It is obvious that the particle-air heat exchange is via convection and that the particle-particle heat exchange, when in contact, is due to thermal diffusion. But Figure 31 also suggests that the particles are exchanging heat with neighbouring particles, even when there is no contact between them. Though these particle surface zones are technically exchanging heat with air, this air column is just acting as a carrier between the particles to “stream” the heat energy. This phenomenon – which will be referred to as streaming heat transfer – is different from the typical convective heat transfer. Hence, this phenomenon cannot be captured with the convection models available in the literature. Thus we conclude that, when neglecting radiation heat transfer, a particle inside packed bed has three modes of heat transfer – 1. Conduction heat transfer with neighbouring particles in contact, 2. Convection heat transfer with the air surrounding the particles, and 3.

Streaming heat transfer to the neighbouring particles (via interstitial air) that may be in contact or not in contact. Although the above observations were drawn from this one particular case, all the other scenarios, with different particle diameters, solid-fluid thermal conductivity ratios, etc. also resulted in similar characteristics.

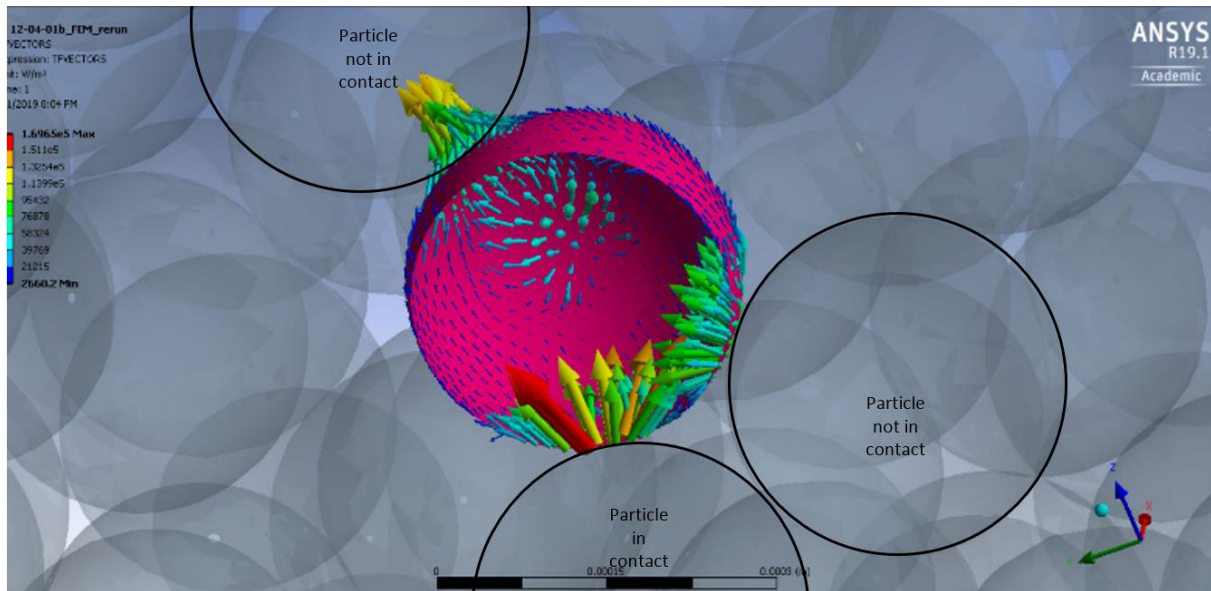


**Figure 31:** Heat flux distribution on the surface of a particle (Only one hemisphere depicted in the image)

Over the years several researchers have worked in quantifying the first two modes of heat transfer. They developed models that have been applied in a DEM implementation to solve heat transfer problems in particulate flows [51]. Since many particulate heat transfer problems focussed on fluidized beds which have low particle packing fraction, the influence of streaming heat transfer was minimal. However, for static beds, particularly those with high particle packing fraction, this phenomenon cannot be ignored. More studies are conducted in the following sections to confirm this behaviour and gain necessary insights that would help in developing a closure model to capture this phenomenon.

### 4.3 Heat Transfer Studies on a Single Stack of Particles

Before certainly confirming that the discrepancies observed in the CFD-DEM implementation in chapter 3 was solely due to the lack of a streaming heat model, all the different assumptions made in them were also evaluated. Hence, a series of PR-DNS tests were conducted to investigate the following aspects:

1. Lumped Capacitance assumption
2. Particle-Particle Conduction Model
3. Particle-Air Convection Model

For simplicity, a single-stack of 10 particles, perfectly aligned on top of each other in a cuboidal domain are considered for these studies. This is depicted in Figure 32. Like the previous section, the particles are first allowed to settle on top of each other under the action of gravity in DEM. Their centroids are then used to create a 3D geometry and mesh for the DNS solver. The results obtained from the DNS studies were compared with the CFD-DEM implementation to analyze the above-mentioned aspects. All the properties were same as in the previous section

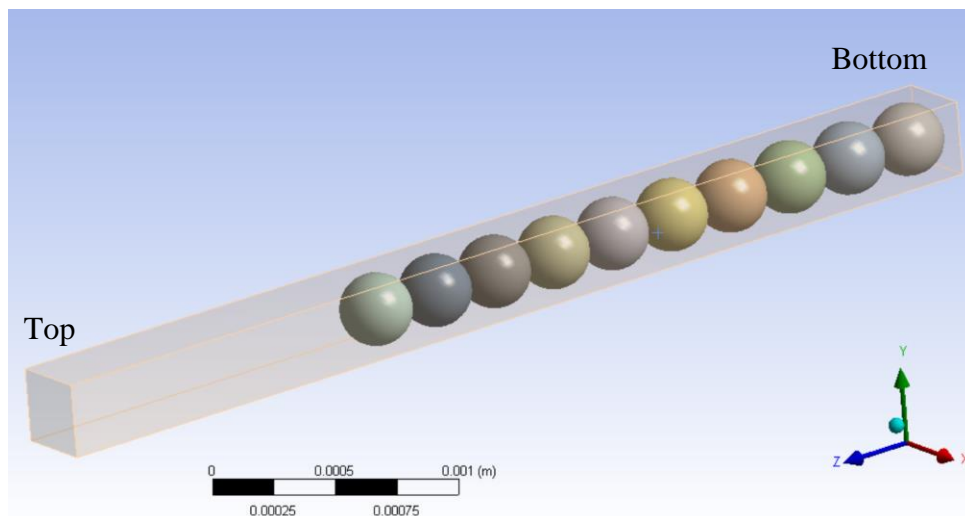


**Figure 32:** PR-DNS Simulation configuration to evaluate the assumptions made in CFD-DEM

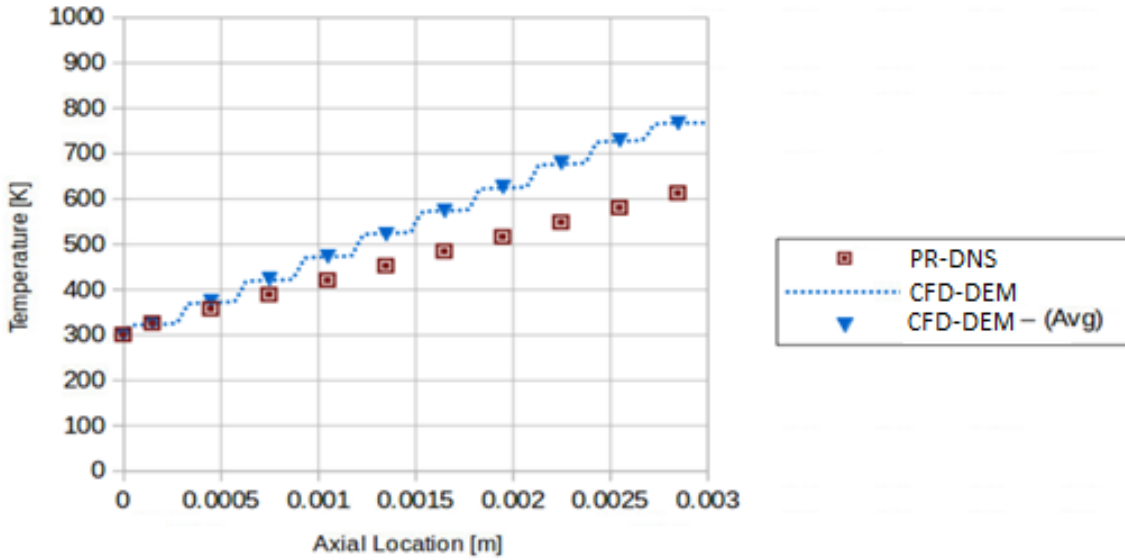
(Gravity in negative z-direction)

### 4.3.1 Verification of Lumped Capacitance Assumption and Conduction Model

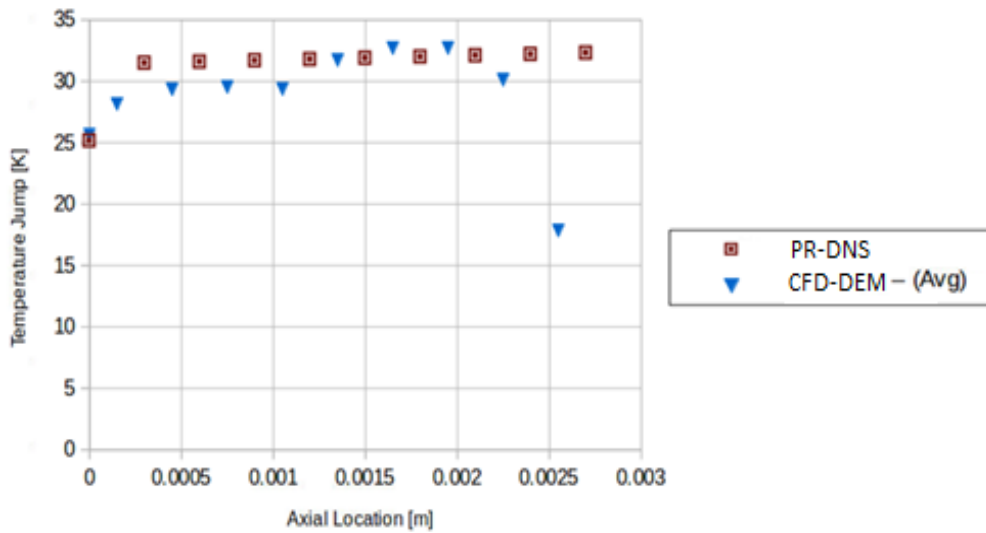
To isolate the influence of particle-air convection model, a series of PR-DNS and CFD-DEM simulations were conducted with no air around the particles. The particles are placed on a flat surface (z-axis) which is maintained at a constant temperature of 300K. Since there is no air, a thermal boundary condition applied on the top can not propagate the heat to the particles. Hence, a constant heat source of 0.001 W was added to the topmost particle. In this way, the 10-particle system experiences a constant heat rate on one end and constant temperature on the other end.

Figure 33 (a) depicts the temperature profiles while 33 (b) shows the temperature jump at the contact interface between two adjacent particles. Since a lumped capacitance model is assumed in the CFD-DEM solver, the temperature jump at the contact interface was simply calculated by finding the temperature difference of adjacent particles. On the other hand, the temperature jump in PR-DNS solution was calculated by first finding the temperatures of each particle at the contact interface junction and finding their difference. It can be observed that the PR-DNS and CFD-DEM solutions have similar trends but different magnitudes. On the other hand, the temperature jump at contact interfaces is the same in both cases. This essentially conveys that the difference in the temperature profiles of CFD-DEM and PR-DNS cases arises from the intra-particulate temperature gradient alone, and not because of any lapse in the particle-particle contact conduction model governed by equation 33 in chapter 2. To validate this, more simulations were conducted with a high particle thermal conductivity, so that the intra-particulate thermal gradient is less. The results of these simulations are plotted in Figure 34. As expected, with increasing particle thermal conductivity, the CFD-DEM solution became more closer to the PR-DNS results. Hence, it can be concluded that the discrepancy between CFD-DEM and PR-DNS solutions of single-stacked particles is arises from the lumped capacitance assumption alone. This in turn conveys that the

particle-particle conduction model assumed in the CFD-DEM framework is working well and there is no need to correct it.



(a)



(b)

**Figure 33:** Comparison of CFD-DEM and PR-DNS solutions for single stacked particle. a)

Temperature Profile; b) Temperature Jump at contact interface

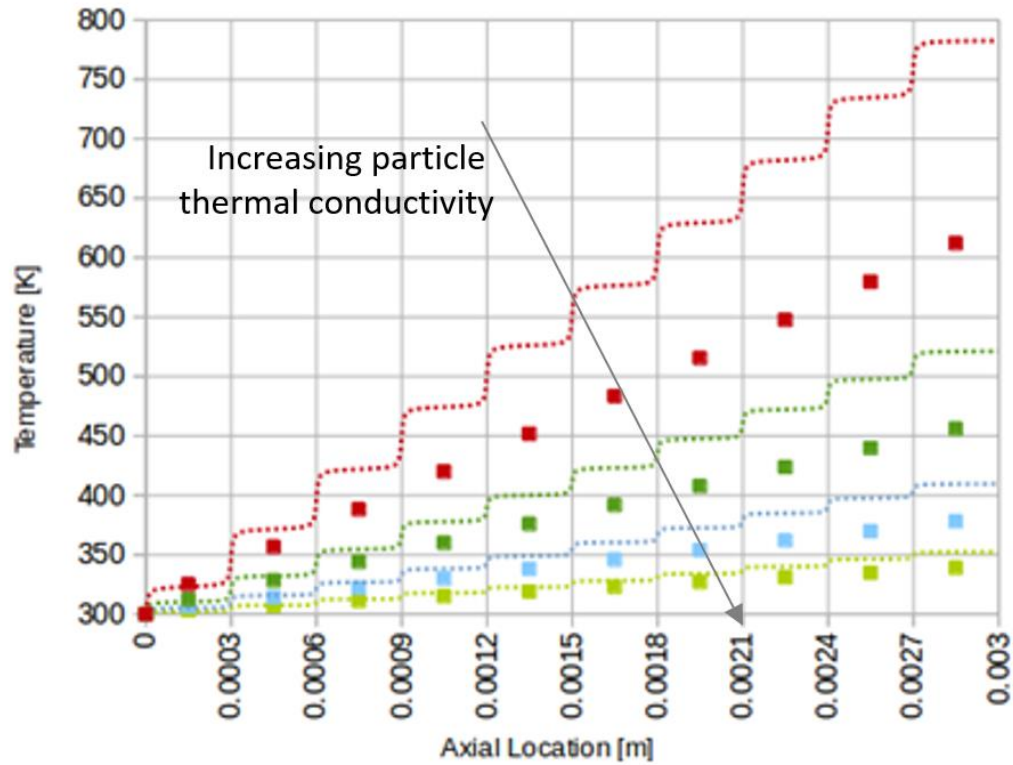


**Figure 34:** Behavior of CFD-DEM and PR-DNS solutions for single-stacked particles with increasing particle thermal conductivity

In Figure 35, the temperature profile inside a particle is plotted for the current case. It can be observed that the temperature inside the particle is not linear. This is because the area normal to the heat flow changes. As a result, the iso-magnitude contours of the temperature profile are curved. The reason for observing such high magnitudes of intra-particulate temperature gradients can be attributed to the unidirectional nature of heat transfer in the current setup (Heat flows only in vertical direction). But in a packed bed, since a single particle is surrounded by neighboring particles and interstitial air, there is chance of more temperature uniformity. Hence, though the lumped capacitance assumption might not be valid in all cases, it might still be a reasonable assumption when solving a packed bed of particles.

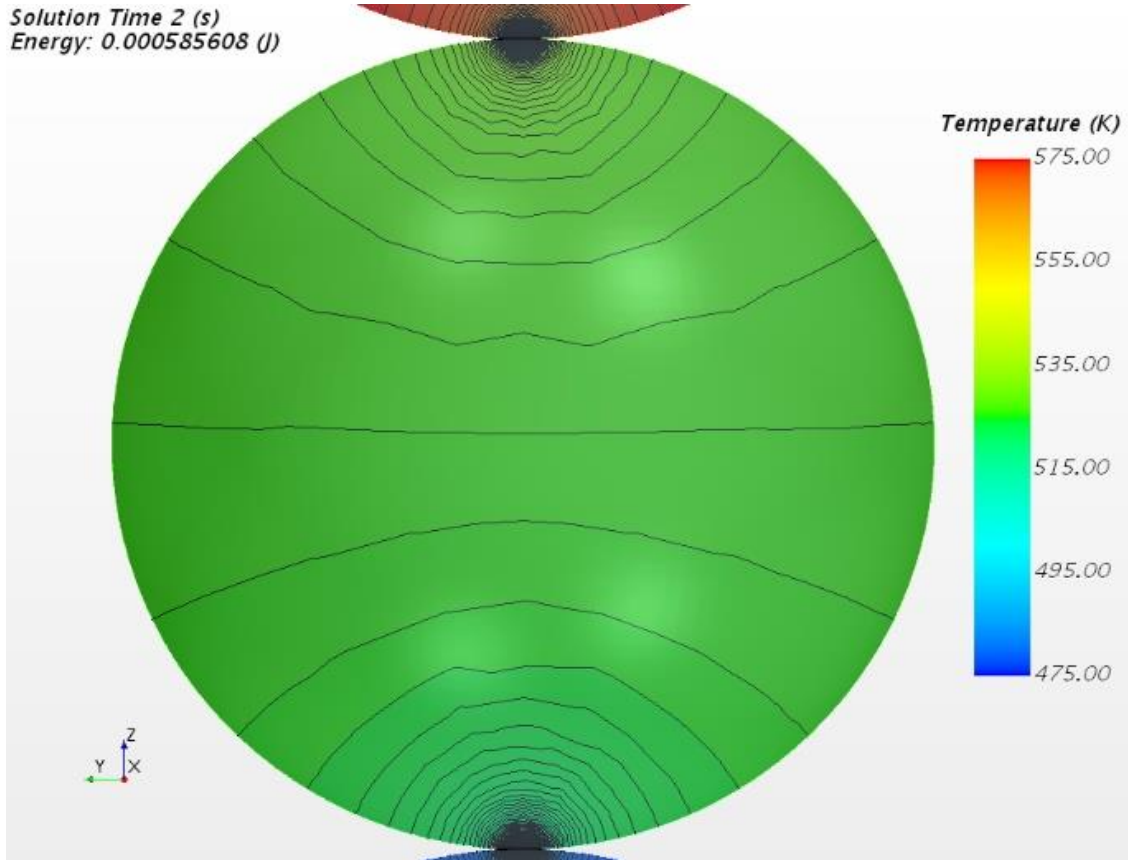


**Figure 35:** Intra-particulate temperature profile for single-stacked particles

Since there is no interstitial air, and lumped capacitance and particle-particle conduction models were found to be valid assumptions, the effective conductivity of the single-stacked particles can be estimated with

$$k_{eff} \frac{\partial T}{\partial z} \left( \frac{\pi D_{particle}^2}{4} \right) = Q_{contactConduction} \quad (46)$$

The term  $Q_{contactConduction}$  can be written from the conduction model in equation 33 as

$$k_{eff} \frac{\partial T}{\partial z} \left( \frac{\pi D_{particle}^2}{4} \right) = 4 \frac{k_{S,A} k_{S,B}}{k_{S,A} + k_{S,B}} \sqrt{A_{contact}} (T_A - T_B) \quad (47)$$

With  $k_{S,A} = k_{S,B} = k_s$ , this can be reduced as

$$k_{eff} \frac{(T_A - T_B)}{D_{particle}} \left( \frac{\pi D_{particle}^2}{4} \right) = 8 k_s R_{Con,AB} (T_A - T_B) \quad (48)$$

$$k_{eff} = \frac{8k_s\sqrt{A_{contact}}}{D_{particle}} \quad (49)$$

Since particle-particle conduction is the only mechanism in the current scenario, the above relation can be understood as the contribution of the particle-particle conduction mechanism to the overall effective thermal conductivity (kEff). Non-dimensionalizing the above relation with  $\sqrt{A_{contact}}$  as the contact length scale and  $D_{particle}$  as the particle length scale, we can understand that the contribution of particle-particle conduction to the overall values of kEff is just a function of the ratio of contact length scales to particle size scales as

$$k_{eff}^{contact\ conduction} \sim k_{particle} \left( \frac{Contact\ Length\ Scale}{Particle\ Length\ Scale} \right) \quad (50)$$

Since the contact length scales are always small compared to the particle length scales, the above relation solidifies the fact that the contribution of particle-particle conduction to the overall magnitude of kEff is always small. This was also hypothesized in another model developed previous using experimental evidences [46].

### 4.3.2 Verification of Convection Model

Since equation 50 suggests that the particle-particle contact conduction has very little influence on the overall heat transfer, it is natural to think that particle-air convection is solely the controlling heat transfer mechanism. To verify the superior contribution of convection over conduction, a new PR-DNS simulation with a single-stack of particles was done, this time with interstitial air present. It was observed that the value of kEff with interstitial air, became 5 times higher than the value measured with no interstitial air (Note shallower temperature gradient with air). As a result, it can be concluded that the interstitial air is the major contributed in the heat transfer physics of a

particle bed. This led to believe that the CFD-DEM implementation discussed in chapter 3 can be corrected by manipulating particle-air convection model.

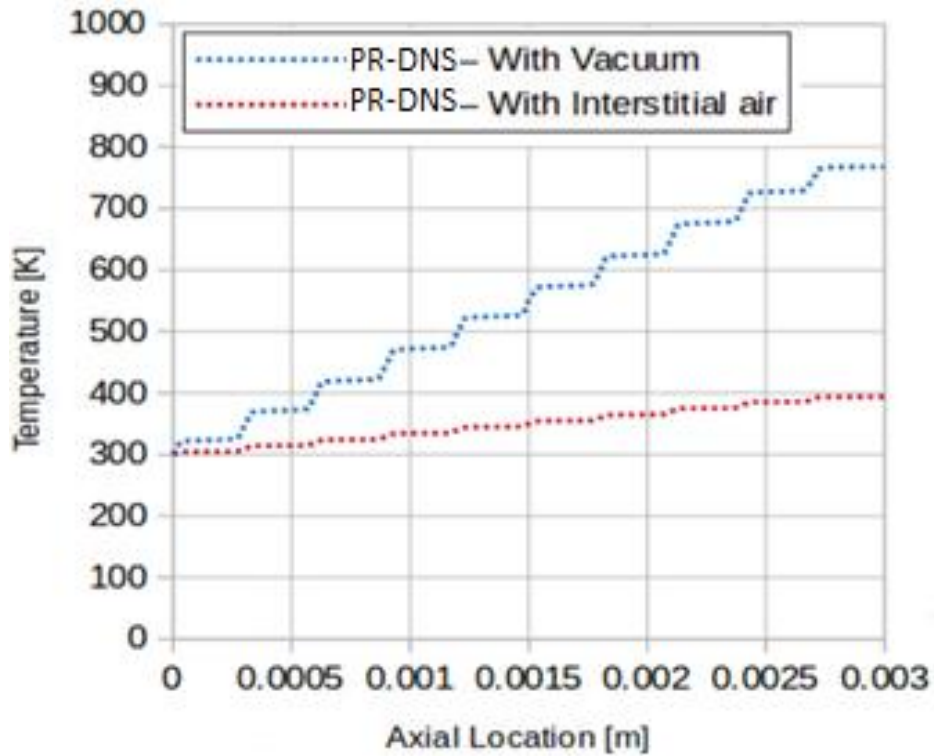


**Figure 36:** Comparison of temperature profiles with vacuum and interstitial air

Taking the above observations into account, CFD-DEM simulations were conducted to observe the effect of artificially increasing the particle-air convection rate. The simulation domain shown in Figure 20 was simulated using the CFD-DEM framework, but by hard imposing higher values of particle-air Nusselt number. The temperature profiles of these CFD-DEM simulations are plotted in Figure 37. In chapter 3, the CFD-DEM results were compared with experimental predictions. But for convenience, these results are now compared with PR-DNS simulations of the same cases. Four cases were tested, one using the original Nusselt Number relations (Equations 39 – 41) and three with  $Nu = 4, 8$  and  $18$ . Surprisingly, the CFD-DEM simulations didn't show any improvement in the thermal behavior with increasing Nusselt number. All the CFD-DEM

temperature profiles remained the same and consistently underestimated the thermal behavior of packed beds when compared to PR-DNS studies.

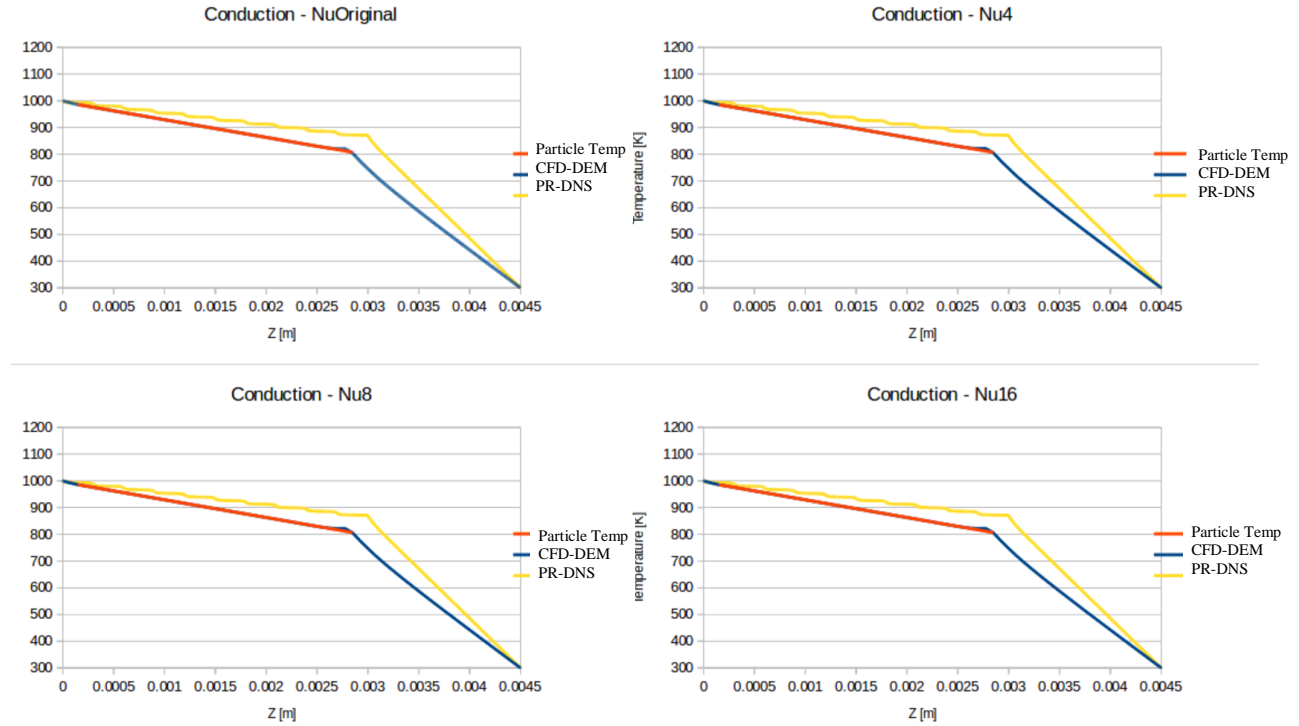


**Figure 37:** Variation of the CFD-DEM behavior for different Nusselt numbers.

So, it can be understood that, though convection is a strong contributor in the overall thermal behavior of packed beds, modifying equations 39-41 cannot correct the inaccuracies of the CFD-DEM framework mentioned in chapter 3.

### 4.3.3 Characteristics of Streaming Heat Transfer

Since the lumped capacitance assumption was considered a valid consideration, and the conduction and convection models in equations 33 and 39-41 were proven to be decently accurate in the previous sections, the only lapse in the CFD-DEM framework is the lack of a streaming heat transfer model. Hence, the current section explores this phenomenon with the help of PR-DNS simulations conducted on the single stack of particles described in Figure 32. Streaming heat

transfer has been studied sporadically in the past [35], [52]. To illustrate streaming heat transfer in a simple way, the heat flux vectors on a mid-plane are plotted in Figure 39. The solid white lines indicate the particle surface and horizontal dashed line indicates the centre line of the simulation domain. The flux vectors, which resemble thermal lines, can be seen starting from the surface of one particle and ending on the surface of the other. This demonstrates the previously made observation that the air trapped between two particles acts as a carrier to “stream” heat from one surface to another. The portion of the particle surface from which these flux lines originate is indicated with solid red colour in Figure 39. These red lines roughly mark the surface area of a particle where most of the streaming heat transfer is taking place. The dashed lines, originating from the centres of these particles to the edges of the red line mark the sectors inside the particles that undergo streaming heat transfer. Though the temperature profiles are not shown here, one can easily understand that the isotherms would be perpendicular to the heat flux vectors.

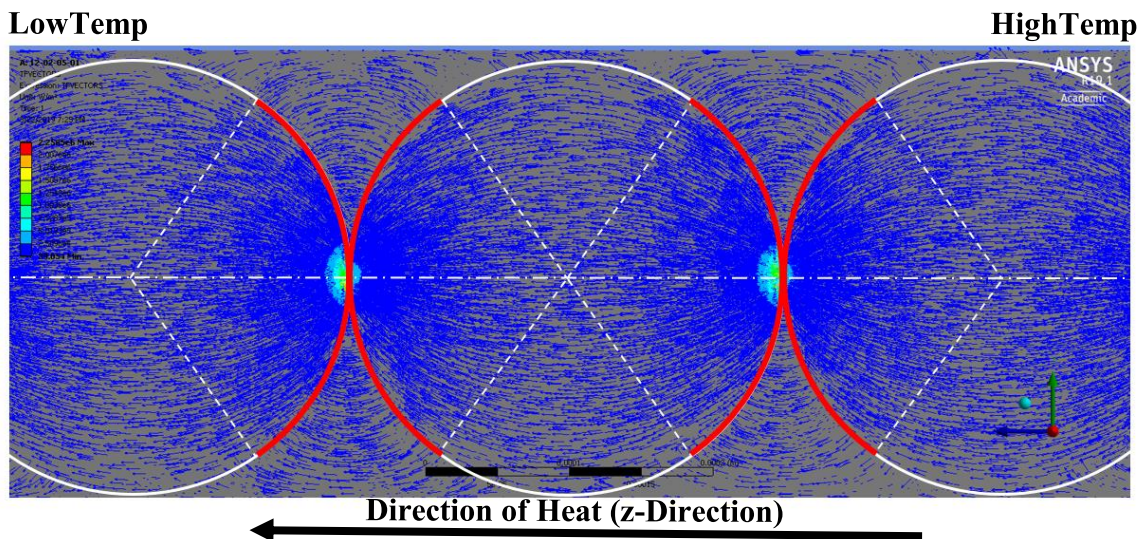


**Figure 38:** Heat flux vectors highlighting the presence of streaming heat transfer

To compare the values of streaming heat transfer and conduction heat transfer, an area-integration operation was performed on the heat flux vectors to calculate the net heat on every surface mesh cell of a particle. These magnitudes are lumped based on their position on the particle

surface and a bar chart is plotted showing this in Figure 40. The red coloured bars indicate the heat exchanged between air and the particle surface, while the blue bars at the ends indicate the heat exchanged with neighbouring particles via contact conduction. Negative magnitudes on the top hemisphere of the particle (right-side in the plot) imply heat leaving and positive magnitudes on the bottom hemisphere of the particles (left-side in the plot) imply heat entering. It can be observed that the amount of heat exchanged with a neighbouring particle at the contact area is significantly less than the amount of heat exchanged with the air. This leads to the conclusion that particle-particle streaming heat transfer is more dominant than the contact conduction. It is acknowledged that the magnitudes of heat transfer obtained from the PR-DNS simulation of a single inline particle stack might not exactly reflect the magnitudes in packed beds. Yet, the basic physical characteristics observed regarding streaming heat transfer still holds true. Using these preliminary observations, a closure model is developed to capture this phenomena in the next chapter.

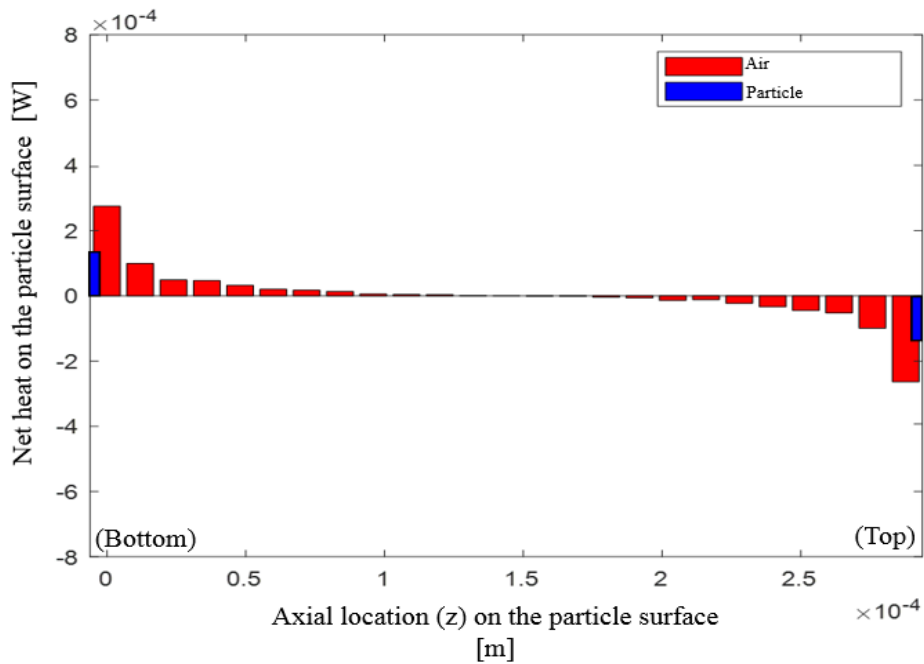


**Figure 39:** Distribution of heat on a particle surface

## Chapter 5

# Streaming Heat Transfer Model

Cheng et al.[9], developed two theoretical models by assuming that the streaming heat transfer between two particles is solely dependent on the area of the Voronoi cell surface between them. Both the models assumed that the heat exchange between two particles is isolated and takes places between the sectors of the particles which face each other. One model assumes a constant temperature boundary condition on the edges of the sectors, while the other assumes an isothermal core at the centres of each particle. Though these two models, when applied in a standard DEM implementation, showed improved accuracy in predicting the thermal behaviours of packed beds, their accuracy suffers for larger particles and for smaller solid-fluid thermal conductivity ratios. This is primarily because the influence of intra-particulate thermal gradient is not accurately characterized in these models. To address these issues, the current work focuses on developing a new model based on the previous ones [35] and tune it to make it applicable for a wide range of particle sizes and solid-fluid thermal conductivity ratios.

### 5.1 Model Development

For the development of the model we took the insights obtained in the previous section. In Figure 39, we observed that the streaming heat interaction occurs between the portions of the

particle surfaces marked by the solid red line. Figure 39 also highlights a thermal gradient inside the quadrants marked by the dashed white lines. This suggests that the heat transfer path between two particles includes three separate zones – 1. Particle A, 2. Interstitial Air, and 3. Particle B. These three zones can be modelled as three separate thermal resistances arranged in series. With this in mind, the streaming heat transfer is simplified as shown in Figure 41.

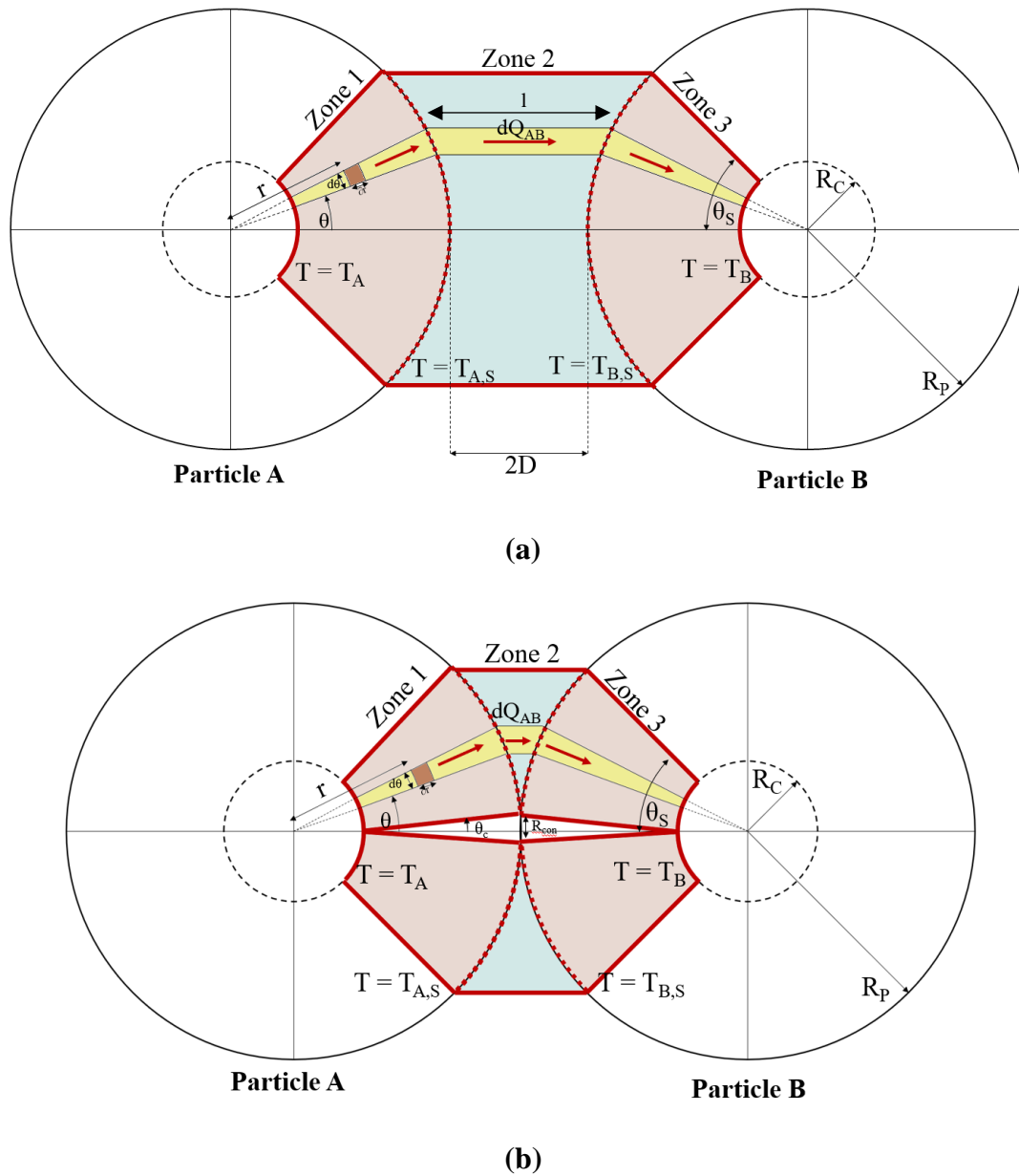


**Figure 40:** Streaming heat transfer model; (a) Particles not in contact (b) Particles in contact

The current work limits itself to mono-sized particles. Hence, both the particles are assumed to be of radius  $R_p$ . An iso-thermal core is assumed inside the particles. The size of the core,  $R_c$  can be used as a parameter that controls the influence of the intra-particulate thermal gradient on the heat transfer physics. The particles are assumed to be at a distance of  $2D$  from each other's surface. The portion of the surface area on the particles that is exposed to streaming heat is assumed to make a half angle of  $\theta_s$ . To find the thermal resistance inside particle A, a ring shaped elemental volume at an angle  $\theta$  and radial distance  $r$  is considered (shaded yellow in Figure 40). The Fourier equation of heat transfer can be written as:

$$dQ_{AB} = -k_{S,A}(2\pi r \sin\theta \, rd\theta) \frac{\partial T}{\partial r} \quad (51)$$

where,  $k_{S,A}$  is the thermal conductivity of particle A. Rearranging equation 51, we can find the heat transfer in the entire conical section at an angle  $\theta$  (shaded red in Figure 40) by integrating from core radius,  $R_c$ , to particle surface radius,  $R_p$ . Here,  $T_{A,S}$  is the temperature on the surface of particle A and  $T_A$  is its core temperature.

$$\int_{T_A}^{T_{A,S}} \partial T = \frac{dQ_{AB}}{2\pi k_{S,A} \sin\theta d\theta} \int_{R_C}^{R_P} \frac{\partial r}{r^2} \quad (52)$$

On integrating equation 52, we get a heat transfer relation for the streaming heat transfer of the zone 1 as below.

$$dQ_{AB} = \frac{T_A - T_{A,S}}{\left(\frac{1}{R_C} - \frac{1}{R_P}\right) \left(\frac{1}{2\pi k_{S,A} \sin\theta d\theta}\right)} \quad (53)$$

Finally, from equation 3, we can obtain the thermal resistance of zone 1 in particle A ( $\Omega_1$ ) as:

$$\Omega_1 = \left(\frac{1}{R_C} - \frac{1}{R_P}\right) \left(\frac{1}{2\pi k_{S,A} \sin\theta d\theta}\right) \quad (54)$$

Similarly, the thermal resistance of zone 3 in particle B ( $\Omega_3$ ) can be written as:

$$\Omega_3 = \left( \frac{1}{R_C} - \frac{1}{R_P} \right) \left( \frac{1}{2\pi k_{S,B} \sin\theta d\theta} \right) \quad (55)$$

Thermal resistance of zone 2 in fluid between particle A and B can be obtained geometrically from the length and cross-section area of the elemental ring (shaded yellow in Figure 40) as follows:

$$\Omega_2 = \frac{l}{kA} = \frac{2(R_P(1 - \cos\theta) + D)}{k_f(2\pi R_P \sin\theta R_P d\theta \cos\theta)} \quad (56)$$

where  $l$  is the length of the elemental zone 2,  $A$  is the cross-section area of zone 2, and  $k_f$  is the fluid thermal conductivity. Arranging the above thermal resistances in series, net thermal resistance of the elemental volume between particles A and B can be written as:

$$\Omega_{Eq} = \Omega_1 + \Omega_2 + \Omega_3 \quad (57)$$

Using equations 54, 55 and 56 in 57, we can write:

$$\Omega_{Eq} = \alpha \left( \frac{1}{\pi \sin\theta d\theta} \right) + \beta \left( \frac{1}{\pi \sin\theta \cos\theta d\theta} \right) \quad (55)$$

where  $\alpha$  and  $\beta$  are

$$\alpha = \left( \frac{1}{R_C} - \frac{1}{R_P} \right) \left( \frac{1}{2k_{S,A}} + \frac{1}{2k_{S,B}} \right) - \left( \frac{1}{R_P} \right) \left( \frac{1}{2k_f} \right) \quad (58)$$

$$\beta = \left( \frac{1 + \frac{D}{R_P}}{R_P} \right) \left( \frac{1}{k_f} \right) \quad (59)$$

Finally, the overall streaming heat exchange between particle A and B can be written by integrating the following expression from  $\theta = 0$  to  $\theta = \theta_s$ , as  $\Omega_{Eq}$  is a function of  $\theta$  as:

$$\int_0^{Q_{AB}} dQ_{AB} = \int_{\theta=0}^{\theta=\theta_s} \frac{T_A - T_B}{\Omega_{Eq}} \quad (60)$$

$$Q_{AB} = \pi \left( \frac{\beta \ln \left( \frac{\beta + \alpha \cos \theta_s}{\beta + \alpha} \right) - \alpha (\cos \theta_s - 1)}{\alpha^2} \right) (T_A - T_B) \quad (61)$$

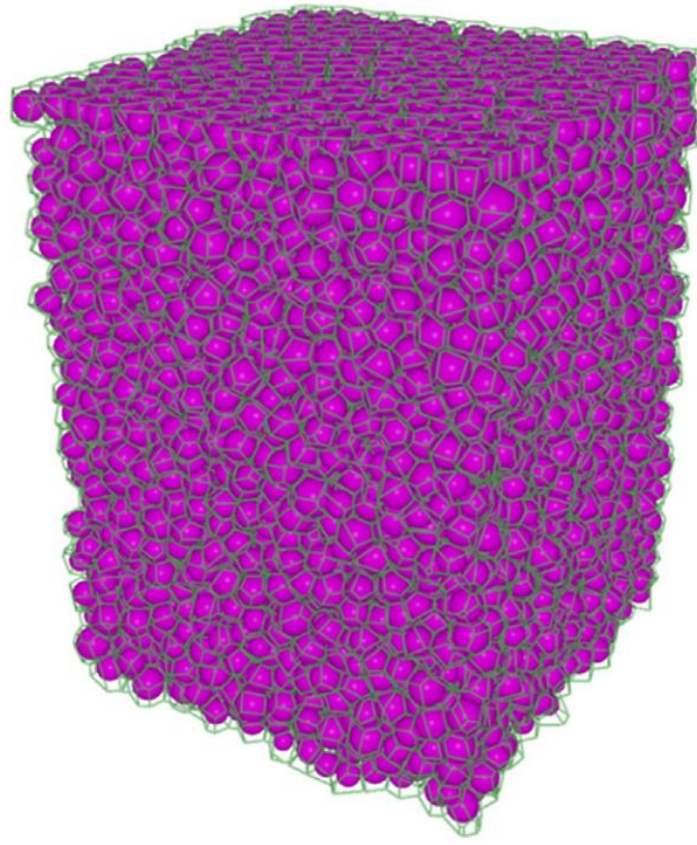
Thus, equation 61 can be used to calculate the amount of streaming heat transfer between two particles that are not touching each other. In the previous section, it was observed that streaming heat transfer exists even when two particles are in contact with each other. To calculate this case, the only variation would be the integration limits for equation 60, where the lower bound should be  $\theta_c$  which is the angle subtended from the particle centre to the radius of the contact circle.

The two unknowns in equation 61 that remain to be evaluated are  $\theta_s$  (half angle of the particle surface area exposed to streaming heat transfer) and  $R_c$  (radius of the iso-thermal core). Cheng et al. [35], assumed that the portion of the particle surface area exposed to streaming heat transfer is the projected area of the Voronoi cell surface [36] between them. A similar approach is used in this study where the value of  $\theta_s$  is calculated as a function of  $R_{VC}$  (the radius of Voronoi cell surfaces) as follows:

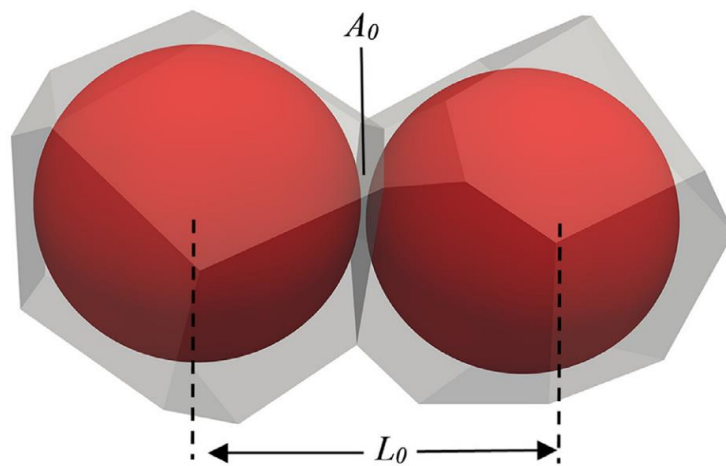
$$\cos \theta_s = \frac{R_P + D_{AB}}{\sqrt{(R_P + D_{AB})^2 + (R_{VC,AB})^2}} \quad (62)$$

$$\cos \theta_c = \frac{R_P + D_{AB}}{\sqrt{(R_P + D_{AB})^2 + (R_{Con,AB})^2}} \quad (63)$$

If particles A and B are not touching each other,  $\theta_c$  is taken as zero. Here  $R_{VC,AB}$  is the radius of the Voronoi cell surface between particles A and B. It is computationally intensive to find Voronoi tessellation in general. For the readers reference, a typical Voronoi Tessellation has individual non-overlapping cells around every particle in a packed bed as shown in Figure 41. Figure 41 (a) shows how Voronoi cells are distributed in a packed bed, while Figure 41 (b) shows the Voronoi cells of two neighbouring particles



(a)



(b)

**Figure 41:** Example of Voronoi Tessellation (a) Tessellation of a packed bed [53]; (b) Voronoi Cells encapsulating two neighboring particles [54]

Typically, Voronoi Tessellation of packed beds is required to obtain two values – 1. The number of neighbouring particles with which streaming heat transfer is taking place; 2. The area of the common Voronoi face between two neighbouring particles. In the current study, techniques were explored to avoid the use of Voronoi Tessellation to reduce the computational expenditure. In general, DEM algorithms make use of a data structure called neighbour lists. They are data structures that store the ID's of all the possible neighbours of a particle. At every time step, for every particle, their neighbour lists are searched to identify which of these particles come in contact. So instead of taking Voronoi Tessellation, the current study explores the use of these lists to evaluate the number of streaming neighbours. In general, a contact event is calculated if two mono-sized particles are at a distance of one particle diameter or less from their centres. But to evaluate if a particle is just a streaming neighbour, their centres can be located much further away than one particle diameter. For convenience, the maximum distance between two particles for them to be considered as streaming neighbours, will be referred to as the 'neighbour radius'. It is obvious that the neighbour radius is a function of the void fraction of a particle bed. In the current study, a basic empirical relation was obtained to estimate this behaviour. This was done by conducting Voronoi Tessellation for different random particle arrangements at different void fractions. The method to obtain these arrangements is described in later sections. For each particle arrangement, the local void fraction and the average distance of the neighbour particles are computed using their Voronoi cell. This data is grouped based on the local void fractions to obtain a trend between the neighbour radius and local void fraction. This is plotted in Figure 42. It can be observed that with increasing local void fraction, the neighbour radius increases. Though further study can be done to empiricalize this behaviour for polydispersed particle beds, the current work just limits itself to mono-sized particles. Thus, Figure 43 can be used to find the neighbour radius

based on local void fraction, which can calculate the number of streaming neighbours, without implementing Voronoi tessellation every time a new particle arrangement is simulated. The local void fractions can be obtained from the already existing CFD-DEM models.

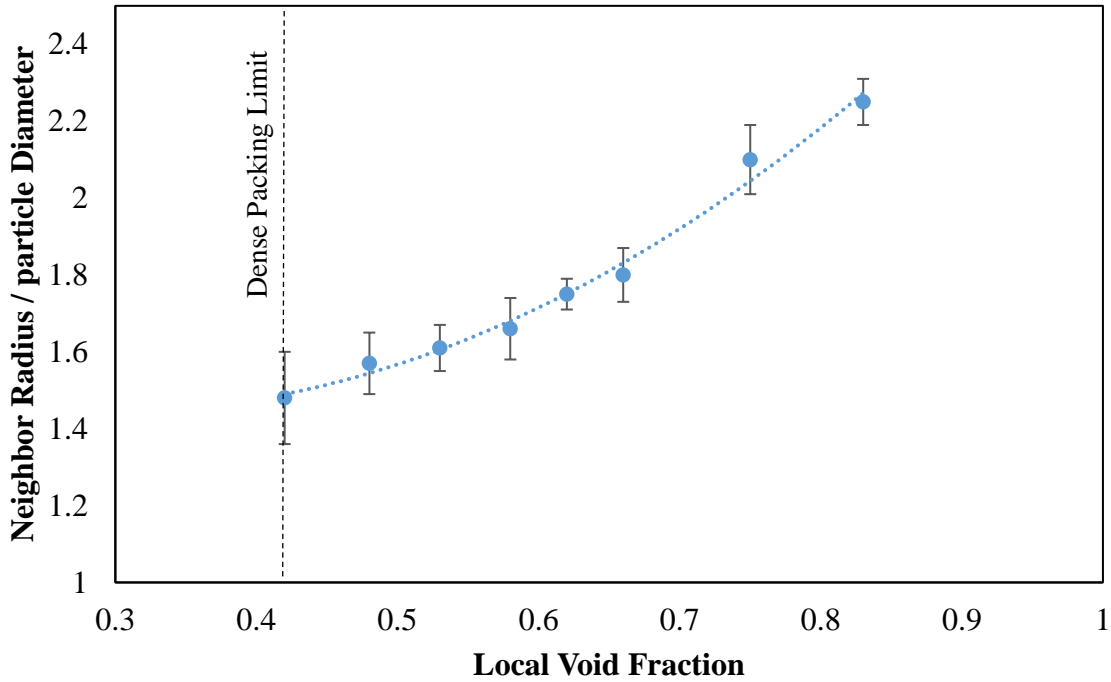


**Figure 42:** Variation of neighbor radius with local void fraction. On y-axis, the neighbor radius is scaled with particle diameter.

Similar to the number of streaming neighbours, the Voronoi face area and the  $R_{VC}$  value in equation 63 can also be estimated without actually implementing the Voronoi tessellation algorithm. For the above-mentioned particle arrangements studies were also conducted to identify how the Voronoi face area varies for different void fractions for randomized particle beds. This behaviour is plotted in Figure 43. A trend was achieved that resulted in an empirical relation between local packing fractions and the face area. This was found to be:

$$R_{VC} = 0.5R_p(PackingFraction)^{-1/3} \quad (64)$$

It is also to be noted that a similar relation was also implemented by Zhou et al.[11] in their study. Like above, the local packing fractions can be obtained from the already existing CFD-DEM models.

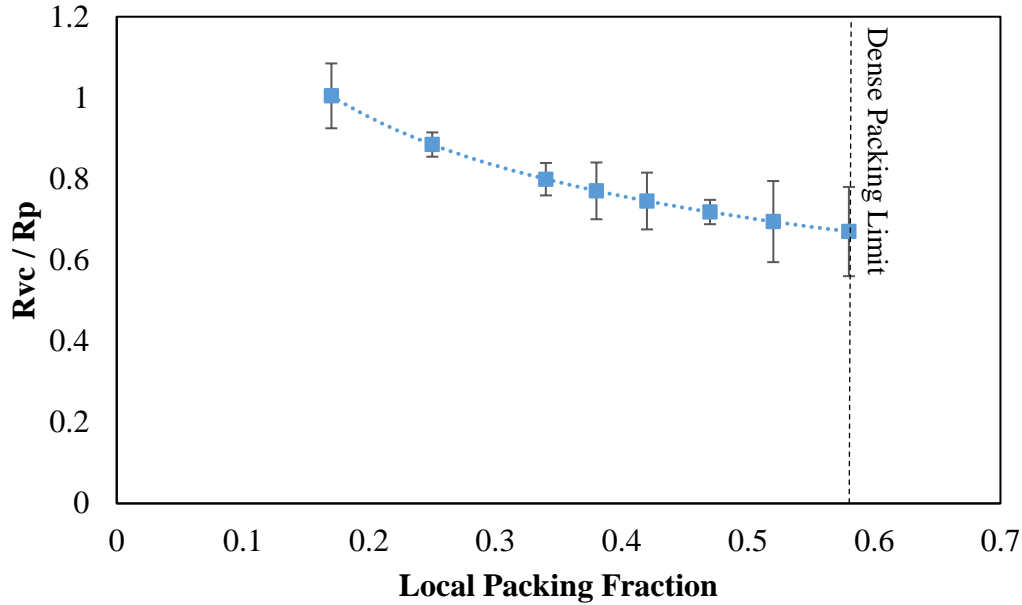


**Figure 43:** Variation of  $R_{vc}$  with local packing fraction. On y-axis, the values are scaled with particle radius

## 5.2 Core Radius Empiricalization

To calculate the values of  $R_c$ , several PR-DNS simulations were conducted with different particle sizes,  $k_f$  values, and  $k_s/k_f$  values. The simulation setup and boundary conditions were the same as those mentioned in the previous chapters (Refer to Figure 20). For each PR-DNS study, a CFD-DEM simulation was also conducted. Unlike the implementation in previous chapters, the CFD-DEM framework in this section is modified to implement the proposed streaming heat transfer model described in equation 61. With the help of scripting tools, roughly 500 PR-DNS and CFD-DEM simulations cases were conducted. In each case, the  $R_c$  values used

in the CFD-DEM simulations were tuned such that their estimates of ETC match the PR-DNS values to within 0.5%. An elaborate data set was then created to provide information about the variation of  $R_C$  for different particle radii  $R_p$ , different  $k_f$  values, and different  $k_s/k_f$  values. This is plotted in Figure 44.

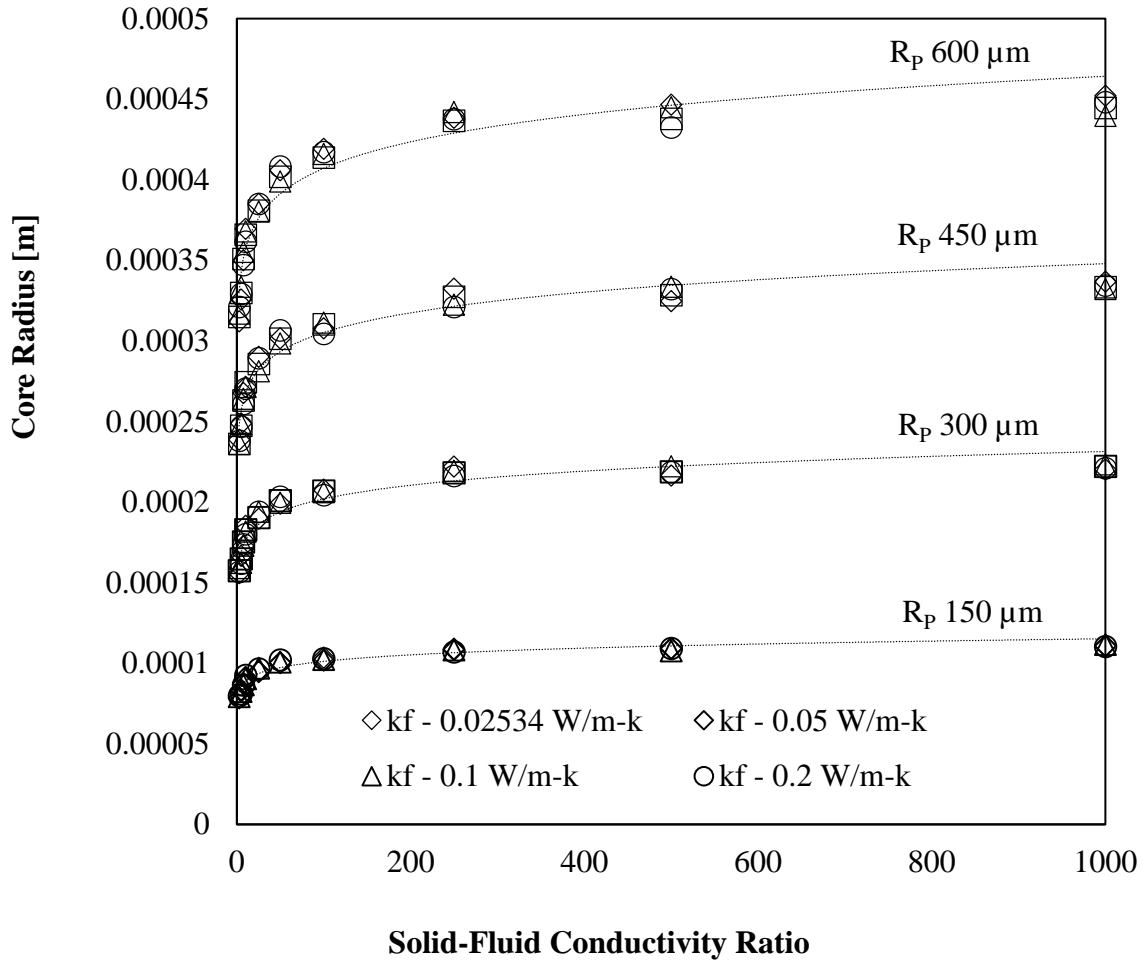


**Figure 44:** Variation of core radius with different simulation parameters

From the data shown in Figure 44, it was found that the core radius varied linearly with particle radius and varied according to a power law with varying  $k_s/k_f$ . Thus  $R_C$  can be modelled with a goodness fit of  $R^2 = 0.98$  using the following equation:

$$R_C = 0.5 R_P (k_s/k_f)^{0.055} \quad (66)$$

With closure complete, one can use equations 61 - 64, to calculate the streaming heat transfer between two particles.

## 5.3 Model Validation

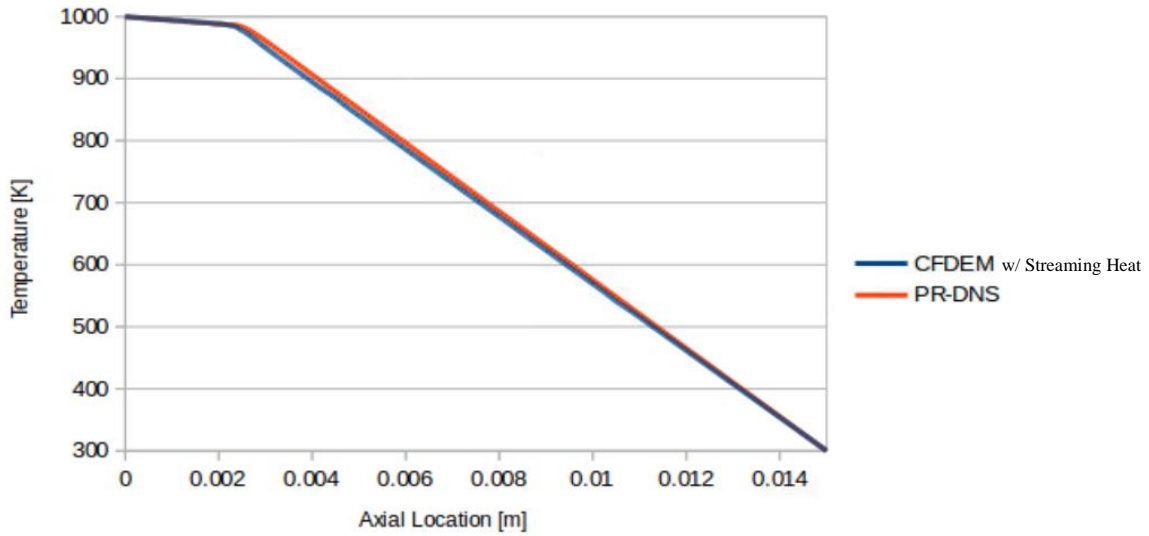
The following sub-section describes the different validation studies conducted for the model. The applicability of the streaming model is tested for different particle sizes, thermal properties and packing fractions. Additionally, a brief comparison of the proposed model and the previous models is also presented.

### 5.3.1 Comparison with PR-DNS Predictions

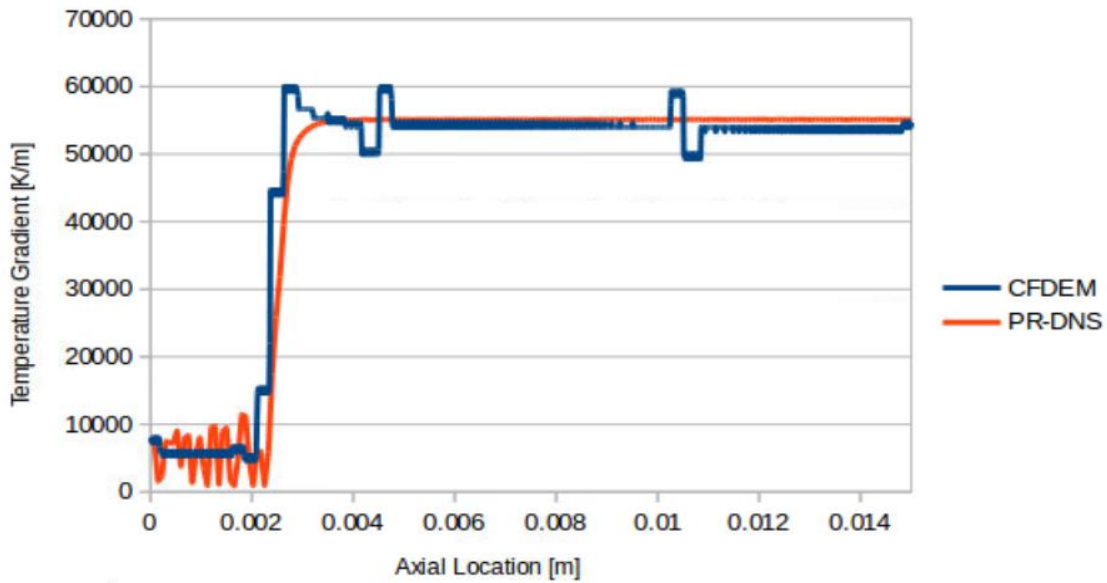
In general, proposed heat transfer models are compared with experimental results to verify their validity. But as mentioned before, this poses restrictions in terms of the range of experimental data available. Since a comprehensive data set of PR-DNS simulations is already available for different particle and geometrical parameters, the current study uses this simulation data to validate the proposed streaming model.

It was observed that all the CFD-DEM simulations, when incorporating the streaming heat transfer model perfectly replicated the axial temperature profiles obtained in PR-DNS. One such scenarios is depicted in Figure 45. Figure 46 presents the effective thermal conductivities calculated using CFD-DEM with streaming model and PR-DNS method for a static packed bed containing 300  $\mu\text{m}$  diameter particles with different fluid thermal conductivities ( $k_f$ ) and different solid-fluid conductivity ratios ( $k_s/k_f$ ). The x-axis is plotted using base 10 logarithmic scaling. It can be observed that the streaming heat transfer model is able to replicate the high fidelity (and computationally intensive) PR-DNS results accurately for a wide range of particle and fluid

thermal conductivities. Increase in  $k_{\text{Eff}}$  with  $k_{\text{Particle}}/k_{\text{Air}}$  ratio is obvious. Although not presented here, similar results were obtained for the other particle diameters ( $D_p$ ) tested.



(a)



(b)

**Figure 45:** Comparison of CFD-DEM with streaming heat and PR-DNS results for  $k_{\text{Part}} = 2.534$

W/m-K and  $k_{\text{Air}} = 0.02534$  W/m-K. (a) Axial Temperature Profile (b) Thermal gradient in z-

direction

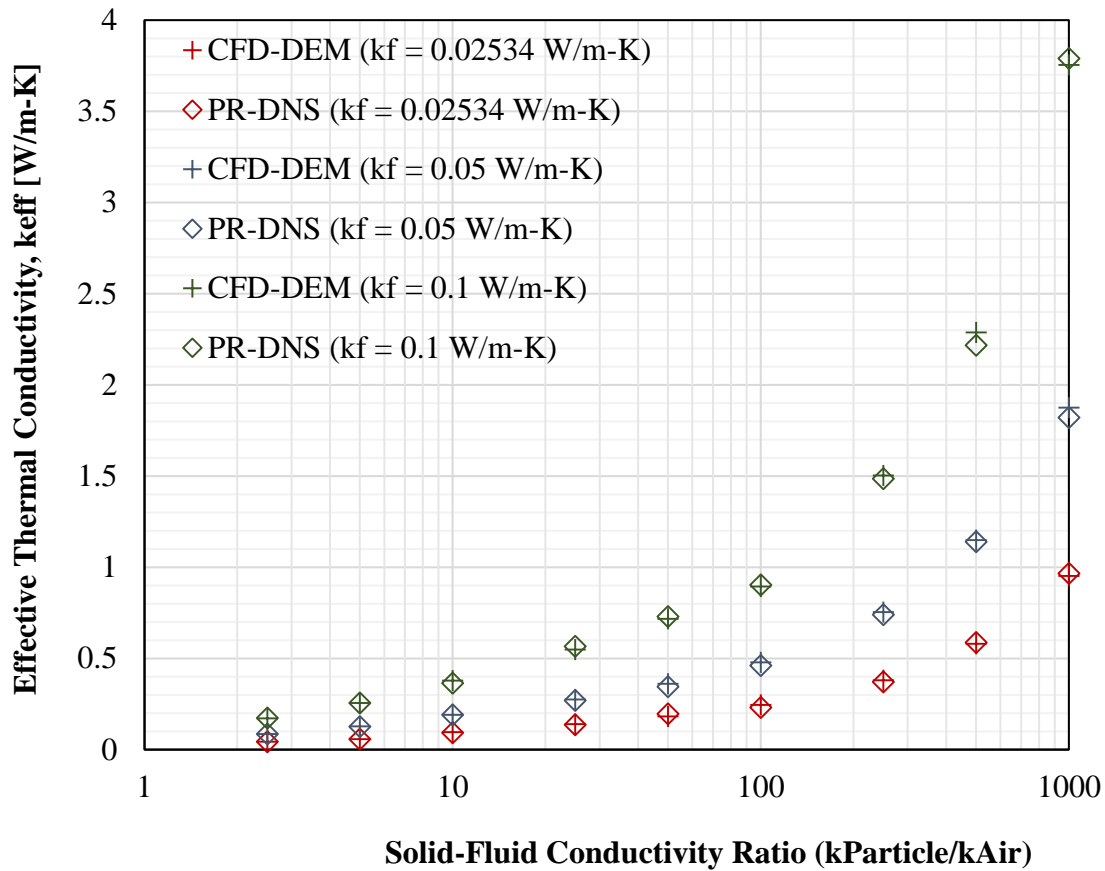


**Figure 46:** Comparison of Effective thermal conductivity estimates from CFD-DEM results with PR-DNS

### 5.3.2 Comparison with Models Available in Literature

The accuracy of the streaming heat transfer model was also tested by comparing it to the ones proposed by Cheng et al. [35]. As mentioned earlier, Cheng et al. developed two theoretical models by implementing different geometrical approaches to calculate the heat transfer between two neighbouring particles through the interstitial air. Figure 47 presents CFD-DEM predictions of  $k_{Eff}$  for different fluid thermal conductivities ( $k_f$ ) and different solid-fluid conductivity ratios ( $k_s/k_f$ ), using each of these models. Particles having a diameter of 2400  $\mu\text{m}$  (larger than others)

were used here. Both the x-axis and the y-axis are plotted using base 10 logarithmic scaling. The  $k_{Eff}$  values on the y-axis are normalized with the magnitudes of the fluid conductivity  $k_f$ .

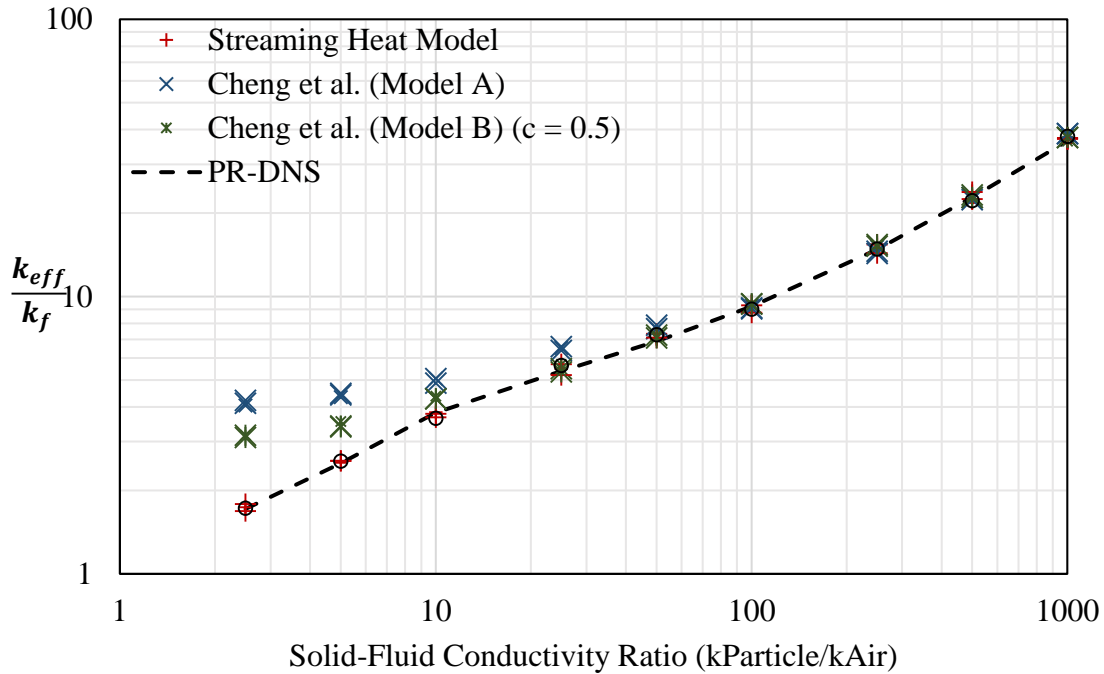


**Figure 47:** Comparison of Streaming Heat Transfer Model in Equations 61 with models proposed by Cheng et al

It can be observed that the streaming heat transfer model proposed here, showed better agreement with the PR-DNS results at low  $k_s/k_f$  ratios as compared to Cheng et al.'s Model A and Model B. This is primarily because the proposed model allows for changes in the thermal resistance inside a particle by varying the core radius ( $R_c$ ) for different properties according to equation 66. Thus, high magnitudes of intra-particulate thermal gradients, which usually occur for low  $k_s/k_f$  ratios and large particle diameter, are resolved accurately. In contrast, Models A and B proposed by Cheng et al., assume a constant thermal resistance inside the particles. Hence, they are unable to accurately capture the intra-particulate thermal gradient at these limiting conditions and result in inaccuracies as shown in Figure 47.

### 5.3.3 Model Behaviour for Different Particle Bed Void Fractions

The validity of the model was also verified for different void fractions of the packed bed. Effective thermal conductivities estimated by implementing the proposed Streaming Heat Transfer Model, were compared with PR-DNS simulations conducted on the same configurations. As mentioned previously, a packed bed is obtained in CFD-DEM framework by adding particles in the simulation domain and letting them fall freely due to gravity. This forms an average void fraction of  $\sim 40\%$  in the packed bed. In order to obtain more dilute configurations, or higher void fraction, one typically blows a jet of air from the bottom of the particle container. This fluidizes the packed bed to higher void fractions. The degree of fluidization governs the void fractions of the bed. In such a scenario, convection heat transfer from the particles to the surrounding air becomes the dominant mode of heat transfer. Moreover, a steady flow of air through the interstitial spaces might also have some influence on the streaming behavior. As a result, other options are explored here to obtain higher void fractions. In a previous study, Singhal et al. [55] achieved a randomly generated particle arrangement of higher void fractions, by injecting them into the simulation domain without a gravitational force. These particles are initially allowed to overlap to a significant degree thus creating large repulsive forces between the particles. As a result, the particles begin to accelerate in different direction, moving around and colliding each other in a random fashion. Since there is no gravity, the particles never settle to form a dense packing. After a certain amount of time, the simulation is stopped, and the random particle positions are used to generate a porous particle bed. The primary issue with this approach is that it allows very little control of the void fractions achieved. As a result, we slightly modified this approach. The particles are first allowed to settle down in the simulation domain due to gravity. Once the kinetic energy of the bed becomes zero, particle-particle interaction forces and gravity are turned off. This ensures

every particle is experiencing a net zero force. Finally, the void fraction of the bed is then varied by reducing the particle size, by keeping their center in the same positions. This is illustrated in Figure 48.

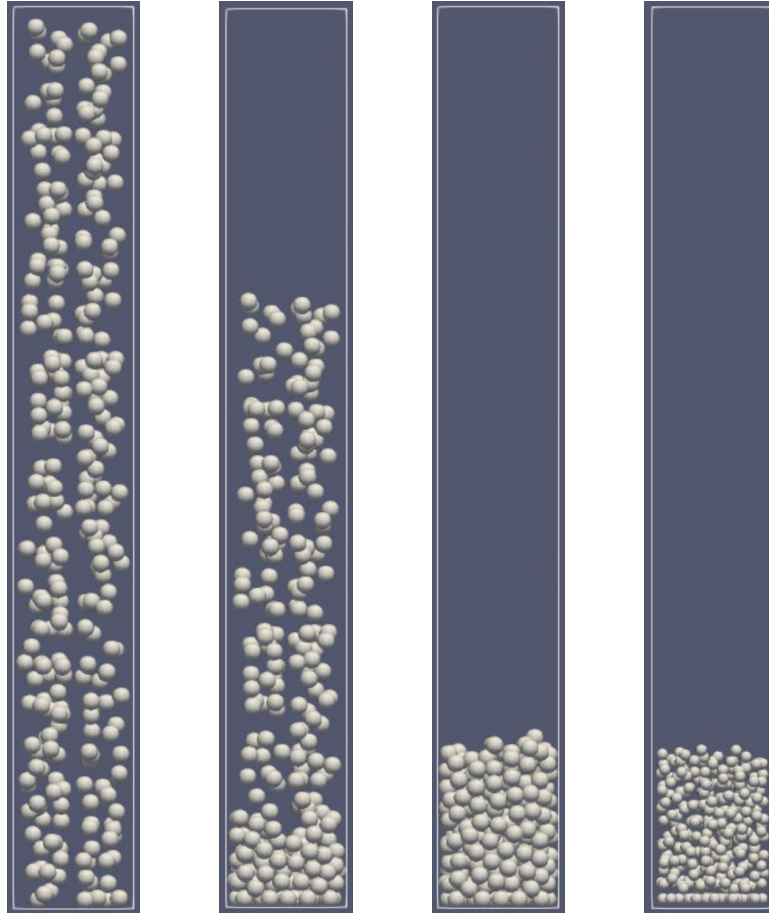
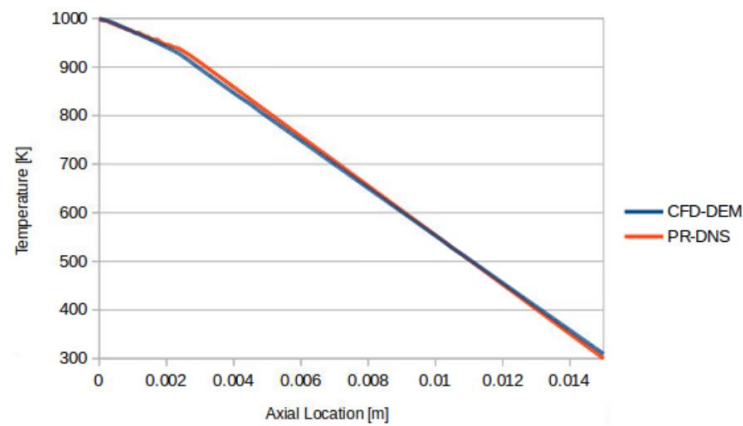


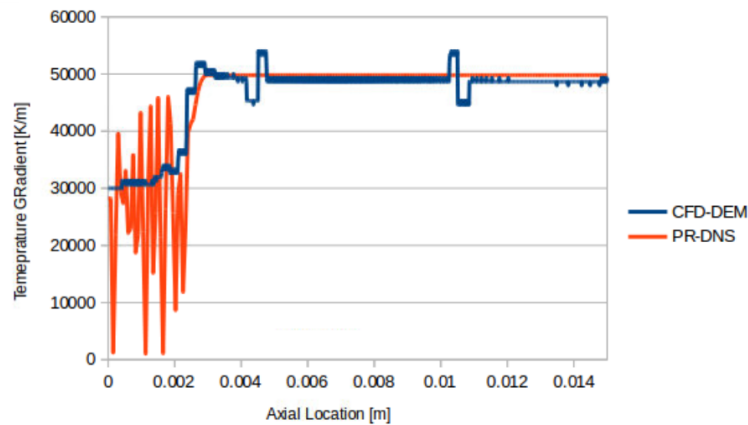
**Figure 48:** Generation of a dilute packing configuration. Image progression from left to right indicating particle insertion, particle settling and particle size reduction in sequence

With different particle diameters, different void fractions were obtained. Several packing configurations were achieved for each void fraction tested. Using the same boundary conditions as before, temperature profiles were obtained in both Pr-DNS simulations and CFD-DEM simulations. In the Figure 49, the temperature profiles and gradients of a case with  $k_{Air}$  as 0.02534 W/m-K,  $k_{Particle}/k_{Air}$  ( $k_{Part}/k_{Air}$ : Ratio of solid-fluid thermal conductivity) as 100 and void

fraction as 75% are plotted. Both the CFD-DEM and Pr-DNS results match. Similar observations were obtained for all the remain cases. Comparing Figure 49 with Figure 45, it can also be identified that the  $k_{Eff}$  in this scenario is lesser than the case with denser packing. In Figure 50, the variation of  $k_{Eff}$  with void fraction was also plotted for PR-DNS and CFD-DEM results. This also shows that both the implementations resulted in similar predictions of  $k_{Eff}$ . Hence it can be concluded that the streaming model is able to capture the heat transfer behavior over a wide range of void fraction values.



(a)



(b)

**Figure 49:** Comparison of CFD-DEM and PR-DNS results for a void fraction of 75%. (a) Axial Temperature Profile (b) Thermal gradient in z-direction

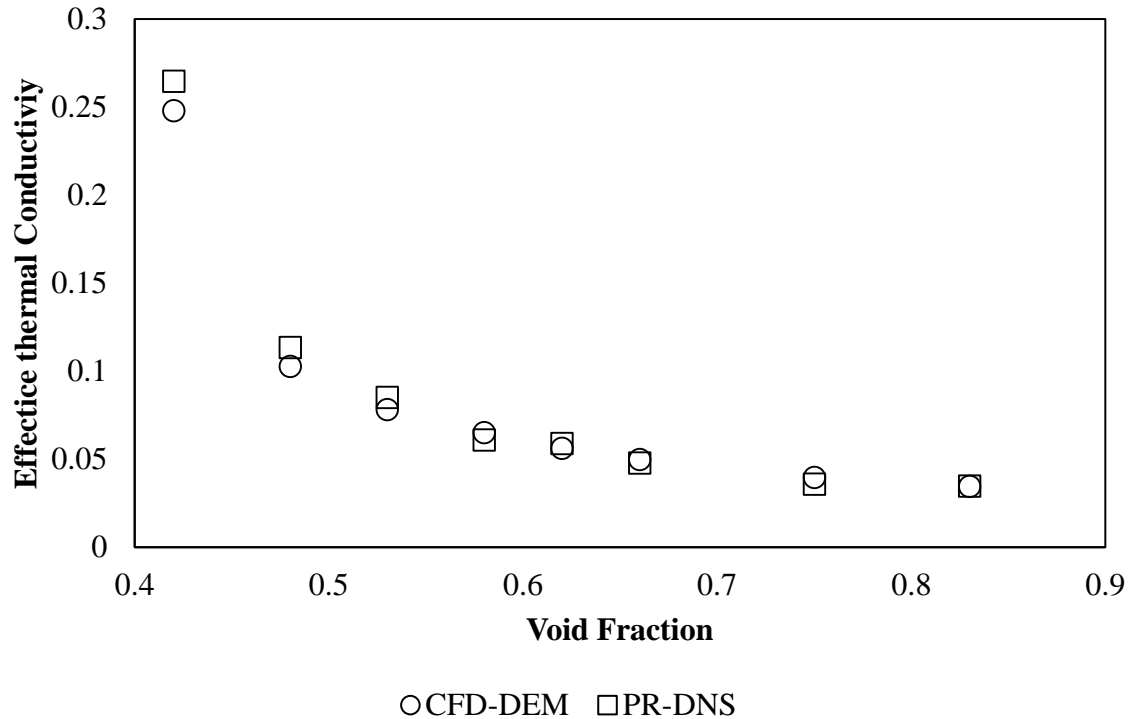


**Figure 50:** Variation of effective thermal conductivity of a packed with void fraction as observed in CFD-DEM and PR-DNS implementations

## 5.4 Heat Transfer Insights from CFD-DEM

Since the proposed streaming model has been validated over a wide range of particle conductivities, fluid conductivities and void fractions, it was used to gain a deeper understanding of the heat transfer physics in a particle bed. The following sub-sections try to explore the different insights that can be observed from the proposed CFD-DEM framework.

### 5.4.1 Preliminary Observations

Since the current work focuses only on showcasing the implementation of CFD-DEM and heat transfer models in packed beds, a comprehensive study to understand packed bed thermal behaviour is not included in this manuscript. Nevertheless, some simple insights drawn from the

different simulation cases are discussed here. Figure 51 shows the variation of  $k_{Eff}$  with the number of particles in a cylindrical container. In general, increasing number of particles in a constant cross-section area static bed results in increasing stresses at particle-particle contact points due to the added weight. This leads to high particle-particle contact area and thereby improves the heat transfer behaviour. However, after the height of the granular media crosses a certain limit, the stresses inside the particle bed remain constant no matter how high the bed is (unlike for liquids). As mentioned earlier, this phenomenon is known as the Janssen effect [7]. The asymptotic nature of  $k_{Eff}$  in packed beds with bed height is because the particle-particle contact areas remain constant even if the height of the bed continues to increase, once it is greater than the Janssen limit. The CFD-DEM data shown in Figure 51 correctly show this trend

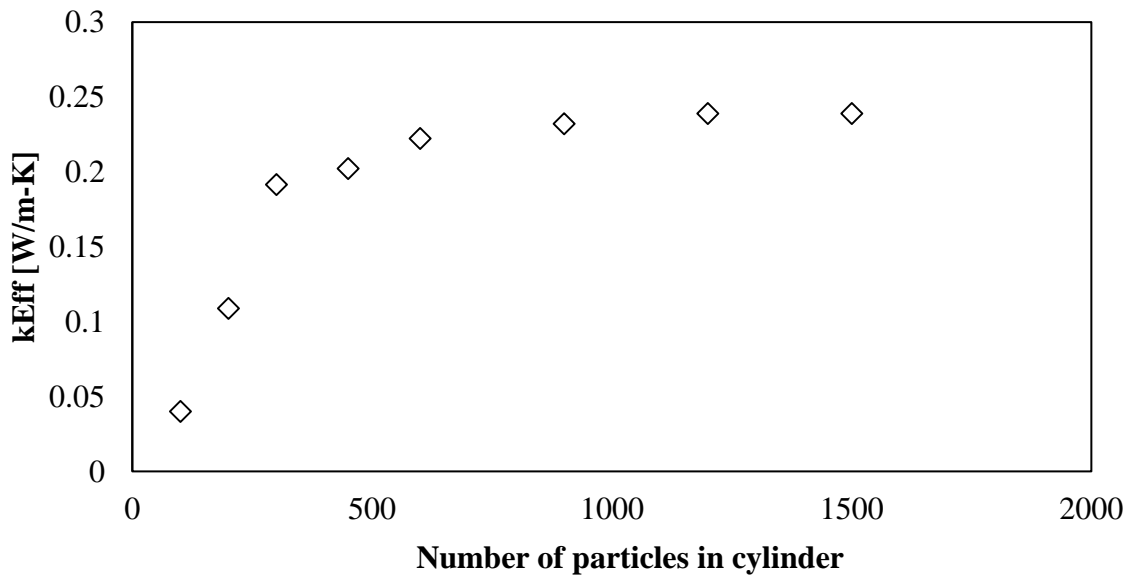


**Figure 51:** Variation of  $k_{Eff}$  with number of particles inside the packed bed

Figure 52 shows the CFD-DEM predicted variation of  $k_{Eff}/k_f$  with  $k_s/k_f$ . It shows that for larger ratios of  $k_s/k_f$ , the effective thermal conductivity is larger for larger diameter particles. This believed to be due to a reduction in the overall thermal resistance as  $D_p$  increases.

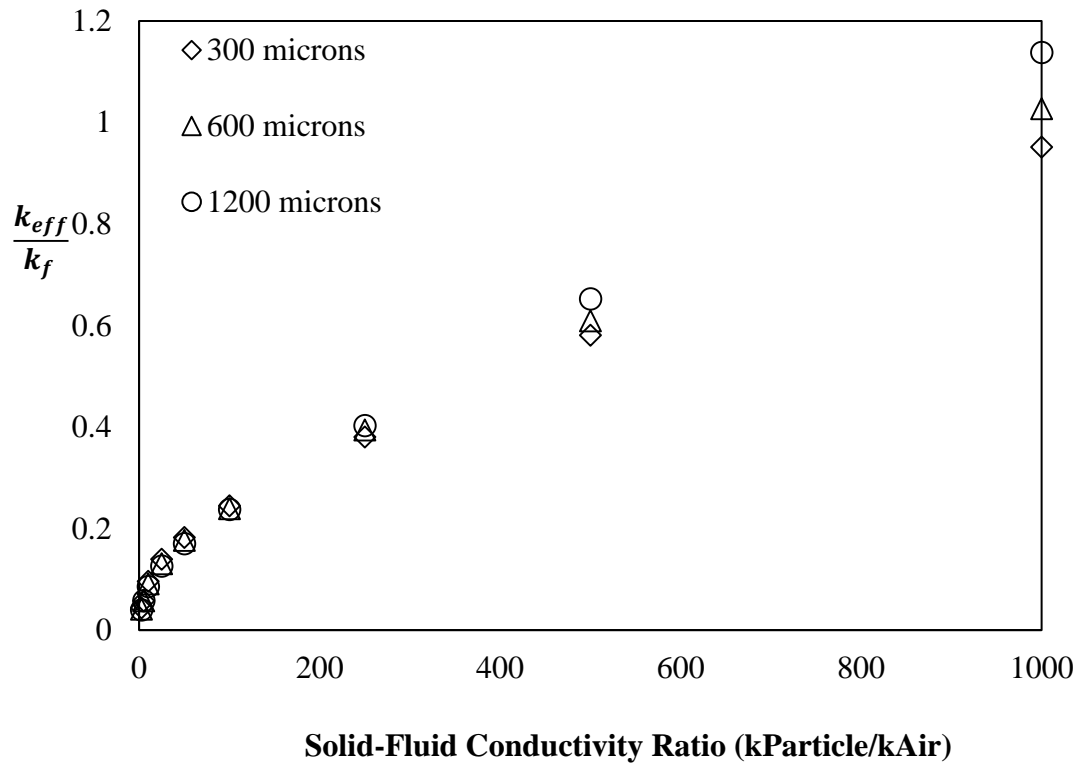


**Figure 52:** Variation of  $k_{eff}$  with number of particles inside the packed bed

### 5.4.2 Relative Contribution of Different Heat Transfer Phenomena in a Packed Bed

Throughout the discussion in the last two chapters, it was emphasised that there are three modes of heat transfer in a particle bed – 1. Particle-Particle Contact Conduction, 2. Particle-Air Convection, and 3. Particle-Particle Streaming heat transfer. Additionally, the particle-particle streaming heat transfer can further be classified into Contact Streaming and Non-Contact Streaming (Refer to Figures 40 a and b). Since all the simulation studies conducted in this work are steady state, the net heat flux for every particle in the system will always be zero. This is also depicted in Figure 53 where the net heat fluxes of all the particles in a simulation with 40% void fraction, 300  $\mu\text{m}$  particles, 0.02534 W/m-K  $k_{Air}$  and 2.534 W/m-K  $k_{Part}$  is plotted.

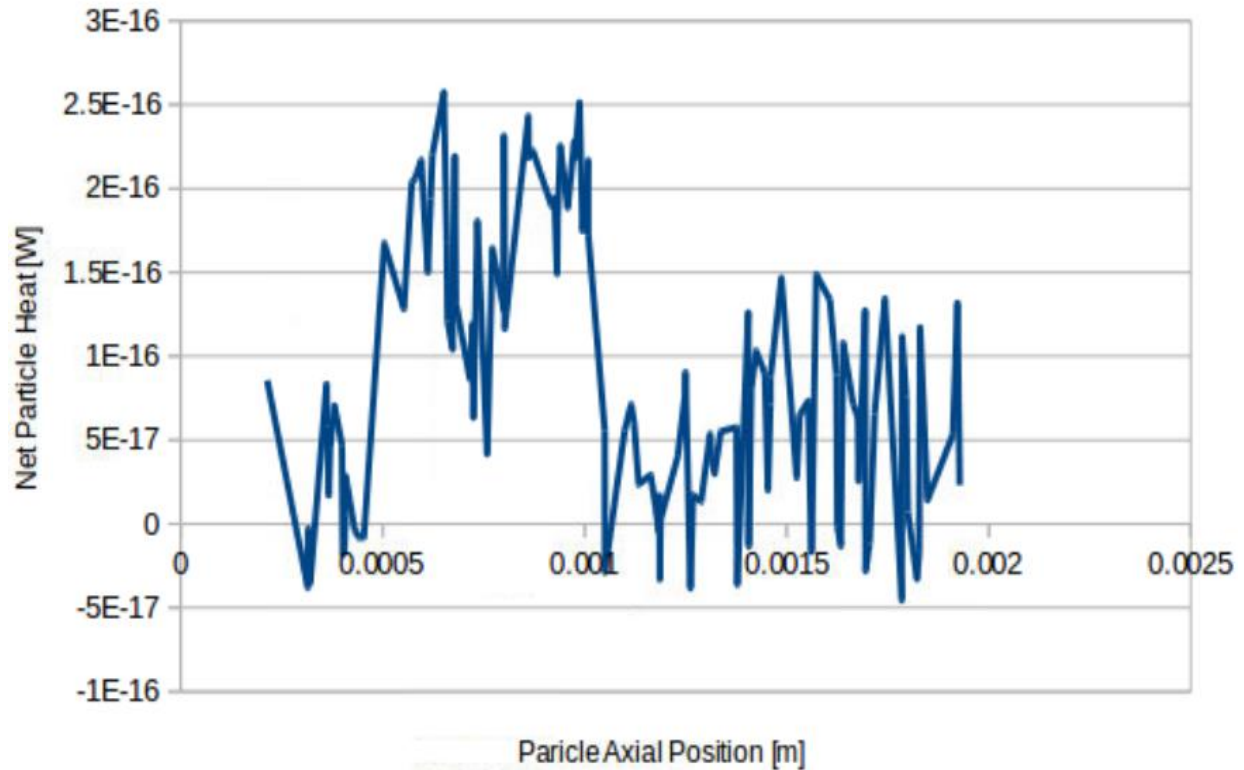


**Figure 53:** Net heat for every particle in the simulation domain

In Figures 54 (a) and (b), the total particle-air (convection) and particle-particle (conduction + streaming) heat transfer rates are plotted for the same case. For steady state heat transfer, the amount of heat energy a particle takes in or gives out is balanced by the heat energy it exchanges with the surrounding air. In chapter 4, it was observed that adding interstitial air, instead of having vacuum increased the heat transfer coefficient drastically. This was initially thought of as the superior contribution of particle-air convection. But, the much smaller magnitudes of convection heat transfer, revealed that it is the streaming phenomena, which also arises in the presence of air, dominates the overall thermal behaviour of packed beds. The slightly higher magnitudes of convection heat transfer shown on the left side of the graphs are due to the presence of the wall boundary condition.

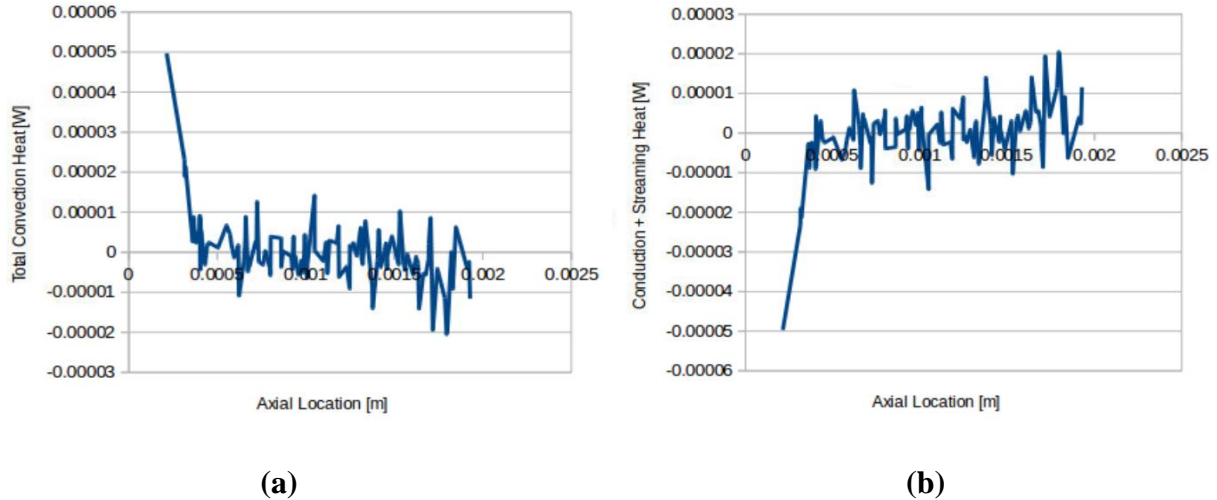
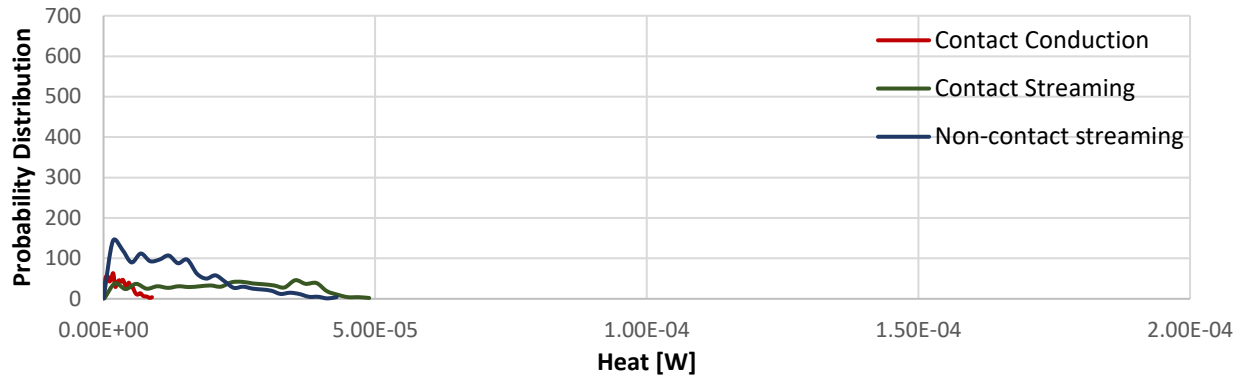
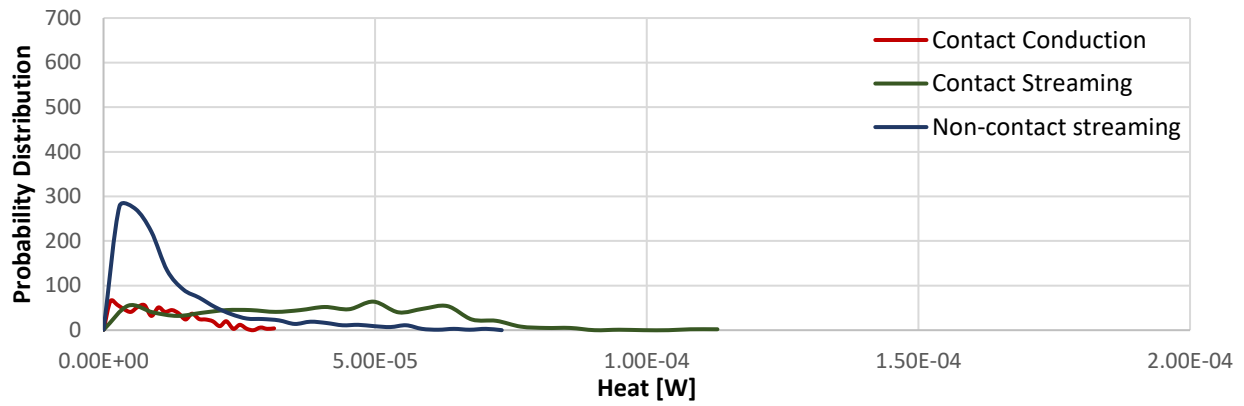


**Figure 54:** (a) Total Convection heat transfer on a particle (b) Total Conduction and streaming heat on a particle

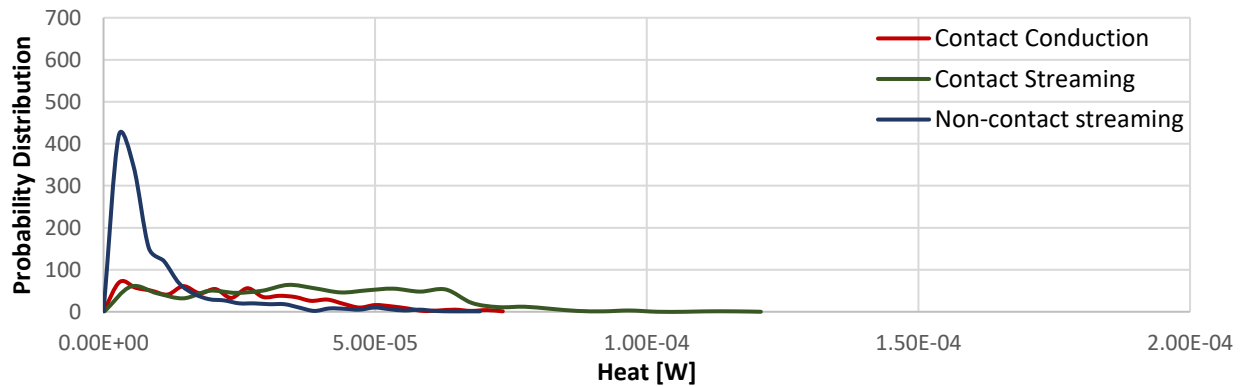
In Figures 55 (a), (b) and (c), a probability distribution of contact conduction, contact streaming and non-contact streaming magnitudes at every particle-particle interaction is plotted. It can be observed that non-contact streaming heat transfer phenomenon is occurring at more locations than contact streaming and contact conduction. Nevertheless, the average magnitudes of non-contact streaming heat transfer are always less than the other two. This can be attributed to the high thermal resistance in non-contact streaming. It can also be observed that with increasing  $k_{\text{Particle}}/k_{\text{Air}}$  (solid-fluid thermal conductivity ratio), the contact streaming and contact conduction magnitudes become much more prominent. In Figure 56, the percentage contribution of each heat transfer mechanism in the direction of heat flow is plotted for a void fraction of 42%. As expected, it can be observed that the particle-particle contact conduction becomes more prominent with increasing  $k_{\text{Particle}}/k_{\text{Air}}$ , while both the streaming heat phenomena's influence becomes low. It can also be observed that at low  $k_{\text{Particle}}/k_{\text{Air}}$ , the streaming phenomena dominates while for higher  $k_{\text{Particle}}/k_{\text{Air}}$ , the contact conduction dominates.



(a)



(b)



(c)

**Figure 55:** Probability distribution of each heat transfer mechanisms for (a)  $k_{\text{Particle}}/k_{\text{Air}} = 2.5$ , (b)  $k_{\text{Particle}}/k_{\text{Air}} = 25$ , and (c)  $k_{\text{Particle}}/k_{\text{Air}} = 250$

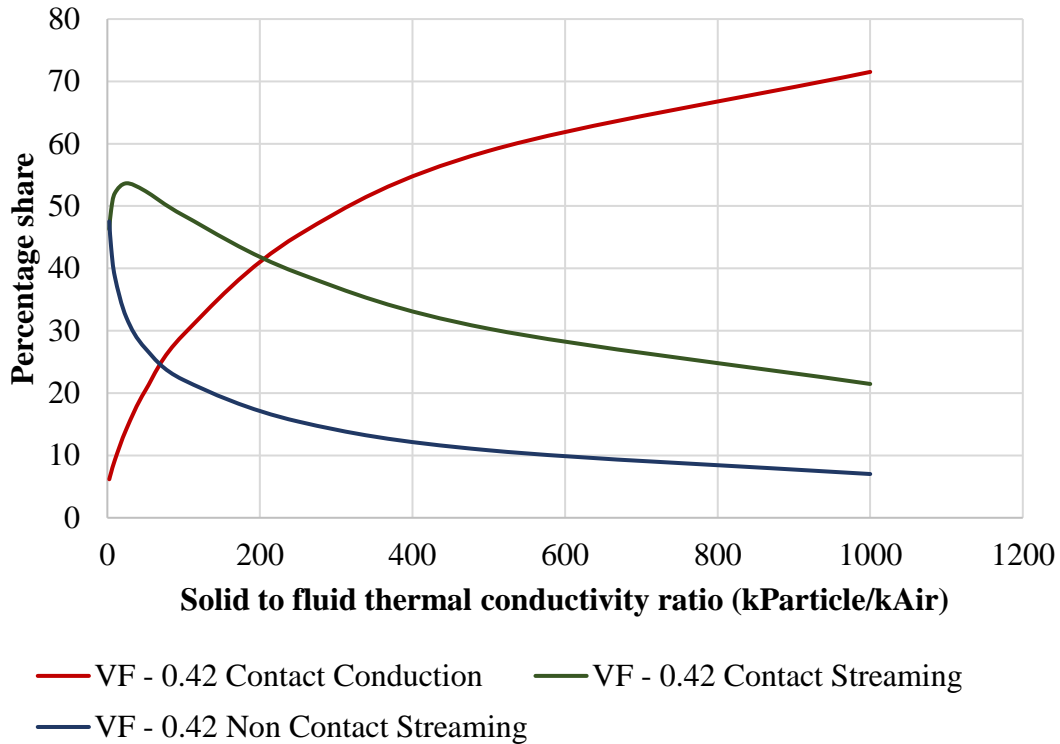


**Figure 56:** Percentage shares of different heat transfer behaviors to the overall heat for void fraction of 42%

Thus, the above observations help in gaining a detailed understanding of the heat transfer phenomena in a particle bed as a function of the packing structure. These distributions can further be used to develop a reliable analytical model for any configuration of particle bed.

### 5.4.3 Influence of Particle Bed Void Fraction on the Heat Transfer Physics

Since the proposed CFD-DEM framework and the streaming heat transfer model works for a wide range of particle bed packing fractions, the current study also evaluated the heat transfer behaviour for several dilute packing configurations. As mentioned in the previous section, dilute packing was obtained by reducing the particle diameter and fixing their positions. As a result, the number of contact points in the particle bed becomes negligible. Hence, we will only study the

behaviour of non-contact streaming heat transfer. In Figure 57, the probability distributions of non-contact streaming heat for different void fractions are plotted.

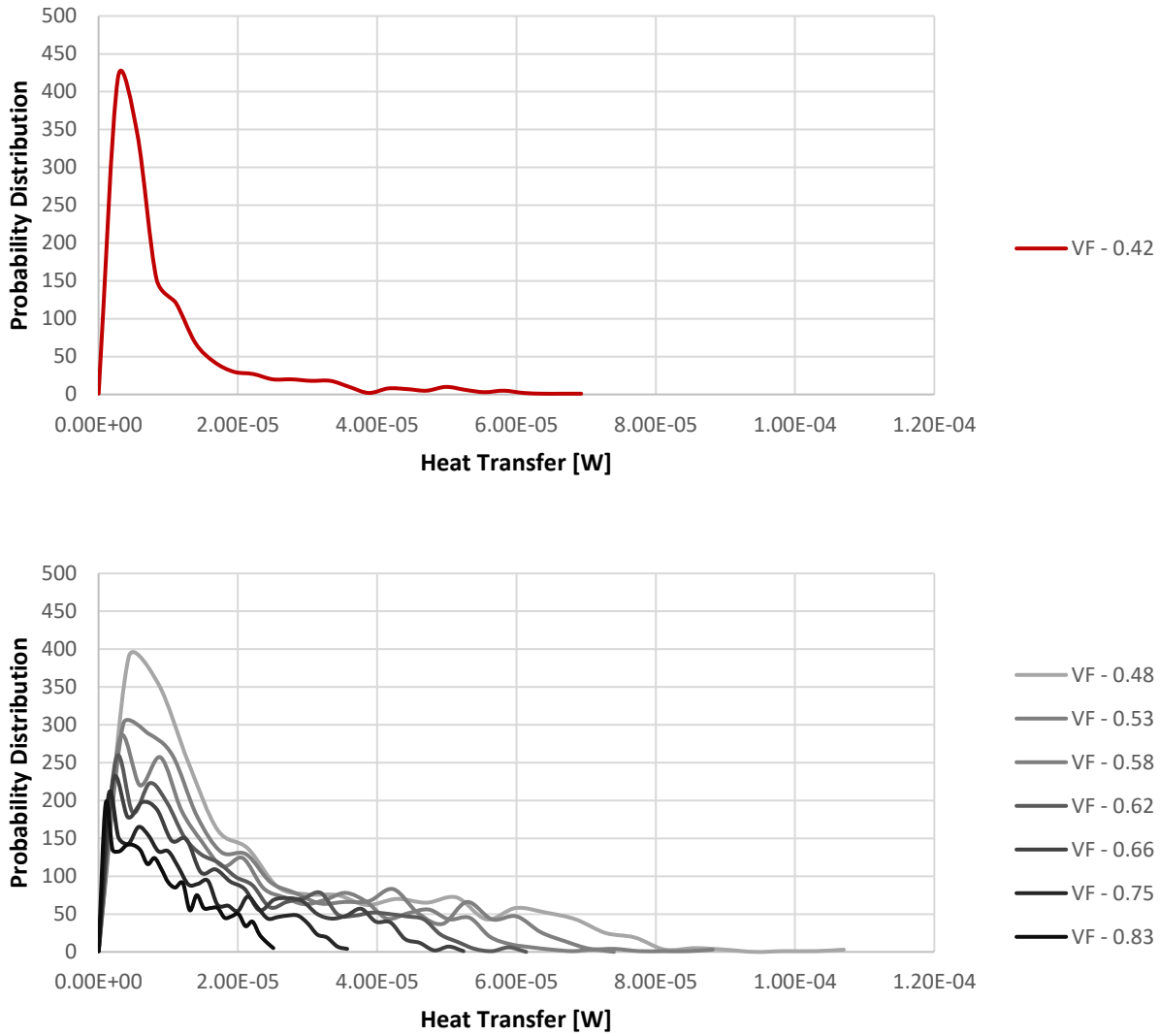


**Figure 57:** Probability distribution of Non-Contact streaming for different void fractions

It can be observed that the average streaming heat transfer magnitude is less for the densest packing compared to other dilute packings. This is peculiar as the  $k_{Eff}$  of densest packing is higher than other configurations. This behaviour is because of the presence of particle-particle contacts in the densest packing, which contribute more to the overall heat transfer. For the dilute packings, it can be observed that the average streaming heat goes down with increasing void fraction. This

is obviously due to an increased particle-particle distance for dilute packings. In the Figure 58, the variation of  $k_{\text{Eff}}$  with  $k_{\text{Particle}}/k_{\text{Air}}$  (solid-fluid thermal conductivity ratio) for different void fraction is plotted. Both the CFD-DEM and PR-DNS results are plotted. As observed in the previous section the PR-DNS and CFD-DEM results match. Also, it was observed that  $k_{\text{Eff}}$  increases with increasing  $k_{\text{Particle}}/k_{\text{Air}}$ . But this increase is very minimal for dilute packing fractions. This peculiar behaviour can be attributed to the fact that there are no particle-particle contact points in the dilute arrangement. In general, increase in  $k_{\text{Particle}}/k_{\text{Air}}$  increase the streaming heat transfer between particles. But in dilute flows, the contribution of streaming is very small by definition. Hence,  $k_{\text{Eff}}$  doesn't change with  $k_{\text{Particle}}/k_{\text{Air}}$  for dilute flows.

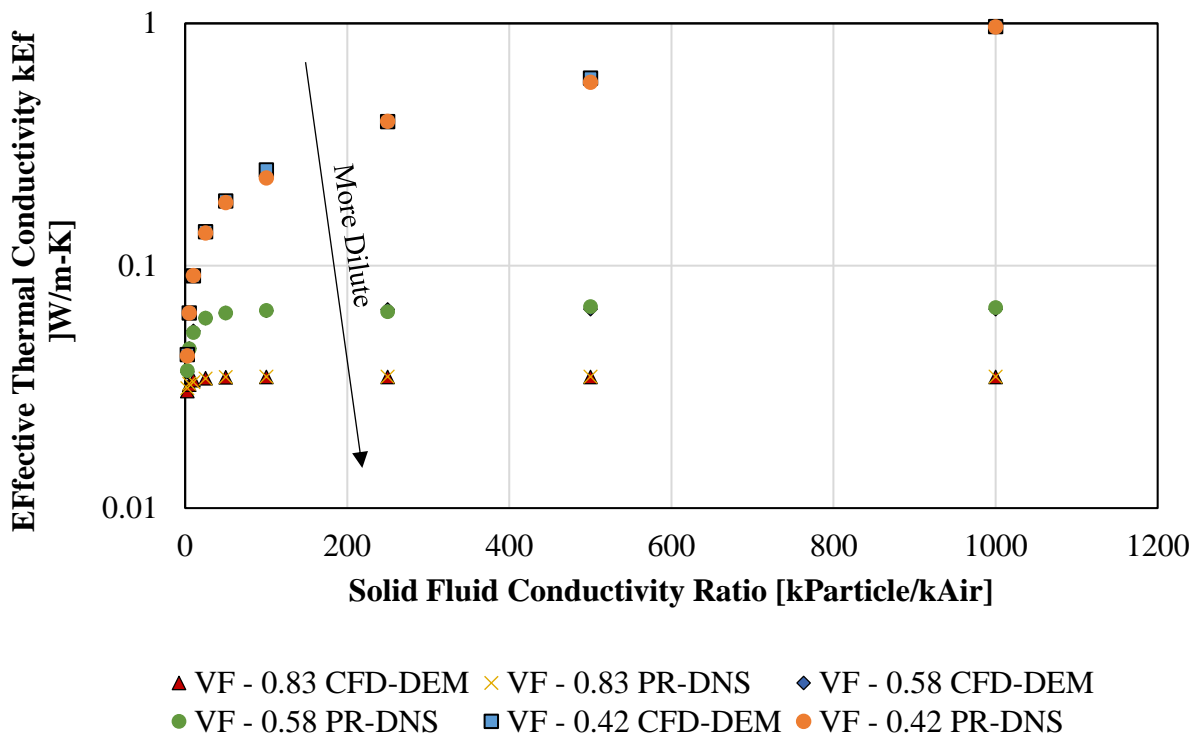


**Figure 58:** Variation of  $k_{\text{Eff}}$  with  $k_{\text{Particle}}/k_{\text{Air}}$  for different void fractions.

In this way several heat transfer insights were obtained via CFD-DEM simulations, without high computational expenditure.

## Chapter 6

# Conclusions

Throughout this work, the different flow and heat transfer characteristics of granular media are studied computationally. Initially, the research sought to gain an understanding of the flow physics that have either a direct or indirect correlation to heat transfer physics of dense granular flows. The simulation results showed that the residence time of particle-wall contacts decreased with increasing flowrates. The differences in the estimated and the actual residence time also gave a qualitative sense of particle motion near the wall. The variation of near wall packing fraction with flowrates was also studied and was found to decrease with increasing flowrates. To understand the fluctuation behavior of the flows, the standard deviation values for different particle flowrates was studied. It was observed that the normalized turbulent intensity near wall decreases with increasing flow rates

It is well understood within the scientific community that the heat transfer to a particulate bed/flow is impeded by the structured contact behavior of particles at the heated surface. A common approach implemented to model the heat transfer behavior involves dividing the bed/flow into two regions: a bulk region with effective properties of the particulate bed and a wall-adjacent layer with an increased thermal resistance. To model the wall-adjacent thermal resistance, information about the packing fraction of the layer and the number of particles in contact with the

wall are required. Discrete Element Method (DEM) simulations were implemented to study the flow mechanics of particles in the wall-adjacent layer. Variation of the packing fraction and number of particle contacts with mean flow velocity and the tube-to-particle diameter ratio were examined. Empirical correlations were developed to capture the trends observed in the DEM data. Both the packing fraction and the number of contacts were found to decrease with increasing flow rate.

Subsequently, the research focused on analyzing the detailed heat transfer characteristics of a densely packed bed of mono-sized particles were studied computationally. Particle-Resolved Direct Numerical Simulations (PR-DNS) were implemented to identify the different heat exchange phenomena a particle experiences. Among those, streaming heat transfer, which describes the significant heat exchange that occurs between particles via interstitial air is discussed. A theoretical model was developed to capture the streaming heat transfer physics and was tuned with the help of PR-DNS simulations. The proposed model presented here is different from previous ones, as it captures the influence of intra-particulate thermal gradients on the heat transfer physics using an empirical relation to calculate the isothermal core size as a function of particle diameter, and ratio of thermal conductivities. Though the model was developed for particle diameter values ranging from 150 - 600  $\mu\text{m}$  and ratio of thermal conductivities values ranging from 2.5 – 1000, we believe that the relations also hold outside these ranges as we captured the physical effects that rooted from lumped capacitance assumption. Nevertheless, future studies should be conducted to evaluate the operational range of this model.

Finally, the implementation of CFD-DEM methodology was demonstrated as an accurate way of computationally studying the heat transfer behavior of static packed beds. The governing equations involved in DEM solvers for the particles and the Finite Volume CFD solvers for the

interstitial fluid were presented. Heat transfer models were implemented to resolve the particle-particle conduction, particle-air convection, and particle-particle streaming phenomenon. The application of a new streaming heat transfer model was compared with the existing models in literature. It was observed that the new model can capture the thermal behavior of packed beds for a wide range of particle properties as it considers the effects of intra-particulate temperature gradients accurately. Though only one configuration was discussed (i.e. static packed bed) in this manuscript, it is believed that similar methodology can be implemented to other static particulate systems in future.

## REFERENCES

- [1] G. Flamant, “Theoretical and experimental study of radiant heat transfer in a solar fluidized-bed receiver,” *AIChE J.*, vol. 28, no. 4, pp. 529–535, Jul. 1982.
- [2] N. P. Siegel, C. K. Ho, S. S. Khalsa, and G. J. Kolb, “Development and Evaluation of a Prototype Solid Particle Receiver: On-Sun Testing and Model Validation,” *J. Sol. Energy Eng.*, vol. 132, no. 2, p. 021008, 2010.
- [3] T. Tan and Y. Chen, “Review of study on solid particle solar receivers,” *Renew. Sustain. Energy Rev.*, vol. 14, no. 1, pp. 265–276, 2010.
- [4] S. Giuliano, R. Buck, and S. Eguiguren, “Analysis of Solar-Thermal Power Plants With Thermal Energy Storage and Solar-Hybrid Operation Strategy,” *J. Sol. Energy Eng.*, vol. 133, no. 3, p. 031007, 2011.
- [5] H. Chen, Y. Chen, H.-T. Hsieh, and N. Siegel, “Computational Fluid Dynamics Modeling of Gas-Particle Flow Within a Solid-Particle Solar Receiver,” *J. Sol. Energy Eng.*, vol. 129, no. 2, p. 160, 2007.
- [6] G. Flamant *et al.*, “A New Heat Transfer Fluid for Concentrating Solar Systems: Particle Flow in Tubes,” *Energy Procedia*, vol. 49, pp. 617–626, 2014.
- [7] H. A. . Jassen and M. Sperl, “Experiments on corn pressure in silo cells - Translation and comment of Janssen’s paper from 1895,” *Granul. Matter*, vol. 8, no. 2, pp. 59–65, 2006.
- [8] H. A. Beverloo, H. A. A. Leniger, J. Van De Velde, W. A. Beverloo, H. A. A. Leniger, and J. Van De Velde, “The flow of granular solids through orifices,” *Chem. Eng. Sci.*, vol. 15, no. 3–4, pp. 260–269, Sep. 1961.
- [9] P. a. Cundall and O. D. L. Strack, *A discrete numerical model for granular assemblies*, vol. 30, no. 3. 1980.

- [10] R. M. A. Nedderman, *Statics and Kinematics of Granular Materials*. Cambridge: Cambridge University Press, 1992.
- [11] O. Pouliquen and R. Gutfraind, “Stress fluctuations and shear zones in quasistatic granular chute flows,” vol. 53, no. 1, 1996.
- [12] D. Chen, J. F. Klausner, and R. Mei, “A fluid mechanics approach to describing the behavior of pneumatically conveyed powder plugs,” *Powder Technol.*, vol. 124, no. 1–2, pp. 127–137, 2002.
- [13] O. Pouliquen, “How do grains flow: Towards a simple rheology of dense granular flows,” *Powders and Grains*, no. I, p. 7, 2005.
- [14] Y. Zhang, E. W. C. Lim, and C. H. Wang, “Pneumatic transport of granular materials in an inclined conveying pipe: Comparison of computational fluid dynamics-discrete element method (CFD-DEM), electrical capacitance tomography (ECT), and particle image velocimetry (PIV) results,” *Ind. Eng. Chem. Res.*, vol. 46, no. 19, pp. 6066–6083, 2007.
- [15] GDR MiDi, “On dense granular flows,” *Eur. Phys. J. E. Soft Matter*, vol. 14, no. 4, pp. 341–65, Aug. 2004.
- [16] J. T. Jenkins and D. Berzi, “Kinetic theory applied to inclined flows,” *Granul. Matter*, vol. 14, no. 2, pp. 79–84, 2012.
- [17] O. Pouliquen and F. Chevoir, “Dense flows of dry granular material,” *Comptes Rendus Phys.*, vol. 3, no. 2, pp. 163–175, 2002.
- [18] M. F. Watkins and R. D. Gould, “Dense granular flows as a new heat transfer fluid for concentrated solar power,” in *International Mechanical Engineering Congress & Exposition*, 2015.
- [19] W. N. Sullivan and R. H. Sabersky, “Heat Transfer to Flowing Granular Media,” vol. 18,

- no. 1, pp. 97–107, 1975.
- [20] D. Huang, G. Sun, and K. Lu, “Influence of granule velocity on gravity-driven granular flow,” *Phys. Lett. Sect. A Gen. At. Solid State Phys.*, vol. 375, no. 38, pp. 3375–3381, 2011.
- [21] V. Vidyapati, M. Kheiripour Langroudi, J. Sun, S. Sundaresan, G. I. Tardos, and S. Subramaniam, “Experimental and computational studies of dense granular flow: Transition from quasi-static to intermediate regime in a Couette shear device,” *Powder Technol.*, vol. 220, pp. 7–14, 2012.
- [22] Y. N. Chilamkurti and R. D. Gould, “Experimental and computational studies of gravity-driven dense granular flows,” in *Proceedings of the ASME 2015 International Mechanical Engineering Congress & Exposition*, 2015, pp. IMECE2015-50762.
- [23] Y. N. Chilamkurti and R. D. Gould, “Discrete element studies of gravity-driven dense granular flows in vertical cylindrical tubes,” in *Proceedings of the ASME 2016 Power Conference*, 2016, pp. POWER2016-59159.
- [24] F. Chevoir, M. Prochnow, and P. Moucheron, “Dense granular flows in a vertical chute,” *Powder and Grains*, pp. 399–402, 2001.
- [25] V. V. R. Natarajan and M. L. Hunt, “Heat transfer in vertical granular flows,” *Experimental Heat Transfer*, vol. 10, no. 2, pp. 89–107, 1997.
- [26] J. K. Spelt, C. E. Brennen, and R. H. Sabersky, “Heat Transfer To Flowing Granular Material,” *Int. J. Heat Mass Transf.*, vol. 3, pp. 791–796, 1981.
- [27] J. S. Patton, R. H. Sabersky, and C. E. Brennen, “Convective heat transfer to rapidly flowing, granular materials,” *Int. J. Heat Mass Transf.*, vol. 29, no. 8, pp. 1263–1269, 1986.
- [28] H. Ahn, “Computer Simulation of Rapid Granular Flow Through an Orifice,” *J. Appl. Mech.*, vol. 74, no. 1, p. 111, 2007.

- [29] M. F. Watkins, Y. N. Chilamkurti, and R. D. Gould, “Effective thermal conductivity of wall-adjacent layer in gravity-driven dense granular flows,” *Proc. ASME 2018 Power Energy Conf.*, pp. 1–11, 2018.
- [30] M. A. van der Hoef, M. van Sint Annaland, N. G. Deen, and J. A. M. Kuipers, “Numerical Simulation of Dense Gas-Solid Fluidized Beds: A Multiscale Modeling Strategy,” *Annu. Rev. Fluid Mech.*, vol. 40, no. 1, pp. 47–70, 2008.
- [31] N. G. Deen and J. A. M. Kuipers, “Direct numerical simulation of flow and heat transfer in dense fluid–particle systems,” *Chem. Eng. Sci.*, vol. 81, pp. 329–344, 2012.
- [32] S. Yagi and D. Kunii, “Studies on effective thermal conductivities in packed beds,” *AICHE J.*, vol. 3, no. 3, pp. 373–381, 1957.
- [33] G. K. Batchelor and R. W. O’Brien, “Thermal or Electrical Conduction Through a Granular Material.,” *Proc R Soc London Ser A*, vol. 355, no. 1682, pp. 313–333, 1977.
- [34] J. Li and D. J. Mason, “A computational investigation of transient heat transfer in pneumatic transport of granular particles,” *Powder Technol.*, vol. 112, no. 3, pp. 273–282, 2000.
- [35] G. J. Cheng, A. B. Yu, and P. Zulli, “Evaluation of effective thermal conductivity from the structure of a packed bed,” *Chem. Eng. Sci.*, vol. 54, no. 19, pp. 4199–4209, 1999.
- [36] M. G. Voronoi, “Nouvelles applications des paramètres continus à la théorie des formes quadratiques.,” *J. für die Reine und Angewandte Math.*, pp. 198–287, 1908.
- [37] 2014 STAR-CCM, “STAR-CCM+ Users Guide,” *Version 9.04.009*, 2014.
- [38] H. Ahn, Z. Başaranoğlu, M. Yilmaz, A. Buğutekin, and M. Z. Gül, “Experimental investigation of granular flow through an orifice,” *Powder Technol.*, vol. 186, no. 1, pp. 65–71, 2008.

- [39] K. L. Johnson, *Contact Mechanics*. 1987.
- [40] P. C. Vinh and R. W. Ogden, “On formulas for the Rayleigh wave speed,” vol. 39, pp. 191–197, 2010.
- [41] S. Timoshenko and J. N. Goodier, *Theory of Elasticity*. 1951.
- [42] R. Artoni, A. Santomaso, and P. Canu, “Shear bands in granular flow through a mixing length model,” vol. 34004, 2007.
- [43] B. Legawiec and D. Ziolkowski, “Structure, voidage and effective thermal conductivity of solids within near-wall region of beds packed with spherical pellets in tubes,” *Chem. Eng. Sci.*, vol. 49, no. 15, pp. 2513–2520, 1994.
- [44] W. Van Antwerpen, P. G. Rousseau, and C. G. Du Toit, “Multi-sphere Unit Cell model to calculate the effective thermal conductivity in packed pebble beds of mono-sized spheres,” *Nucl. Eng. Des.*, vol. 247, pp. 183–201, 2012.
- [45] A. O. O. Denloye and J. S. M. Botterill, “Heat transfer in flowing packed beds,” *Chem. Eng. Sci.*, vol. 32, no. 5, pp. 461–465, 1977.
- [46] M. F. Watkins, “A Heat Transfer Analysis of Vertical Dense Granular Flows,” 2018.
- [47] Y. N. Chilamkurti and R. D. Gould, “Characterizing particle-wall contact behavior and fluctuations in gravity-driven dense granular flows in cylindrical tubes using DEM,” in *ASME 2017 Power Conference Joint with ICOPE-17*, 2017, pp. 1–10.
- [48] W. Schotte, “Thermal conductivity of packed beds,” *AIChE J.*, vol. 6, no. 1, pp. 63–67, 1960.
- [49] J. Yamada, Y. Kurosaki, I. Satoh, and K. Shimada, “Radiative heat exchange between a fluidized bed and heated surface,” *Exp. Therm. Fluid Sci.*, vol. 11, no. 2, pp. 135–142, 1995.

- [50] C. Goniva *et al.*, “An open source CFD-DEM perspective,” *Proc. OpenFOAM Work.*, no. May 2016, pp. 1–10, 2010.
- [51] C. Kloss, C. Goniva, A. Hager, S. Amberger, and S. Pirker, “Models, algorithms and validation for opensource DEM and CFD-DEM,” *Prog. Comput. Fluid Dyn. An Int. J.*, vol. 12, no. 2/3, p. 140, 2012.
- [52] Z. Zhou, A. Yu, and P. ZULLI, “Particle Scale Study of Heat Transfer in Packed and Bubbling Fluidized Beds,” *IFAC Proc. Vol.*, vol. 7, no. PART 1, pp. 405–410, 2009.
- [53] L. Chen, C. Wang, M. Moscardini, M. Kamlah, and S. Liu, “A DEM-based heat transfer model for the evaluation of effective thermal conductivity of packed beds filled with stagnant fluid: Thermal contact theory and numerical simulation,” *Int. J. Heat Mass Transf.*, vol. 132, pp. 331–346, 2019.
- [54] H. Wu, N. Gui, X. Yang, J. Tu, and S. Jiang, “Numerical simulation of heat transfer in packed pebble beds: CFD-DEM coupled with particle thermal radiation,” *Int. J. Heat Mass Transf.*, vol. 110, pp. 393–405, 2017.
- [55] A. Singhal, *Arpit Singhal Heat and mass transfer in gas-solid packed beds*, no. August. 2018.